ISSN 0912-1803

PHOTON FACTORY ACTIVITY REPORT 1990

#8

NATIONAL LABORATORY FOR HIGH ENERGY PHYSICS, KEK

Photon Factory

Activity Report

1990

Staff members and users of the Photon Factory with Mt. Tsukuba in their background

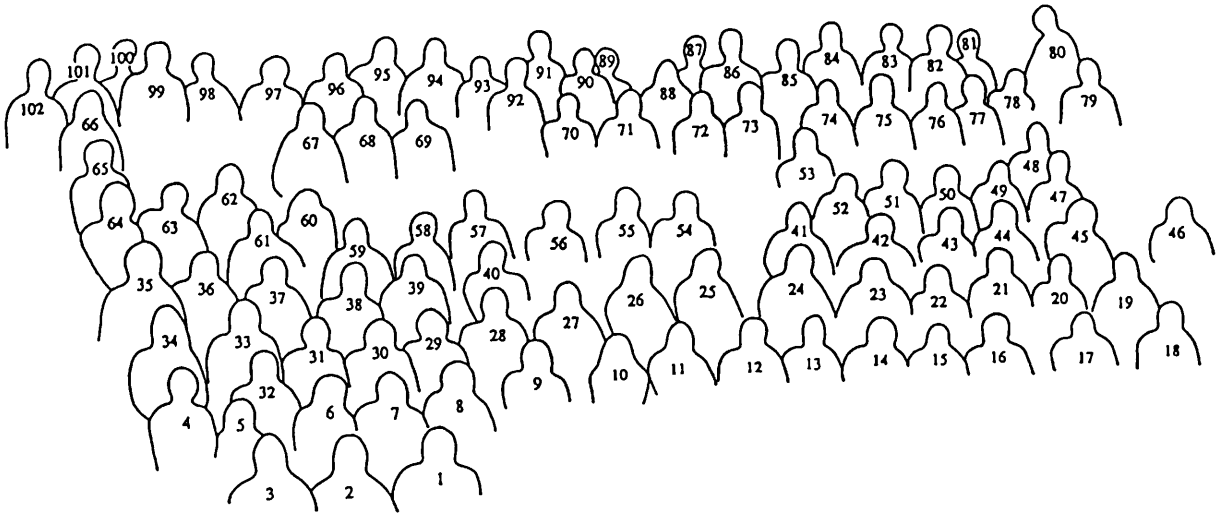

1. Y. Amemiya
2. H. Honma
3. N. Kamikubota
4. H. Sato
5. H. Katagiri
6. M. Ando
7. Y. Ogawa
8. Y. Saito
9. H. Kobayakawa
10. M. Kimura
11. A. Asami
12. H. Iwasaki
13. J. Chikawa
14. T. Urano
15. H. Kobayashi
16. T. Iwazumi
17. K. Kakihara
18. X. W. Zhang
19. T. Oogoe
20. K. Kawasaki
21. T. Koide
22. K. Nakamura
23. H. Kitamura
24. A. Enomoto
25. H. Kato
26. A. Yagishita
27. T. Yamakawa
28. Y. L. Wang
29. H. Nakamura
30. I. Abe
31. M. Kobayashi
32. N. Sakabe
33. T. Matsushita
34. S. Takano
35. A. Toyoshima
36. S. Anami
37. T. Katsura
38. S. Ohsawa
39. M. Yokota
40. N. Nakamura
41. S. Muto
42. M. Hara
43. Y. Kagoshima
44. S. Yamamoto
45. T. Nogami
46. Y. Kamiya
47. K. Furukawa
48. Y. Hori
49. S. Tokumoto
50. T. Mori
51. A. Ueda
52. S. Sakanaka
53. H. Hanaki
54. K. Mori
55. A. Nakagawa
56. S. Sasaki
57. M. Nakayama
58. N. Usami
59. K. Ito
60. T. Kosuge
61. S. Hayakawa
62. N. Watanabe
63. A. Yokoya
64. Y. Yamaguchi
65. H. Kaizu
66. A. Kikuchi
67. K. Kobayashi
68. T. Shioya
69. M. Nomura
70. A. Mikuni
71. K. Hyodo
72. S. Asaoka
73. C. O. Pak
74. S.Yamaguchi
75. Y. Takiyama
76. Y. Fukushima
77. Y. Kobayashi
78. H. Iijima
79. M. Isawa
80. K. Ohsumi
81. A. Mishina
82. T. Kamitani
83. Y. Sato
84. Y. Shimizukawa
85. T. Shidara
86. E. Shigemasa
87. Y. Takata
88. Y. Hakuta
89. A. Iida
90. A. Koyama
91. Y. Kitajima
92. N. Kanaya
93. H. Sugiyama
94. A. P. Kulikov
95. K. R. Bauchspieß
96. K. Haga
97. K. Ohmi
98. T. Kurihara
99. K. P. Huber
100. T. Kikuchi
101. G. Stark
102. Y. Ohtake

PREFACE

Jun-ichi Chikawa
Director of Photon Factory

The Photon Factory is ever growing at a considerable rate in various aspects; as of today 600 experiments are running in 1991, and the number of users is now 2300 including about 500 users from the industrial sectors. The increasing use of synchrotron radiation is ever more extensive, from fundamental researches to industrial developments. It is no exaggeration to say that the activities in the Photon Factory as a whole reflect a total picture of science and technology in Japan.

Needless to say, developments at the Photon Factory have been supported by the capability of the accelerators. At present, the 2.5 GeV PF Ring is operated with positrons at an initial beam current of 350 mA. The average current is 280 mA with one injection per day. The total operation time was 3500 hours in the fiscal year 1990 . The recent progress may be summarized as follows: (1) The rate of positron generation of the injector has been doubled (2) Six insertion devices are now in operation of the PF Ring. The vertical fluctuation of the photon beam axes was suppressed to less than 100 μm by various improvements for the beam stability. The free tuning of the undulators is under way; the gap of the magnets can be adjusted during operation of the Ring. (3) The single-bunch operation was made at the end of December. The maximum beam current is 70 mA at present.

This one bunch operation is a highlight of the year 1990: For time-resolved experiments, an avalanche-mode photodiode with the resolving time of 300 ps was developed as an x-ray high-speed detector. Combination of this detector and the multi-pole wiggler at BL-16 enables us to observe "quantum beat" in experiment of nuclear Bragg scattering with a Hematite $^{57}Fe_2O_3$ crystal. Time-resolved measurements of photo-electron and photo-ion spectroscopy were also successfully made. These experiments well demonstrated usefulness of the one-bunch operation.

Last few years have seen an increase in number of users from overseas, especially the number for protein structure analysis has exceeded that of domestic users. International collaboration has been proposed from Australia, Korea and the USSR. Recently Australian government decided to support its scientists by building a branch beamline (BL-20) at the Photon Factory, thus promoting synchrotron radiation research with a grant of 3.3 million Australian dollars in the course of three years. This joint project will prove to be fruitful and beneficial to both the countries.

Our future plan for 1990s is to convert TRISTAN Main Ring to an ultra-high-brilliance and high-coherence source. A task force, consisting of several staff members each from Accelerator Department and Photon Factory, has been organized to this effect. A recent installation of an in-vacuum-type 180-pole undulator at TRISTAN Accumulation Ring realized an x-ray source 20 times brighter than the multi-pole wiggler at BL-16 of the PF Ring. This success opened up a promising prospect for the Project to construct a 4000-pole undulator inserted in the TRISTAN Main Ring.

At the annual users' meeting "PF Symposium" our future plan was on the agenda. Prof. H. Winick, Deputy Director of SSRL, was invited as a symposium guest and gave a talk titled "Ultra-High Brightness and Coherent Radiation from Large Storage Rings". He emphasized the importance of the TRISTAN Main Ring having a circumference of 3000 m as the fourth-generation SR source and an expectation of a short wavelength free electron laser in a soft x-ray region using Self Amplified Spontaneous Emission (SASE).

In this Project, a building of a few beamlines is planned for the ultra-long undulators and FEL in the soft x-ray region installed in the 200m-long straight sections of the MR. We believe that such ultra-high brilliance sources, starting even with a few beamlines, will form a nucleus for potentially extensive needs and that its materialization is the mission of our staff members.

Finally I would like to mention my retirement at the end of March, 1991. Taking advantage of this opportunity, I would like to express my sincere and deep thanks to all those who have encouraged our research activities through the continuous and warm support to the Photon Factory during the past six years of my tenure. Their dedicated efforts have always been indispensable. Prof. Hiroshi Iwasaki, who has been the Director of Instrumentation Department, was elected to succeed me from the beginning of the fiscal year 1991. It is my most sincere wish that the Photon Factory will continue its development into 21st century under the new Director.

Acknowledgement

The editors would like to thank Miyako Kimura, Yoshiko Yamaguchi for their help in editing this issue. One of the editors (Y. A.) is grateful to Dr. Karl Rudolf Bauchspieß, visiting scientist at PF, for his careful reading of the manuscript of Instrumentation Division.

KEK Progress Report 90- 3 A/M

KEK Reports are available from:

Technical Information & Library
National Laboratory for High Energy Physics
1-1 Oho, Tsukuba-shi
Ibaraki-ken, 305
JAPAN

Phone: 0298-64-1171
Telex: 3652-534 (Domestic)
(0)3652-534 (International)
Fax: 0298-64-4604
Cable: KEKOHO

CONTENTS

OUTLINE OF THE PHOTON FACTORY

A. INTRODUCTION

The Photon Factory (PF) is a national synchrotron radiation (SR) research facility affiliated with the National Laboratory for High Energy Physics (KEK), supervised by the Ministry of Education, Science and Culture. It consists of a 2.5-GeV electron/positron linear accelerator, a 2.5-GeV electron/positron storage ring as a dedicated light source, and beamlines and experimental stations for exploiting synchrotron radiation, in studies involving such research fields as physics, chemistry, biology, medical sciences, pharmacology, earth sciences and lithography. All of the facilities for synchrotron radiation research are open to scientists of universities and research institutes belonging to the government, public organizations, private enterprises and those of foreign countries. The members of institutions affiliated with the Ministry of Education, Science and Culture are given the highest priority among all users. Applications from other organizations are also admitted with or without charge, depending upon the categories of their objectives. The Photon Factory is located at the northern end of Tsukuba Science City, about 60 km north-east of Tokyo.

B. OVERVIEW OF THE FACILITY

The general view of the facility is shown in Fig. 1. The 2.5-GeV linac housed in a 450 m long enclosure is used as an injector for both the PF storage ring and the accumulation ring (AR) of TRISTAN. The PF storage ring was already equipped with the flexibility of storing positrons in place of electrons. Part of AR has been used as a high energy synchrotron radiation source from its bending magnet and partly augmented with an insertion device to produce elliptically polarized radiation. It has been operated for synchrotron radiation users with an energy range from 5 to 6.5 GeV.

C. ORGANIZATION AND STAFF

The organization of KEK is shown in Fig. 2. The PF is composed of three divisions; Injector Linac, Light Source and Instrumentation. The organization of the PF including its personnel is shown in Fig. 3. The Advisory Council for the PF was established to discuss scientific programs and management of the PF. The council consists of twenty-one experienced scientists including ten non-KEK members (Table 1). The term of membership is two years. The Program Advisory Committee (PAC) consisting of the members listed in Table 2 accepts proposals of users and decides priorities for the experiments.

In Table 3, the names of the staff members are listed in alphabetical order to help make direct and quick contact. Also, the numbers of staff members and visiting scientists are summarized in Table 4.

D. BUDGET

The budget of the PF is supplied by the Ministry of Education, Science and Culture. The annual budget after commissioning of the facilities are shown in Table 5. The numbers of beam channels in each year are shown in Table 6.

E. OPERATION TIME

The machine operation time is divided into three terms per year. Summary and timetable of the machine operation in FY 1990 are shown in Tables 7 and 8, respectively.

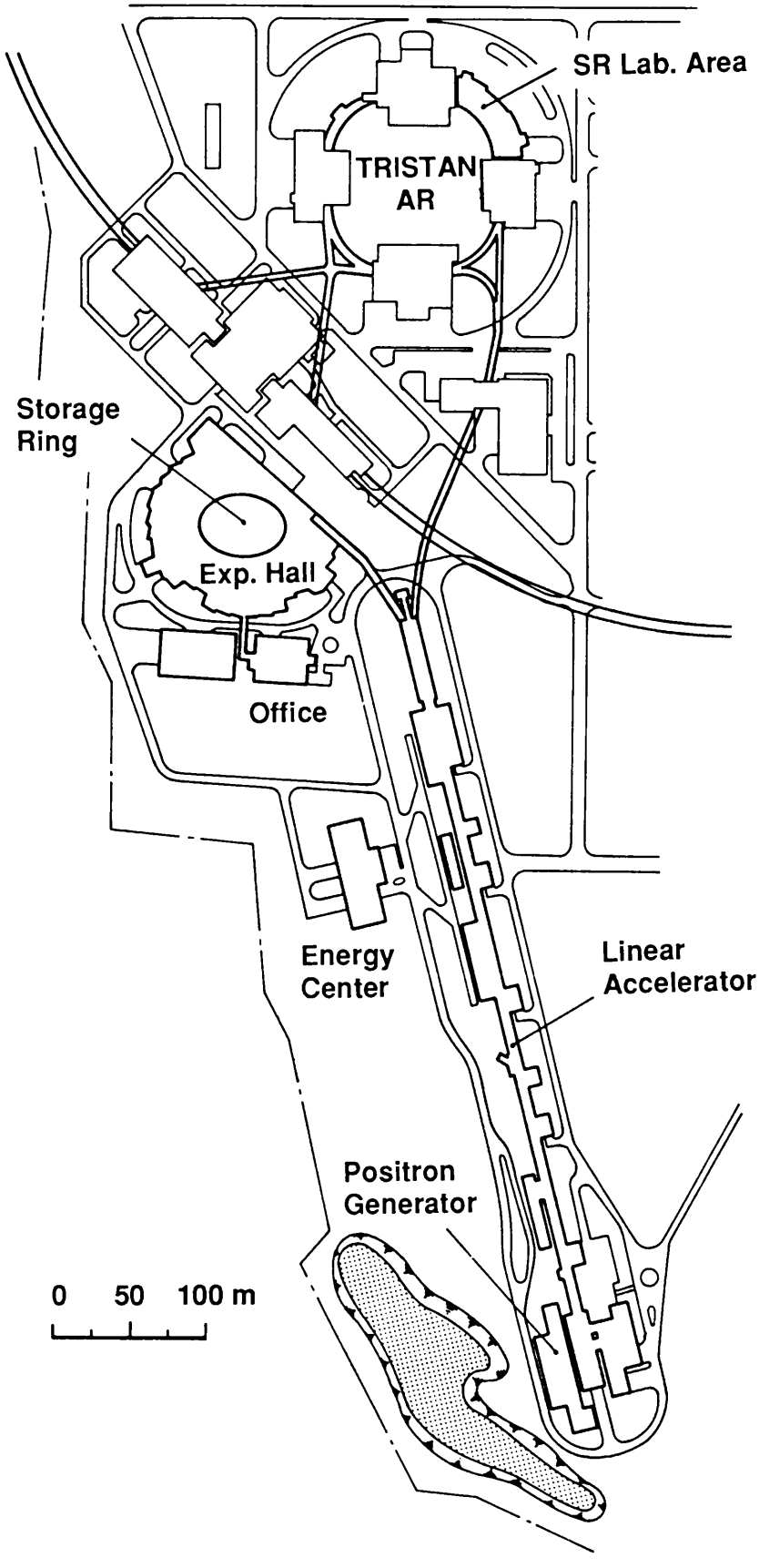

Fig. 1 Plan view of the Photon Factory

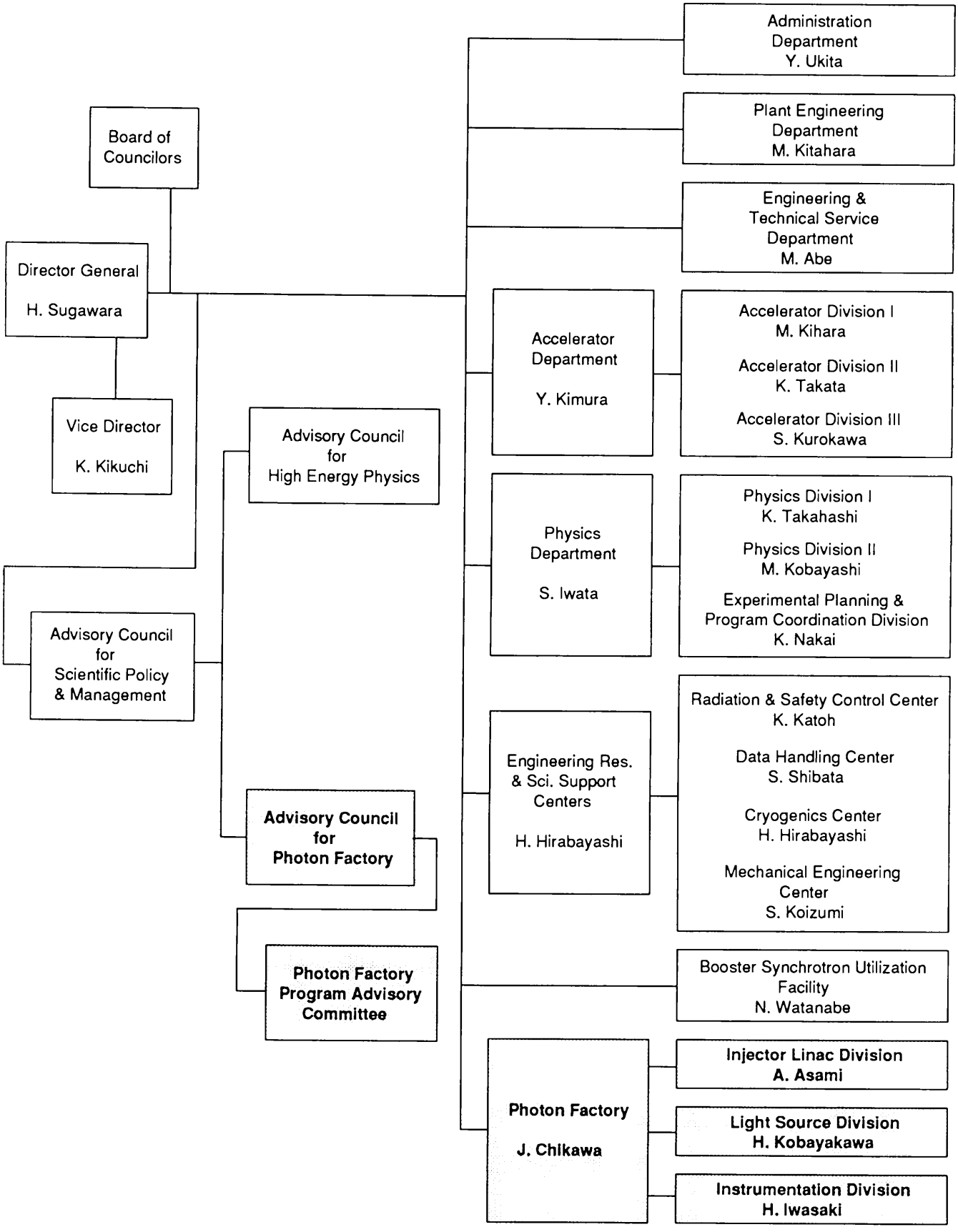

Fig. 2 Organization of KEK

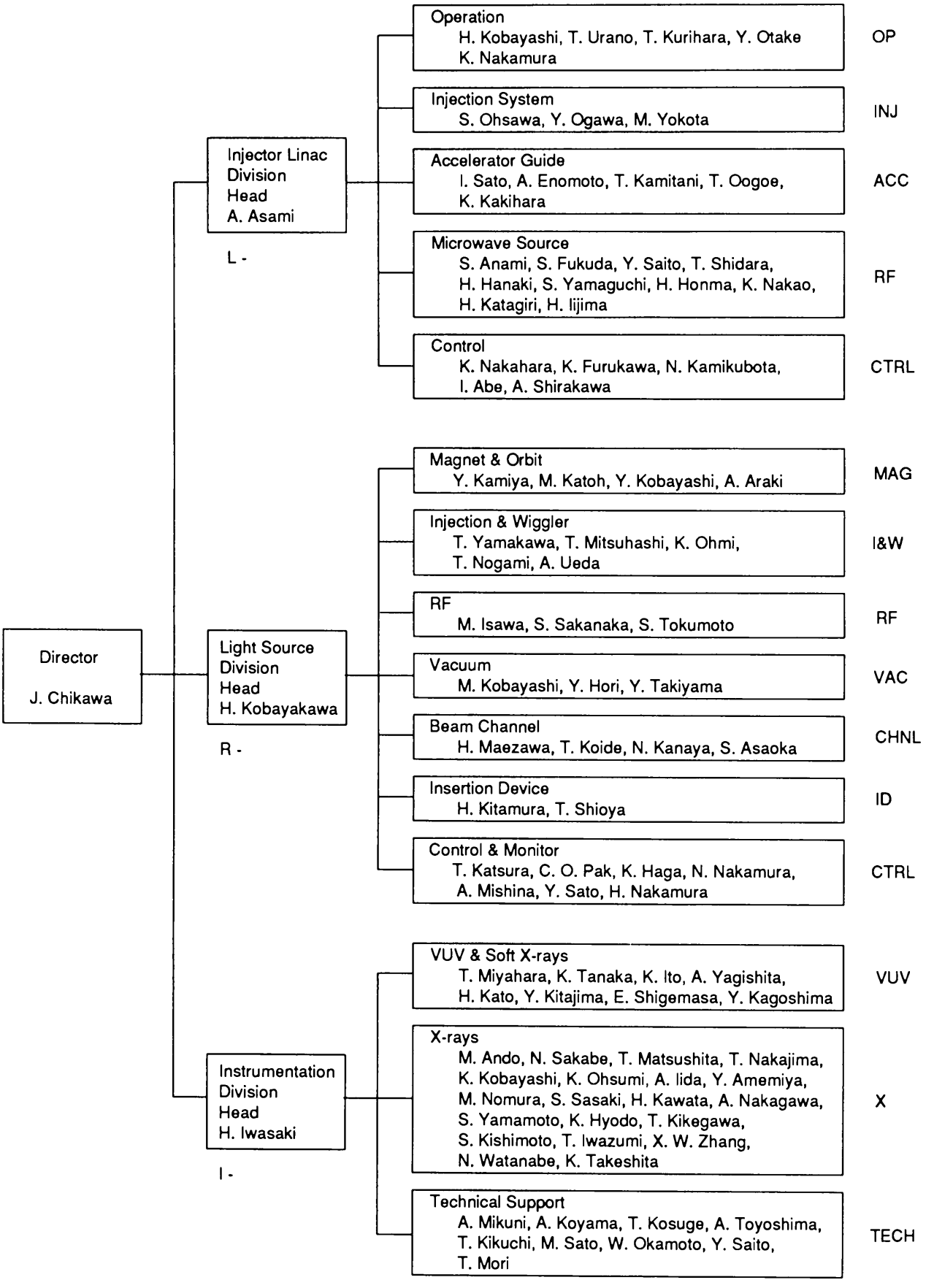

Fig. 3 Organization of the Photon Factory

Table 1 Members of Advisory Council

* Chairman ** Vice-Chairman

ANDO, Masami	Instrumentation Division, PF, KEK
ASAMI, Akira	Injector Linac Division, PF, KEK
FUJII, Yasuhiko	Institute of Materials Science, University of Tsukuba
HIEDA, Kotaro	Faculty of Science, Rikkyo University
IIJIMA, Takao	Faculty of Science, Gakushuin University
ISHII, Takehiko	Institute for Solid State Physics, University of Tokyo
IWASAKI, Hiroshi*	Instrumentation Division, PF, KEK
KATSUBE, Yukiteru	Institute for Protein Research, Osaka University
KOBAYAKAWA, Hisashi	Light Source Division, PF, KEK
KOBAYASHI, Masanori	Light Source Division, PF, KEK
KURODA, Haruo**	Faculty of Science, University of Tokyo
MAEZAWA, Hideki	Light Source Division, PF, KEK
MATSUSHITA, Tadashi	Instrumentation Division, PF, KEK
NAKAHARA, Kazuo	Injector Linac Division, PF, KEK
OHTA, Toshiaki	Faculty of Science, Hiroshima University
SAKABE, Noriyoshi	Instrumentation Division, PF, KEK
SATO, Isamu	Injector Linac Division, PF, KEK
SUZUKI, Kenji	Institute for Materials Research, Tohoku University
TOKONAMI, Masayasu	Faculty of Science, University of Tokyo
YAMAKAWA, Tatsuya	Light Source Division, PF, KEK
WAKO, Shinya	Faculty of Library and Information Science, University of Library and Information Science

Table 2 Members of Program Advisory Committee

* Chairman

ANDO, Masami*	Instrumentation Division, PF, KEK
ASAMI, Akira	Injector Linac Division, PF, KEK
GOHSHI, Youichi	Faculty of Engineering, University of Tokyo
ISHII, Takehiko	Institute for Solid Physics, University of Tokyo
IWASAKI, Hiroshi	Instrumentation Division, PF, KEK
IWASAWA, Yasuhiro	Faculty of Science, University of Tokyo
KOBAYAKAWA, Hisashi	Light Source Division, PF, KEK
KOMA, Atsushi	Faculty of Science, University of Tokyo
OHTA, Toshiaki	Faculty of Science, Hiroshima University
SAKABE, Noriyoshi	Instrumentation Division, PF, KEK
SATO, Yukinori	Research Institute for Scientific Measurements, University of Tohoku
SHIMOMURA, Osamu	National Institute for Research in Inorganic Materials
UEKI, Tatsuo	The Institute of Physical and Chemical Research
WASEDA, Yoshio	Research Institute of Mineral Dressing and Metallurgy, Tohoku University
YOSHIMORI, Akio	Faculty of Engineering Science, Osaka University

Table 3 Staff members of the Photon Factory

Name	Position	Responsibility(*)	Bitnet address
ABE, Isamu	Tech.	L-CTRL	ABEI@JPNKEKVM
AMEMIYA, Yoshiyuki	Assoc. Prof.	I-X	AMEMIYA@JPNKEKVX
ANAMI, Shozo	Assoc. Prof.	L-RF	
ANDO, Masami	Prof.	I-X	ANDO@JPNKEKVM
ARAKI, Akira	Tech.	R-MAG	
ASAMI, Akira	Prof.	L-Head	
ASAOKA, Seiji	Tech.	R-CHNL	
CHIKAWA, Jun-ichi	Prof.	Director	
ENOMOTO, Atsushi	Assoc. Prof.	L-ACC	ENOMOTOA@JPNKEKVX
FUKUDA, Shigeki	Assoc. Prof.	L-RF	
FURUKAWA, Kazuro	Res. Assoc.	L-CTRL	FURUKAWA@JPNKEKVX
HAGA, Kaiichi	Res. Assoc.	R-CTRL	HAGA@JPNKEKVM
HANAKI, Hirofumi	Res. Assoc.	L-RF	HANAKI@JPNKEKVX
HONMA, Hiroyuki	Tech.	L-RF	
HORI, Yoichiro	Res. Assoc.	R-VAC	
HYODO, Kazuyuki	Res. Assoc.	I-X	HYODO@JPNKEKVX
IIDA, Atsuo	Assoc. Prof.	I-X	
IIJIMA, Hitoshi	Tech.	L-RF	
ISAWA, Masaaki	Assoc. Prof.	R-RF	ISAWA@JPNKEKVX
ITO, Kenji	Assoc. Prof.	I-VUV	ITO@JPNKEKVM
IWASAKI, Hiroshi	Prof.	I-Head	
IWAZUMI, Toshiaki	Res. Assoc.	I-X	
KAGOSHIMA, Yasushi	Res. Assoc.	I-VUV	KAGOSIMA@JPNKEKVX
KAKIHARA, Kazuhisa	Tech.	L-ACC	KAKIHARA@JPNKEKVX
KAMIKUBOTA, Norihiko	Res. Assoc.	L-CTRL	KAMI@JPNKEKVX
KAMITANI, Takuya	Res. Assoc.	L-ACC	KAMITANI@JPNKEKVM
KAMIYA, Yukihide	Assoc. Prof.	R-MAG	KAMIYA@JPNKEKVM
KANAYA, Noriichi	Res. Assoc.	R-CHNL	KANAYA@JPNKEKVM
KATAGIRI, Hiroaki	Tech.	L-RF	
KATSURA, Tomotaro	Assoc. Prof.	R-CTRL	KATSURA@JPNKEKVM
KATO, Hiroo	Res. Assoc.	I-VUV	
KATOH, Masahiro	Res. Assoc.	R-MAG	
KAWATA, Hiroshi	Res. Assoc.	I-X	
KIKEGAWA, Takumi	Res. Assoc.	I-X	KIKEGAWA@JPNKEKVM
KIKUCHI, Takashi	Tech.	I-TECH	
KISHIMOTO, Syunji	Res. Assoc.	I-X	KISHIMOTO@JPNKEKVM
KITAJIMA, Yoshinori	Res. Assoc.	I-VUV	
KITAMURA, Hideo	Prof.	R-ID	KITAMURA@JPNKEKVM
KOBAYAKAWA, Hisashi	Prof.	R-Head	
KOBAYASHI, Hitoshi	Assoc. Prof.	L-OP	
KOBAYASHI, Katsumi	Assoc. Prof.	I-X	KOBAYASI@JPNKEKVM
KOBAYASHI, Masanori	Prof.	R-VAC	
KOBAYASHI, Yukinori	Res. Assoc.	R-MAG	
KOIDE, Tsuneharu	Res. Assoc.	R-CHNL	
KOSUGE, Takashi	Tech	I-TECH	
KOYAMA, Atsushi	Tech.	I-TECH	
KURIHARA, Toshikazu	Res. Assoc.	L-OP	
MAEZAWA, Hideki	Prof.	R-CHNL	MAEZAWAH@JPNKEKVX
MATSUSHITA, Tadashi	Prof.	I-X	MATSUS@JPNKEKVM
MIKUNI, Akira	Tech.	I-TECH	

Name	Position	Responsibility(*)	Bitnet address
MISHINA, Atsushi	Tech.	R-CTRL	MISHINA@JPNKEKVM
MITSUHASHI, Toshiyuki	Res. Assoc.	R-I&W	MITSUHAS@JPNKEKVX
MIYAHARA, Tsuneaki	Prof.	I-VUV	MIYAHARA@JPNKEKVM
MORI, Takeharu	Tech.	I-TECH	
NAKAGAWA, Atsushi	Res. Assoc.	I-X	NAKAGAWA@JPNKEKVM
NAKAHARA, Kazuo	Prof.	L-CTRL	
NAKAJIMA, Tetsuo	Assoc. Prof.	I-X	NAKATETS@JPNKEKVM
NAKAMURA, Kie	Tech.	L-OP	
NAKAMURA, Hajime	Tech.	R-CTRL	NAKAMUR@JPNKEKVM
NAKAMURA, Norio	Res. Assoc.	R-CTRL	
NAKAO, Katsumi	Tech.	L-RF	
NOGAMI, Takashi	Tech.	R-I&W	
NOMURA, Masaharu	Assoc. Prof.	I-X	
OGAWA, Yujiro	Res. Assoc.	L-INJ	OGAWAYJ@JPNKEKVX
OHMI, Kazuhito	Res. Assoc.	R-I&W	OHMI@JPNKEKVX
OHSAWA, Satoshi	Assoc. Prof.	L-INJ	OHSAWA@JPNKEKVX
OHSUMI, Kazumasa	Assoc. Prof.	I-X	
OKAMOTO, Wataru	Tech.	I-TECH	
OOGOE, Takao	Tech.	L-ACC	
OTAKE, Yuji	Tech.	L-OP	OTAKE@JPNKEKVM
PAK, Cheol On	Assoc. Prof.	R-CTRL	PAK@JPNKEKVM
SAITO, Yoshio	Assoc. Prof.	L-RF	
SAITO, Yuuki	Tech.	I-TECH	
SAKABE, Noriyoshi	Prof.	I-X	SAKABE@JPNKEKVM
SAKANAKA, Shyogo	Res. Assoc.	R-RF	SAKANAKA@JPNKEKVM
SASAKI, Satoshi	Res. Assoc.	I-X	SASAKIS@JPNKEKVM
SATO, Isamu	Prof.	L-ACC	
SATO, Masato	Tech.	I-TECH	
SATO, Yoshihiro	Tech.	R-CTRL	YOSHIHIR@JPNKEKVM
SHIDARA, Tetsuo	Assoc. Prof.	L-RF	SHIDARA@JPNKEKVM
SHIGEMASA, Eiji	Res. Assoc.	I-VUV	
SHIOYA, Tatsuro	Tech.	R-ID	SHIOYA@JPNKEKVX
SHIRAKAWA, Akihiro	Tech.	L-CTRL	
TAKESHITA, Kunikazu	Res. Assoc.	I-X	
TAKIYAMA, Youichi	Tech.	R-VAC	
TANAKA, Ken"ichiro	Assoc. Prof.	I-VUV	TANAKA@JPNKEKVM
TOKUMOTO, Shuichi	Tech.	R-RF	
TOYOSHIMA, Akio	Tech.	I-TECH	
UEDA, Akira	Tech.	R-I&W	
URANO, Takao	Res. Assoc.	L-OP	URANO@JPNKEKVX
WATANABE, Nobuhisa	Res. Assoc.	I-X	
YAGISHITA, Akira	Assoc. Prof.	I-VUV	
YAMAGUCHI, Seiya	Res. Assoc.	L-RF	
YAMAKAWA, Tatsuya	Prof.	R-I&W	
YAMAMOTO, Shigeru	Res. Assoc.	I-X	
YOKOTA, Mitsuhiro	Tech.	L-INJ	
ZHANG, Xiao Wei	Res. Assoc.	I-X	

(*) Refer to Fig. 3 for abbreviations

Table 4 Annual numbers of staff & visiting scientists

Position	Division	1978	1979	1980	1981	1982	1983	1984	1985	1986	1987	1988	1989	1990
Chief Director		1	1	1	1	1	1	1	1	1	1	1	1	1
	Injector Linac	1	2	3	3	3	3	3	3	4	4	4	3	3
Professor	Light Source	1	4	4	4	4	4	4	3	4	4	4	4	5
	Instrumentation	0	0	0	1	1	1	1	2	3	4	5	5	5
Associate	Injector Linac	0	1	1	1	2	2	2	2	1	2	3	5	7
Professor	Light Source	1	5	4	4	4	3	5	5	3	3	3	5	4
	Instrumentation	0	0	1	3	4	5	5	8	7	8	7	10	9
Research	Injector Linac	1	3	4	6	7	8	9	10	11	10	10	9	8
Associate	Light Source	0	1	4	6	7	7	6	8	9	12	12	9	11
	Instrumentation	0	0	3	2	7	10	10	10	13	13	14	11	15
Technical	Injector Linac	0	0	2	3	5	5	6	6	7	8	9	10	11
Staff	Light Source	3	3	3	4	6	6	6	6	7	7	8	10	10
	Instrumentation	0	0	0	0	1	2	4	4	8	9	11	10	9
Visiting	Injector Linac	2	2	2	2	2	2	2	2	2	2	2	2	2
Scientist	Light Source	2	6	4	4	4	4	4	4	4	4	4	4	4
	Instrumentation	0	0	6	6	6	6	6	6	6	6	6	6	6
Total		12	28	42	51	64	69	74	80	90	97	103	104	110

Table 5 PF budget in each fiscal year (in million yen)

Item	1982	1983	1984	1985	1986	1987	1988	1989	1990
Salary	402	474	484	510	561	561	642	757	764
PF Storage Ring (channel, insertion device, etc.)	0	0	0	153	131	647	0	0	196
PF Experiments	140	153	134	184	190	196	237	341	367
PF Operation & Maintenance	412	477	552	653	820	907	962	1,078	1,107
Computer Rentals	136	135	135	135	136	136	141	145	145
Positron Source & Electric Plant Operation	0	0	0	41	138	208	258	300	308
Cooling System & Electric Operation	120	111	124	180	211	214	217	231	235
Electricity	209	226	257	338	381	331	355	425	423
PF-Industrial Cooperative Experiments	0	94	84	95	185	166	302	219	171
AR Construction and Experiments						398	267	387	250
Miscellaneous	115	134	115	127	162	120	301	243	287
Total	1,534	1,804	1,885	2,397	2,864	3,884	3,682	4,126	4,253

Table 6 Yearly account of beam channels

	1981	1982	1983	1984	1985	1986	1987	1988	1989	1990
PF	6	8	8	8	10	12	13	13	15	15
Institutes	0	0	0	1	1	1	3	4	4	4
Industry	0	0	1	2	4	4	4	4	4	4
Total	6	8	9	11	15	17	20	21	23	23

Table 7 Summary of operation in FY 1990 (April 1990 - March 1991) (hours)

Cycle	Linac	PF Ring	Users' time	AR	Dedicated to SR at AR
1	2520	1944	1536	2448	2352
2	1536	1296	1080	1200	408
3	1320	1080	888	1176	689
Total	5376	4320	3504	4824	3449

Table 8 Timetable of the Machine Operation in FY 1990. L: Linac, PF: PF Ring, AR: Accumulation Ring, T: Machine Tuning, M: Machine Study, E: Users Beam Time with Vertical Wiggler, (E): Users Bonus Time with Vertical Wiggler, SR: Dedicated SR Use of AR, (SR): Parastic SR Use of AR, B: Photo-Baking of PF Ring and Beamline, BA: Beamline Alignment.

Cycle	Time	MON 9 17	TUE 9 17	WED 9 17	THU 9 17	FRI 9 17	SAT 9 17	SUN 9 17	MON 9 17	TUE 9 17	WED 9 17	THU 9 17	FRI 9 17	SAT 9 17	SUN 9 17
1-1	Date	4/2	3	4	5	6	7	8	9	10	11	12	13	14	15
	L	-		T→	←					M→	←				
	PF								T/M	(E)	←———		M———		
	AR				T→	←				(SR)					
1-1	Date	16	17	18	19	20	21	22	23	24	25	26	27	28	29
	L							M→	←						
	PF	——→	←———	E———				(E)	M→	←———	E———	→			
	AR							(SR)							
	Date	30	5/1	2	3	4	5	6	7	8	9	10	11	12	13
	L			→					←Maintenance	→	T→	←			
	PF								←———	Maintenance	———				
	AR		(SR)		→		←		Maintenance				T→	←	
1-2	Date	14	15	16	17	18	19	20	21	22	23	24	25	26	27
	L		→		M→	←				→		M→	←		
	PF	→		T/M	(E)	←———	E———		M→	(E)	←———	E———	→		
	AR							(SR)							
1-3	Date	28	29	30	31	6/1	2	3	4	5	6	7	8	9	10
	L	→		M→	←										
	PF			T/M	←———	E———			M→	←———	E———	→			
	AR							(SR)							
1-4	Date	11	12	13	14	15	16	17	18	19	20	21	22	23	24
	L	→		M→							→		←	Maintenance	
	PF	——→		T/M	←———	E———			→		←———		Maintenance	———	
	AR					(SR)				→		←	Maintenance		
1-5	DATE	25	26	27	28	29	30	7/1	2	3	4	5	6	7	8
	L		→		T→	←			→		M→	←			
	PF	——→		T/M	←———	E———		→		(E)	←———	E———	→		
	AR		→		T→	←	SR→	←		(SR)		→		M	← (SR)
1-6	Date	9	10	11	12	13	14	15	16	17	18	19	20	21	22
	L	→		M→											
	PF			T/M	←———	E———			M→	←———	E———				
	AR								(SR)						
1-6	Date	23	24	25	26	27	28	29	30	31	8/1	2	3	4	5
	L			→		M→	←			→					
	PF	———	E———	→		M→	←	E———	→						
	AR				(SR)				→						
2-1	Date	10/15	16	17	18	19	20	21	22	23	24	25	26	27	28
	L		T/M					→	←						
	PF								T/B・M→	M→	(BL)B	←———	E———		
	AR									T/B・M			→	←	

Cycle	Time	MON 9 17	TUE 9 17	WED 9 17	THU 9 17	FRI 9 17	SAT 9 17	SUN 9 17	MON 9 17	TUE 9 17	WED 9 17	THU 9 17	FRI 9 17	SAT 9 17	SUN 9 17
2-1	Date	10/29	30	31	11/1	2	3	4	5	6	7	8	9	10	11
	L	→		M→	←					→		M→	←		
	PF	→		(E)	←———	E———			→		M→		(E)	←———	E———
	AR											→		M→	←
2-1	Date	12	13	14	15	16	17	18	19	20	21	22	23	24	25
2-2	L		→		←			Maintenance		→		T→	←		
	PF	——→		←———				Maintenance	———	→			T/M	←———	E———
	AR		→		M	→		←		Maintenance			→		T→	←
2-2	Date	26	27	28	29	30	12/1	2	3	4	5	6	7	8	9
	L		→		M→	←				→		M→	←		
	PF	→		M→	(E)	←———	E———			→		(E)	←———	E———	→	
	AR				→		M	→		←			S R		→	
2-3	Date	10	11	12	13	14	15	16	17	18	19	20	21	22	23
	L	→		M→	←										
	PF				T/M	←———	E———		→		M→		←———	E———	
	AR						T／←			S R					
2-3	Date	24	25	26	27	28	29	20	31						
	L		→												
	PF	——→													
	AR		→												
3-1	Date	1/28	29	30	31	2/1	2	3	4	5	6	7	8	9	10
	L		T				→		←						
	PF								T／B——→		BA	←———	E———		
	AR					T(e⁻)			T→	←		M			
3-1	DATE	11	12	13	14	15	16	17	18	19	20	21	22	23	24
	L							→		M→	←				
	PF	——→			E———			→		M→	(E)	←———	E———		
	AR			→		←							→	←	SR
3-1	Date	25	26	27	28	3/1	2	3	4	5	6	7	8	9	10
3-2	L		→		←	Maintenance		→		T→	←				
	PF	——→		←———	Maintenance	———		→		T／M——→		←———	E———		
	AR		→		←	Maintenance		→		T→	←	SR	→M	←	SR
3-2	Date	11	12	13	14	15	16	17	18	19	20	21	22	23	24
3-3	L		→		M→	←			→		M→	←			
	PF	——→		(E)	←———	E———	→				T/M	←———	E———		
	AR		→		←			(SR)							
3-3	Date	25	26	27	28	29	30	31							
	L					→									
	PF	———				→									
	AR					→									

F. SEMINARS, MEETINGS AND PUBLICATIONS

Twenty two seminars were given by scientists who visited the PF in 1990. Nine users' meetings were held in FY 1990, including the annual PF symposium. The Photon Factory publishes its quarterly "PHOTON FACTORY NEWS" in Japanese for communication between users and staff.

PF seminars

Nordling, C. (Uppsala Univ.) Molecular physics at MAX and other SR facilities	January. 16, 1990
Smith, H.I. (MIT) Applications of X-ray Lithography in Future Microelectronics	February 8, 1990
Ikezawa, M. (Research Institute for Scientific Measurements, Tohoku Univ.) Measurements of Coherent Synchrotron Radiation	February 15, 1990
Gudat, W.S. (BESSY) Spin-resolved Photoemission, Circular Dichroism, and Other Activities at BESSY	February 21, 1990
Lee, J.S. (POSTECH) The Status of the Construction of Synchrotron Radiation Facility in Korea	February 27, 1990
Kitamura, M. (Faculty of Engineering, Tohoku Univ.) Current Status of Knowledge Engineering Technology	March 5, 1990
Tamura, T. (Carnegies Melon Univ.) An Expert System for Ladder Logic	March 5, 1990
Mantykentta, A. (Univ. of Oule) Electron Correlation in the 4d Hole State of Ba Studied by using Auger Spectroscopy	March 27, 1990
Brunet, P., Bienvenue, G. (SERA, LAL) FEL Project at LAL	April 2, 1990
Amusia, M.Y. (A.F. Ioffe Physico-Technical Inst. Acad. Sci.) Many Body Effect in the Photoionization Cross Section	April 10, 1990
Cooper, M.J. (Warwich Univ.) Recent Inelastic X-ray Scattering Experiments at the Daresbury SRS	May 21, 1990
Kohra, K. (Former Director of PF) Impression on the Recent Progress of Synchrotron Radiation Techniques in USSR	May 31, 1990
Grey, F. (Riso National Laboratory) Surface X-ray Diffraction at HASYLAB	July 12, 1990
Rosenberg, R. (Synchrotron Radiation Center, Univ. of Wisconsin) Synchrotron-Radiation Induced Photolysis of Molecules Adsorbed on Si(111)	July 13, 1990
Fuggle, J.C. (Univ. of Nijmegen) X-ray Absorption Spectroscopy of d-f-Electron System	September 21, 1990

Ono, A. (National Research Laboratory for Metrology)
A Method for Measuring Temperature Distribution of Synchrotron-Radiation Mirror surfaces with an Infrared Camera — September 20, 1990

Xian, D.C. (Beijing Synchrotron Radiation Laboratory)
Progress of BSRL — October 11, 1990

Winick, H. (SSRL)
The Third Generation SR Source around the World — October 11, 1990

McWhan, D. (NSLS)
Magnetic X-ray Scattering Studies at the NSLS — October 19, 1990

Jacobsen, C. (State Univ. of New York)
X-ray Holographic Study at the NSLS Undulator Beamline X-1A — November 2, 1990

Howry, S. (Computer System Specialist Accelerator Controls Department, SLAC)
Control Software for PEP and SSRL SPEAR — November 6, 1990

Cernik, R.J. (Daresbury Laboratory)
Instrumentation for Polycrystalline Diffraction at Daresbury Laboratory — December 10, 1990

Users' Meetings

Workshop on Design of a Vacuum Diffractometer for Surface and Interface Structure Analysis	April 4, 1990
Users' Meeting of BL-2 Undulator Beamline	May 7-8, 1990
Utilization of SR from a Bending Magnet of AR	May 16, 1990
Diffraction and Scattering from Condensed Matter under Extreme Conditions	October 12-13, 1990
Utilization of SR Pulse Produced by Single Bunch Operation	October 19, 1990
Biophysics Users' Meeting	November 14-15, 1990
Application of Circularly Polarized X-rays in the Region of 1-8 keV	December 21-22, 1990
The 8th Photon Factory Symposium (Annual Users' Meeting)	January 22-23, 1991
XAFS Users' Meeting	January 24, 1991

Publications

PHOTON FACTORY NEWS ISSN 0916-0604 Vol.8, No.1-5

G. PROPOSALS FOR EXPERIMENTS AT THE PHOTON FACTORY

The Photon Factory accepts proposals for beam time on the PF storage ring and Accumulation Ring twice a year: July 15 and January 14. The proposals are reviewed and rated on the basis of scientific and technological merit by the Program Advisory Committee (PAC) which meets in September and March. Proposals are active for a 2 year period after they are approved by the PAC. Urgent proposals are also accepted any time. The number of proposals approved by the PAC since commissioning of the PF is listed in Table 9.

The beam time at the PF is also available with fees to researchers of private corporations. No approval by the PAC is required.Scientific programs in collaboration between PF staff members and scientists of private corporations are also in progress; No fees and no approval by the PAC are required. The programs are renewed every fiscal year starting from April.

All the proposals approved during FY 1990 are listed at the end of this section.

H. GRADUATE UNIVERSITY FOR ADVANCED STUDIES

The national graduate university was established in 1988. It has the following three schools:

School of Cultural Studies
School of Mathematical and Physical Sciences
School of Life Sciences.

The National Laboratory for High Energy Physics has participated in the University to form the Department of Synchrotron Radiation Science and the department of Accelerator Science, both of which belong to the School of Mathematical and Physical Sciences.

Students in the Department of Synchrotron Radiation Science are expected to study the basic theory of emission of synchrotron radiation, its characteristics, and interaction of radiation with matter, and then engage in research by using various kinds of facilities at the Photon Factory. The research field includes the development of radiation sources, optical elements, and instruments for diffraction, scattering, spectroscopy, and irradiation experiments as well as exploration of new areas of applying radiation to science and technology. The students are expected to play an important role in the development of synchrotron radiation science in Japan.

Table 9 Number of proposals approved by the PAC.

Research Field	1983	1984	1985	1986	1987	1988	1989	1990
(A) EXAFS	42	26	35	40	61	66	57	71
(B) Biology	18	18	28	28	32	38	57	61
(C) X-Ray	24	29	75	54	73	65	61	80
(D) VUV & Soft X-Ray	19	12	27	26	28	28	36	27
Total	103	85	165	148	194	197	211	239

List of proposals accepted in fiscal 1990

Proposal Number	Spokesperson	Title
90-001	H. Kuroda Faculty of Science, Univ. of Tokyo	XAFS Studies of carbonyl clusters on SiO_2 surface modified by silane reagents
90-002	H. Kuroda Faculty of Science, Univ. of Tokyo	EXAFS studies on Pt Rh, Pr Cu bimetallic catalyst supported in NaY zeolite
90-003	Y. Iwasawa Faculty of Science, Univ. of Tokyo	EXAFS studies on structures of active Hetero-Metal sites during their syntheses and catalyses
90-004	Y. Iwasawa Faculty of Science, Univ. of Tokyo	Dynamic behavior of supported Rh dimer catalysts in metal-assisted catalysis
90-005	Y. Iwasawa Faculty of Science, Univ. of Tokyo	Static and dynamic structures of plane $[MM_{06}O_{24}]^{8-}$ ensembles attached on SiO_2 and Al_2O_3
90-006	K. Asakura Faculty of Science, Univ. of Tokyo	EXAFS studies on the supported bimetallic particle with a double layer structure
90-007	H. Nasu Faculty of Engineering, Mie Univ.	Fine structure analysis of Ti^{4+} or Te^{4+} ions in high-index glasses for nonlinear optics
90-008	H. Kawazoe Faculty of Engineering, Tokyo Institute of Technology	Coordination structure of indium in a- and c-In_2Se_3
90-009	S. Yoshida Faculty of Engineering, Kyoto Univ.	Study on the structures of non-heme iron complexes functioning enzyme-like oxygenations
90-010	S. Yoshida Faculty of Engineering, Kyoto Univ.	The variation of structural parameters of Ni-MgO solid solution with Ni concentration
90-011	H. Yamazaki Faculty of Science, Okayama Univ.	XAFS studies on local environment effect of iron atoms in ordered Fe-Pt alloys
90-012	K. Oshima Faculty of Science, Okayama Univ.	Local structure of organic superconducting BEDT-TTF salts with transition metal ion
90-013	S. Yoshikado Faculty of Engineering, Doshisha Univ.	Study on the configuration of mobile ions in one-dimensional superionic conductors by EXAFS method
90-014	Y. Osaka Faculty of Engineering, Hiroshima Univ.	EXAFS study on semiconducting microcrystallites embeded in glass
90-015	M. Sato National Science Museum	Structure analyses of macromolecular complexes by EXAFS and XANES

Proposal Number	Spokesperson	Title
90-016	H. Terauchi Faculty of Science, Kwansei Gakuin Univ.	Local strain and phase transition of KDP and CdTe
90-017	H. Kageyama Government Industrial Research Institute, Osaka	XANES and EXAFS studies on valence state and structure of ultra-fine gold particles
90-019	E. Ito Institute for Study of the Earth's Interior, Okayama Univ.	EXAFS analysis of iron-bearing silicate perovskite
90-020	I. Nakai Faculty of General Education, Tottori Univ.	The local structure of amorphous $Gd_xY_{68-x}Cu_{32}$ alloys
90-021	A. Nishijima National Chemical Laboratory for Industry	XAFS study on inter-metallic interactions of bimetallo-silicates of pentasil structure
90-022	A. Nishijima National Chemical Laboratory for Industry	EXAFS studies on changes in local structure of supported metal catalysts for vapor phase oxo reaction
90-024	A. Nishijima National Chemical Laboratory for Industry	XAFS study on the solution for impregnation of multi-component supporting catalysts
90-025	M. Misono Faculty of Engineering, Univ. of Tokyo	Structural analysis of active phase of V-P polyoxo compounds
90-026	T. Yamamura Faculty of Science, The Science Univ. of Tokyo	Zinc peptides as the models for DNA binding proteins: EXAFS, XANES, and the application of distance geometry to the results
90-027	S. Hasegawa Tokyo Gakugei Univ.	Structural analysis of moribudenum oxides magnesia catalysts by mean of EXAFS
90-028	A. Tomita Chemical Research Institute of Non-Aqueous Solutions, Tohoku Univ.	EXAFS studies on the local structures of calcium compounds on coal
90-029	N. Kosugi Faculty of Engineering, Kyoto Univ.	K-edge XANES of Cu and Ni around impurities in conductive Cu-based and Ni-based complex oxides
90-030	M. Niwa Faculty of Engineering, Nagoya Univ.	Structure of supported molybdate monolayer active for the methanol oxidation
90-031	V.A. Andreyevna X-ray Structure Analysis Laboratory	EXAFS studies of Ca^{2+}-binding protein centers upon isomorphous replacements
90-032	H. Arashi Research Institute for Scientific Measurements, Tohoku Univ.	Investigations of mixed alkali effect in β-alumina by using EXAFS measurements

Proposal Number	Spokesperson	Title
90-033	T. Miyanaga Faculty of Science, Hirosaki Univ.	EXAFS studies of the local structure of chloranilate complexes $Ln(C_6O_4Cl_2)_3$
90-034	T. Miyanaga Faculty of Science, Hirosaki Univ.	Study on the effect of anharmonicity in EXAFS
90-035	I. Nakai Department of Chemistry, Univ. of Tsukuba	Study on structural chemistry of precipitation and coloration reactions important to analytical chemistry and environmental science
90-036	S. Saigo Jichi Medical school	Rapid-freeze EXAFS studies of intermediates of heme proteins
90-037	H. Oyanagi Electrotechnical Laboratory	Development of fluorescence XAFS techniques for dilute systems
90-038	K. Shinohara Tokyo Metropolitan Institute of Medical Science	Biological application of soft X-ray holography
90-039	N. Miyoshi Department of Pathology, Fukui Medical School	Searching of sensitizer in soft X-ray region and analysis of its sensitizing reaction mechanism
90-040	M. Watanabe School of Medicine, Yokohama City Univ.	Analysis of in vitro cell transformation by SOR
90-041	M. Sasaki Radiation Biology Center, Kyoto Univ.	Studies on the mechanism of chromosome aberration formation by radiations as probed by monochromatic soft X-rays
90-042	T. Higashi Radiation Center of Osaka Prefecture	Detection of mutation in bacteria on the range of soft X-ray using an umu test
90-043	I. Nakai Department of Chemistry, Univ. of Tsukuba	Nondestructuive two dimensional chemical imaging of trace elements in biological tissues
90-044	A. Takenaka Faculty of Science, Tokyo Institute of Technology	Structural Studies of 3-isopropylmalate dehydrogenase
90-045	T. Yamane Faculty of Engineering, Nagoya Univ.	Crystal structure analysis of phospholipase A_2
90-046	T. Yamane Faculty of Engineering, Nagoya Univ.	Crystal structure analyses of Bowman-birk type inhibitors and their complex with trypsin
90-047	A. Suzuki Faculty of Engineering, Nagoya Univ.	Crystal structure analyses of bacterial α-amylases
90-049	N. Kato School of Medicine, Nagoya Univ.	Analysis of crystals of bacterial lipopolysaccharides

Proposal Number	Spokesperson	Title
90-050	H. Masuda Institute for Molecular Science	Molecular engineering studies of site-directly chemical modificated myoglobins by synchrotron radiation
90-051	A. Nakagawa Photon Factory, National Laboratory for High Energy Physics	X-ray crystal structure analysis of commelinin
90-052	H. Mizuno National Institute of Agrobiological Resources	X-ray crystal structure analysis of rice dwarf virus
90-053	D.C. Wang Institute of Biophysics Academia Sinica	X-ray data collection at high resolution for a series of human insulin mutants
90-054	X.C. Gu Department of Biology, Peking Univ.	The collection of diffraction data of autolyzed active products of porcine trypsin-mung bean trypsin inhibitor complex
90-055	A.B. Edmundson Harrington Cancer Center	The three dimensional structure of immunoglobulins
90-056	A.K. Aggarwal Columbia Univ.	Recognition and cleavage of DNA by restriction enzymes
90-057	F.A. Quiocho Howard Hughes Medical Institute	Crystallographic study of antibody Fab fragments
90-058	S.H. Kim Department of Chemistry, Univ. of California	Structural studies of RAS onlogene products and their mutant proteins
90-059	Y. Izumi Faculty of Science, Hokkaido Univ.	Solution X-ray scattering study using an imaging plate
90-060	M. Kataoka Faculty of Science, Tohoku Univ.	Solution structural studies of calmodulin with genetically modified calmodulin and squidulin
90-061	S. Nojima Faculty of Engineering, Nagoya Univ.	Crystallization process of poly (ε-caprolactone) chain in block copolymers
90-062	N. Matsushima Department of Physics School of Allied Health Processions, Sapporo Medical College	X-ray solution scattering from a high-Mr subunit of gluten
90-063	H. Kihara School of Nursing Jichi Medical School	Direct measurement of allosteric transition by stopped-flow X-ray scattering
90-064	M. Kuwabara Faculty of Veterinary Medicine Hokkaido Univ.	Free radicals in DNA exposed to X-rays with energy of phosphate K-edge
90-065	K. Hieda Faculty of Science, Rikkyo Univ.	DNA strand breaks induced by K-shell holes of carbon, nitrogen and oxygen

Proposal Number	Spokesperson	Title
90-066	N. Tanaka Faculty of Science, Tokyo Institute of Technology	Crystal structure of the multi-heme enzyme
90-067	L. Makowski Department of Physics, Boston Univ.	Multiple wavelength anomalous dispersion in fiber diffraction
90-068	D.C. Cater NASA	Structure determination of human serum albumin
90-069	F. Tokunaga Faculty of Science, Osaka Univ.	Analysis on structure change on the process of regeneration of nurple membrane
90-071	M. Akiyama Sapporo Medical College	Structure of low temperature stable phase of glycolipids
90-072	S. Kurihara The Jikei Univ. School of Medicine	Difference of cross-bridge behaviour between cardiac myosin isozymes
90-073	V.A. Anderyevna X-ray Structure Analysis Laboratory	Time-resolved study of muscle at different type of contractions (quick release and stretch; the pairwise stimulation of active muscle; investigation of tired muscle)
90-074	T. Takeda Institute of Clinical Medicine, Univ. of Tsukuba	Biochemical imaging by SR
90-075	T. Masujima Institute of Pharmaceutical Sciences School of Medicine, Hiroshima Univ.	Analysis of thermal loading of optical elements by photoacoustics
90-076	T. Masujima Institute of Pharmaceutical Sciences Scool of Medicine, Hiroshima Univ.	Fundamental development of synchrotron radiation-photoacoustics spectroscopy
90-077	M. Ishikawa National Institute of Radiological Sciences	Characterization of ultra-trace elements in marine samples by SR excited X-ray fluorescence analysis
90-078	A. Iida Photon Factory, National Laboratory for High Energy Physics	X-ray fluorescence imaging by image reconstruction technique
90-080	K. Ishida Faculty of Science and Technology, Science Univ. of Tokyo	The site determination of the impurity atoms in the high-Tc superconductor using the anomalous dispersion effect
90-081	K. Ohno National Research Institute for Metals	Determination of γ/γ' lattice misfit in nickel-base superalloys at elevated temperatures by SR parallel beam diffractometory
90-082	E. Kita Institute of Applied Physics, Univ. of Tsukuba	Structural study of transition-metal/insulater multilayerd thin films
90-083	N. Hamaya Institute of Materials Science, Univ. of Tsukuba	Mesoscopic structure and phase transition in colloidal system

Proposal Number	Spokesperson	Title
90-084	H. Suematsu Faculty of Science, Univ. of Tokyo	Phase transitions of adsorbed monolayers
90-085	H. Hashizume Research Laboratory of Engineering Materials, Tokyo Institute of Technology	X-ray interference studies of epitaxial $CaSrF_2$ crystals
90-086	J. Harada Faculty of Engineering, Nagoya Univ.	Study of thermal vibration of crystal surface by X-ray CTR scattering
90-087	H. Terauchi Faculty of Science, Kwansei Gakuin Univ.	Synchrotron radiation research of structural phase transitions of CdTe and $Pbs(PO_4)_2$
90-088	S. Wilkins CSIRO	Development and testing of optics for high resolution powder diffraction and saxs
90-089	Y. Fujii Institute of Materials Science, Univ. of Tsukuba	Structural aspects and anomalous solid state properties of metallic superlattices
90-090	M. Kurahashi National Chemical Laboratory for Industry	Structure analysis of non-linear optical materials with hetero-atoms by X-ray powder diffraction
90-091	Y. Waseda Research Institute of Mineral Dressing and Metallurgy Tohoku Univ.	Determination of the evrironmental structure around a specific atom in disordered materials by the anomalous X-ray scattering
90-092	H. Arashi Research Institute for Scientific Measurements Tohoku Univ.	Investigations of pressure-induced phase transformation in defect Fluorite using imaging plate
90-093	Y. Fujii Institute of Materials Science, Univ. of Tsukuba	Structural aspects of dense halogens under ultra high pressure
90-094	W. Utsumi Institute for Solid State Physics, Univ. of Tokyo	High pressure phase transformation of graphite at room temperature
90-095	A. Onodera Faculty of Engineering Science, Osaka Univ.	Instability of NiAs-type structure under pressure
90-096	K. Takemura National Institute for Research in Inorganic Materials	Search for core ionization in cesium under ultra-high pressure
90-097	C. Masuda Institute for Materials Research, Tohoku Univ.	Facture analysis of composite materials by X-ray CT using synchrotron radiation
90-098	K. Otsuka Institute of Materials Science, Univ. of Tsukuba	Structural change in Au-47.5 at%Cd martensite which shows a rubber-like behavior after aging

Proposal Number	Spokesperson	Title
90-099	Y. Soejima Faculty of Science, Kyushu Univ.	Superstructure analysis using x-ray anomalous dispersions. (New lambda technique)
90-100	H.P. Weber Institute of Crystallography, Univ. of Lausanne	Modelling of zeolite catalysis: an application of charge density analysis
90-101	M. Takahashi Faculty of Engineering, Tokyo Metropolitan Univ.	Crystallization of PEO in melts and blends with PMMA
90-102	Y. Osaka Faculty of Engineering, Hiroshima Univ.	Low angle X-ray diffraction study on semiconducting microcrystallite-doped glass
90-103	S. Kishimoto Photon Factory, National Laboratory for High Energy Physics	Development of high time-resolution system in X-ray region
90-104	K. Ishida Faculty of Science and Technology, The Science Univ. of Tokyo	Anomaly of fluorescence X-ray yield before the absorption edge and the target crystal surface dependence
90-105	X.W. Zhang Photon Factory, National Laboratory for High energy Physics	Variation of the X-ray total reflection critical angle as applied static electric field to a mirror
90-106	O. Sakata Research Laboratory of Engineering Materials, Tokyo Institute of Technology	Structure analysis of As/Si (111) by X-ray standing wave at grazing incidence
90-107	Y. Fujii Institute of Materials Science, Univ. of Tsukuba	Test of optical elements for X-ray inelastic scattering project
90-108	S. Nanao Institute of Industrial Science, Univ. of Tokyo	Structural study of Al-Cu-Ru icosahedral alloy by anomalous X-ray scattering
90-109	A. Onodera Faculty of Engineering Science, Osaka Univ.	Crystallization process of amorphous silica into high pressure phases
90-110	T. Kino Faculty of Science, Hiroshima Univ.	Behavior of lattice defects in nearly perfect crystals
90-111	S. Iida Faculty of Science, Toyama Univ.	Characterization of tungsten single crystal as an X-ray monochromator
90-112	S. Nanao Institute of Industrial Science, Univ. of Tokyo	Structural study of Ge/Si superlattices by X-ray anomalous scattering

Proposal Number	Spokesperson	Title
90-113	J. Yoshimura Faculty of Science, Yamanashi Univ.	Investigation into nonprojectiveness of X-ray moiré fringe patterns
90-114	Y. Syono Institute for Materials Research, Tohoku Univ.	Phase transition of rare earth oxides under high pressure
90-115	S. Endo Research Center for Extreme Materials, Osaka Univ.	Phase transition in polycrystalline graphite under ultrahigh pressure
90-116	K. Tsuji Faculty of Science and Technology, Keio Univ.	Density of liquid selenium and tellurium under pressure
90-117	K. Tsuji Faculty of Science and Technology, Keio Univ.	Structure of liquid bismuth under pressure
90-118	H. Ohno Japan Atomic Energy Research Institute	X-ray diffraction analysis of ionic liquids under high pressure
90-119	A.C. Thompson Lawrence Berkeley Laboratory	X-ray diffraction at ultrahigh pressure using multilayer focussing optics
90-120	Y. Murata Institute for Solid State Physics, Univ. of Tokyo	Heteroepitaxial growth on semiconductors using an adsorbed commensurate layer
90-122	T. Suzuki Sophia Univ.	p·A scattering of soft X-ray by solids of light element
90-123	S. Ino Faculty of Science, Univ. of Tokyo	Photoelectron angular distribution pattern using new spherical mirror analyzer
90-124	M. Taniguchi Faculty of Science, Hiroshima Univ.	Core excitons and band structures in IV-VI compound semiconductors
90-125	M. Yanagihara Research Institute for Scientific Measurements, Tohoku Univ.	Improvement of apparatus evaluate optical elements and its application
90-126	T. Hayaishi Institute of Materials Science, Univ. of Tsukuba	Shake-up processes of rare gases
90-127	K. Seki Faculty of Science, Hiroshima Univ.	Polarization XANES spectroscopy of oriented organic molecular films
90-128	H. Kuroda Faculty of Science, Univ. of Tokyo	Studies on the adsorption structure and the surface behavior of phosphine on Ni (111) and Ni (7 9 11)

Proposal Number	Spokesperson	Title
90-129	T. Ohta Faculty of Science, Hiroshima Univ.	Structural study on thiophenol adsorbed on single-crystal Ni surfaces by means of surface EXAFS and XANES techniques
90-130	T. Ohta Faculty of Science, Hiroshima Univ.	Improvement of the soft X-ray standing wave method by use of a Si (Li) solid state detector
90-131	E. Miyazaki Faculty of Science, Tokyo Institute of Technology	Angle-resolved photoemission spectroscopy of TiC single crystal surfaces and O_2, CO, H_2 adsorbed surfaces
90-132	Y. Hatano Faculty of Science, Tokyo Institute of Technology	Photodissociation of superexcited molecules as studied by using the single-bunched pulse structure of Photon Factory
90-133	Y. Hatano Faculty of Science, Tokyo Institute of Technology	Selective dissociation of superexcited states of simple polyatomic molecules by means of fluorescence spectra measuremtns
90-134	K. Ueda Research Institute for Scientific Measurements, Tohoku Univ.	Measurements of high-resolution absorption spectra of Yb and Eu
90-135	K. Tanaka Photon Factory, National Laboratory for High Energy Physics	Photochemical Reactions of adsorbed molecules at low temperature
90-136	K. Nakagawa Education Dept., Kobe Univ.	Density effects of foreign rare gases on molecular Rydberg transitions of aromatic molecules
90-137	M. Abe Faculty of science, Tokyo Institute of Technology	The study of configuration of antimony atom on adsorption site in titanium antimonate ion exchanger
90-138	P.Z. Deng Shanghai Institute of Optics & Fine Mech	Studies on dynamic process of defects in some laser and non-linear optical crystals by live X-ray topography
90-139	D.J. Weider Department Ess. State Univ. NY	Equation of state and stability of hydrous magnesium Silicate
90-140	E. Hinze Inst. Für Geowissenschaften und Lithosphärenforschung, Univ. of Giessen	Investigation of the Cu-Fe-Ni-S system as a model system for chalcogenide inclusions in diamonds
90-141	H. Takeda Faculty of Science, Univ. of Tokyo	Determination of abundances of trace siderophile and lithophile elements in meteorites and their formation condition
90-142	Y. Iwasawa Faculty of Science, Univ. of Tokyo	In situ direct structure determination of the metal oxide ultra thin layers an inorganic oxide crystals by polarized total reflection florescence EXAFS spectroscopy

Proposal Number	Spokesperson	Title
90-143	M. Kawai Research Laboratory of Engineering Materials, Tokyo Institute of Technology	The ultra-thin film formation of superconductor oxides by surface reaction epitaxy
90-144	S. Yoshida Faculty of Engineering, Kyoto Univ.	The variation of structural parameters of Co-MgO solid solution with Co concentration.
90-145	M. Hirobe Faculty of Pharmaceutical Science, Univ. of Tokyo	XAFS study on active intermediates of cytochrome P-450 models possessing thiolate axial ligand
90-146	H. Komiyama Faculty of Engineering, Univ. of Tokyo	A study of compound semiconductor multilayer fine particles by EXAFS
90-147	Y. Yoshida Faculy of Engineering, Univ. of Tokyo	Structure and electronic state of mono-atomically deposited vanadium oxide species on inorganic carried by means of XAFS
90-149	T. Murata Department of Physics, Kyoto Univ. of Education	EXAFS studies of gold silver sulfide structure on the surfaces of silver halide microcrystals
90-150	Y. Okamoto Faculty of Engineering Science, Osaka Univ.	EXAFS analysis of highly active cobalt sulfide catalysts prepared from cobalt carbonyl
90-151	G. Adachi Faculty of Engineering, Osaka Univ.	EXFAS studies on local structure of hydrogenated amorphous rare earth alloy films
90-153	I. Shimizu The Graduate School Nagatsuda, Tokyo Institute of Technology	Structural study on HR-CVD a Si: H films using EXAFS
90-154	H. Hattori Faculty of Science, Hokkaido Univ.	Pt L edge XAFS spectrum of sulfate promoted Pt/Z_rO_2
90-155	H. Hattori Faculty of Science, Hokkaido Univ.	Structure and electronic state around Cs in Cs exchanged basic zeolite
90-156	M. Ichikawa Research Institute for Catalysis, Hokkaido Univ.	Ship-in-bottle synthesis of organometallics inside zeolite and dynamic EXAFS application
90-157	M. Ichikawa Research Institute for Catalysis, Hokkaido Univ.	Characterization of Pd-Cu metal particles in mordenite by EXAFS
90-158	A. Tomita Chemical Research Institute of Non-Aqueous Solutions, Tohoku Univ.	EXAFS studies on the thermal decomposition of metal complex adsorbed on carbon
90-159	K. Ozutsumi Department of Chemistry, Univ. of Tsukuba	EXAFS studied on homodinuclear mercury(II) porphyrin in solution

Proposal Number	Spokesperson	Title
90-160	Y. Iwasawa Faculty of Science, Univ. of Tokyo	EXAFS and XANES studies of the behavior of catalytic reaction intermediates using attached metal clusters
90-161	M. Yamada Faculty of Engineering, Nagoya Institute of Technology	EXAFS study of Cu-Ti- and Ni-Ti-base ternary alloy glasses
90-162	T. Mukoyama The Institute for Chemical Research, Kyoto Univ.	X-ray absorption experiment of the fine structure in higher energy region than EXAFS state
90-163	Y. Ito The Institute for Chemical Research, Kyoto Univ.	High temperature local structure analysis of β-PbF_2 with fluorite type structure
90-165	S. Yano Faculty of Science, Nara Women's Univ.	Functional designs, organization, and their multidimensional applications of metal containing complex compounds
90-166	T. Yokoyama Faculty of Science, Hiroshima Univ.	Temperature dependence of EXAFS spectra of alkali halide solid solutions: comparison with that of silver halide solid solutions
90-167	A. Yoshiasa Faculty of Science, Hiroshima Univ.	EXAFS study on the phase transition of superionic conductor AgI
90-168	K. Koto Department of Materials Science Faculty of Integrated Arts and Sciences Tokushima Univ.	EXAFS study on anharmonic thermal vibrations in the 4- and 6-coordinated binary crystals
90-169	M. Nagumo School of Science and Engineering, Waseda Univ.	EXAFS study on amorphization and crystallization process of solid state reaction alloys
90-170	K. Segawa Faculty of Science and Engineering, Sophia Univ.	EXAFS study of MoO_3 catalysts on composit supports by CVD method
90-171	A. Hanaki National Institute of Rediological Sciences	Characters of the Cu(II)-S(Thiol) bond in low-molecular weight complexes
90-172	I. Kojima National Chemical Laboratory for Industry	Structure analysis of metal complexes with formazane compounds containing various functional groups by XAFS
90-173	K. Sakurai National Research Institute for Metals	EXAFS study on the Cu base alloy systems synthesized by mechanical alloying
90-174	Y. Ujihira Faculty of Engineering, Univ. of Tokyo	EXAFS study of amorphous iron alloy prepared by electrodeposition
90-175	M. Itoh Institute of Atomic Energy, Kyoto Univ.	Analysis of micro structure of metal ultrafine particles from EXAFS measurements

Proposal Number	Spokesperson	Title
90-176	S. Tanaka Senshū Univ.	Studies on phase transition in $LaNi_5$ by means of EXAFS
90-177	K. Yamazaki Faculty of Science, Okayama Univ.	Local structure on rare-earth iron garnet by means of magnetic EXAFS and EXAFS measurements
90-178	K. Takakura Department of Physics College of Liberal Arts, International Christian Univ.	DNA damage in aqueous solution induced by soft X-rays arising from synchrotron radiation
90-179	K. Suzuki School of Medicine, Tokai Univ.	An action spectrum and DNA damage of bacteriophage T1 by ultra-soft X-rays
90-180	K. Machida Faculty of Pharmaceutical Sciences, Kyoto Univ.	X-ray crystal structure analysis of human lysozyme and its complexes with saccharides
90-181	J. Hajdu Lab. Mol. Biophys, Oxford Univ.	High resolution data collection on orthorhombic crystals of spinach Rubisco.
90-182	N. Watanabe Photon Factory, National Laboratory for High Energy Physics	X-ray crystal structure analysis of ω-amino acid: pyruvate aminotransferase
90-183	K. Miki Faculty of Engineering, Osaka Univ.	Crystallographic study of flavoprotein, FP390
90-184	Y. Sugawara The Institute of Physical and Chemical Research	Crystal structure analysis of aleuria aurantia lectin
90-185	J. Read Dept of Med. & Infect. Diseases, Univ. of Alberta	X-ray data collection on pertussis toxin
90-186	W.A. Bridger Dept. of Biochemistry, Univ. of Alberta	Succinyl-CoA synthetase
90-187	M.N.G. James Dept. of Biochemistry, Univ. of Alberta	X-ray diffraction data collection for β-hexosaminidase
90-188	D. Stuart Lab. of Molecular Biophysics, Univ. of Oxford	Structural studies on HIV reverse transcrietaes
90-189	L.Z. Jun Institute of Biophysics, Academia Sinica	Structure analysis of P. versicolor D-glyceraldehyde-3-phosphate dehydrogenase at high resolution
90-190	K. Hyodo Photon Factory, National Laboratory for High Energy Physics	Development of monochromator system for the K-edge subtraction coronary angiography

Proposal Number	Spokesperson	Title
90-191	T. Takeda Institute of Clinical Medicin, Univ. of Tsukuba	An animal experiment with iodine filter angiography
90-192	Y. Hiragi The Institute for Chemical Research, Kyoto Univ.	Structural kinetics of association of CGMMV protein by T-jump small-angle scattering
90-193	S. Nomura Kyoto Institute of Technology	Dynamic observation of model network formation by small angle X-ray scattering
90-194	H. Urakawa Faculty of Engineering and Design, Kyoto Institute of Technology	Reconstitution process of TMV by stopped-flow small-angle scattering
90-195	Y. Sano National Food Research Institute	Characterization of oligosaccharide in solution by small-angle X-ray scattering
90-196	K. Nakagawa Faculty of Education, Kobe Univ.	Study on basic processes of radiation damage in organic solids
90-197	Y. Satow Faculty of Pharmaceutical Science, Univ. of Tokyo	Methodological studies for structure determination of micro protein crystals of immunogloblin F_v fragment
90-198	K. Nagai MRC Laboratory of Molecular Biology	X-ray crystallographic study of spliceosomal proteins and their complexes with RNK
90-199	K. Wakabayashi Faculty of Engineering Science, Osaka Univ.	X-ray small-angle scattering studies on structural change of a myosin head (SI)
90-200	Y. Tajima Faculty of Science, Tokyo Metropolitan Univ.	X-ray diffraction studies of the thin filament in a tonically contracting muscle
90-201	H. Suzuki Faculty of Engineering, Tokyo Engineerng Univ.	Observations of dynamical behaviors of dislocations in solid helium by X-ray topography
90-202	M. Wakatsuki Institute of Materials Science, Univ. of Tsukuba	Analysis of impurity distribution in diamond by the X-ray florescence method
90-203	Y. Ohashi Faculty of Science, Tokyo Institute of Technology	Dynamical structure analysis of desolation process in cobaloxime complex crystal
90-204	T. Ishiguro Faculty of Science, Kyoto Univ.	Superstructure of heterogenious LB multilayer
90-205	Y. Fujii Institute of Materials Science, Univ. of Tsukuba	Pressure-induced phase transition in triangular antiferroelectric $K_2Ba(NO_2)_4$
90-206	K. Ohsima Institute of Physics, Univ. of Tsukuba	Study on the precursive phenomena of phase transition from metallic sodium

Proposal Number	Spokesperson	Title
90-207	Y. Maeda Japan Atomic Energy Research Institute	SOR diffuse scattering study of vacancy clusters in quenched copper
90-208	I. Shirotani Faculty of Engineering, Muroran Institute of Technology	Phase transitions of phosphorus-arsenic alloys under low temperatures and high pressure
90-210	Y. Nogami Faculty of Science, Kyoto Univ.	Structural changes in κ-type ET salts at low temperature
90-211	K. Tsuji Faculty of Science and Technology, Keio Univ.	Pressure-induced phase transition from crystal to amorphous state in Si and Ge
90-212	K. Hisatake Kanagawa Dental College	SOR irradiation induced change of complex permeability in yttrium iron garnet
90-213	S. Sasaki Photon Factory, National Laboratory for High Energy Physics	Electron density distribution of superconductor $Tl_2CaBa_2Cu_2O_8$ below and above the Tc
90-214	M. Kimata Dept. of Earth Science, Univ. of Tsukuba	Crystal Structure of anorthite solid solution as a single micro crystal
90-215	T. Yamanaka College of General Education, Osaka Univ.	Precise measurements of forbidden reflection about diamond type crystals
90-217	Q. Tran-Cong Kyoto Institute of Technology	Analysis of the ordered structures resulting from polymer blends irradiated with light: mixtures of polystyrene, corresponding derivatives and poly (vinyl methylether)
90-218	O. Nittono Faculty of Engineering, Tokyo Institute of Technology	Characterization of crystallinity and interface structure of thin films deposited on substrates by X-ray diffraction goniometry
90-219	T. Takahashi The Institute for Solid State Physics, Univ. of Tokyo	Characterization of epitaxially grown thin crystals by X-ray diffraction
90-220	H. Hirayama Radiation & Safety Control Center National Laboratory for High Energy Physics	Experiments on the energy deposition of X-rays to matter
90-221	H. Sugiyama Photon Factory, National Laboratory for High Energy Physics	Lattice distortion and pore morphology of porous silicon studies by means of X-ray diffraction techniques
90-222	Y. Masumoto Institute of Applied Physics, Univ. of Tsukuba	Structural analysis of ZnSe-ZnS superlattice
90-223	S. Koumura Faculty of Integrated Arts and Science, Hiroshima Univ.	Mesoscopic structure ordering of microemulsions

Proposal Number	Spokesperson	Title
90-224	E. Ohtani Faculty of Science, Tohoku Univ.	Department of the pressure scalemate high temperatures by the double stage multianvil system
90-225	N. Hamaya Institute of Materials Science, Univ. of Tsukuba	Pressure-induced second-order phase transition in praseodymium
90-226	A. Ogata Accelerator National Laboratory for High Energy Physics	Plasma wakefield acceleration experiments
90-228	N. Shiotani College of Liberal Arts and Science, Tokyo Univ. of Fisheries	Electronic structure study by high resolution and/or magnetic Compton scattering
90-229	H. Yamazaki Faculty of Science, Okayama Univ.	Magnetic absorption measurements of transition metals and rare earths by circularly polarized X-rays
90-230	N. Sakai The Institute of Physical and Chemical Research	X-ray magnetic diffraction
90-231	M.J. Cooper Physics Department, Warwick Univ.	Compton scattering studies of momentum density in alloys and compounds
90-232	H. Tagawa College of Science and Technology, Nihon Univ.	Dynamical SAXS investigations on micro-phase segregated structures of segmented polyurethanes
90-233	H. Maezawa Photon Factory, National Laboratory for High Energy Physics	XES and XPS study of 3d shell in rare earth compounds
90-234	J. Kawai The Institute of Physics and Chemical Research	Total reflection X-ray photoelectron spectroscopy
90-235	S. Nakai Faculty of Engineering, Utsunomiya Univ.	Polarization dependency in the Ce 3d XAS of $CeRh_3B_2$
90-237	T. Sasaki Photon Factory, National Laboratory for High Energy Physics	Photofragmentation dynamics of molecules composed of light elements
90-238	M. Niwano Research Institute of Electrical, Tohoku Univ.	SR-induce deposition of ultrathin dielectric films on semiconductors
90-239	Y. Aiura Electro technical Laboratory	Study of electronic structure of high-Tc superconductors $Nd_{2-x}Ce_xCuO_{4-\delta}$ system by photoemission spectroscopy
90-241	A. Fujimori Faculty of Science, Univ. of Tokyo	Low temperature photoemission spectroscopy of high-Tc superconductors

Proposal Number	Spokesperson	Title
90-242	M. Yanagihara Research Institute for Science Measurements, Tohoku Univ.	Studies on the thermal resistivity and radiation damage of soft X-ray multilayers
90-244	H. Tagawa College of Science and Technology, Nihon Univ.	Conformational change of sarcosine-alanine-sarcosine block copolymer in water
90-245	V.J. James The Univ. of New South Wales	Low angle diffraction study of collagen fibres from normal and diabetic skin
90-246	K. Hodgson Department of Chemistry, Stanford Univ.	Kinetic intermediates on the pathway of protein folding
90-247	K. Suzuki The research Institutte for Iron Steel and Other Metals, Tohoku Univ.	Local structure of amorphous Ce-Cu alloy preduced by vaper quenching
90-Y001	K. Miyauchi Center Research Laboratory Hitachi Ltd.	BL-8A; soft X-ray diffractometry, XPS. B; silicon EXAFS experiments, total reflection measurement. C; digital radiography, lithography, microprobe experiments, CT, and micro X-ray diffractometry.
90-Y002	S. Oda Fuji Photo Films Co., Ltd.	Application of high-sensitive EXAFS to characterization of AgX
90-Y003	Y. Ishii Applied Electronics Laboratory NTT	Materials analysis, lithography and photo-reaction using SR
90-Y004	H. Miyagi Center Research Laboratory Hitachi Ltd.	Development of angiographic system using iodine filter method
90-Y005	Y. Goto Fundamental Research Lab. NEC Corp.	X-ray optics, X-ray lithography and photo-chemical reactions experiments
90-Y006	T. Hisatsugu Fujitsu Laboratory Ltd.	Exposure test by synchrotron radiation in BL-17A, BL-17B, and BL-17C
90-Y007	K. Yoshida Research Center Mitsubishi Chemical Industries Ltd.	The EXAFS study of catalysts and thin films
90-Y008	K. Ohshima Mitsui Toatsu Chemicals, Inc.	EXAFS of supported metallic or metal oxide catalysts
90-Y009	Y. Obi Central Research Institute Japan-Tabacco Inc.	Crystallographic studies on Mirabilis anti-viral protein
90-Y010	M. Takeuchi The Association for Progress of New Chemistry	EXAFS of polymer sheet containing ultrafine semi-conductor particles
90-Y011	M. Takeuchi The Association for Progress of New Chemistry	Micro-analysis of contaminants on a silicon wafer by X-ray fluorescence

Proposal Number	Spokesperson	Title
90-Y012	K. Yoshida Research Center Mistubishi Chemical Industries Ltd.	The EXAFS study of catalysts and thin film
90-Y013	T. Hisatsugu Fujitsu Laboratory Ltd.	Exposure tests by synchrotron radiation in BL-17A, BL-17B, and BL-17C
90-Y014	Y. Goto Central Research Lab. NEC Corp.	X-ray optics, X-ray lithography and photo-chemical reaction experiments
90-Y015	K. Miyauchi Center Research Laboratory Hitachi Ltd.	BL-8A; soft X-ray diffractometry, XPS. B; silicon EXAFS experiments, total reflection measurement. C; digital radiography, lithography, microprobe experiments, CT, and micro X-ray diffractometry.
90-Y016	Y. Goto NEC Corp.	X-ray optics, X-ray lithography and photo-chemical reaction experiments
90-Y017	N. Ishikawa Idemitsu	An EXAFS study of platinum and ruthenium on catalysts
90-Y018	K. Ohshima Mitsui Toatsu Chemicals, Inc.	EXAFS of (supported) metallic or metal-oxide catalysts-3
90-Y019	K. Ohshima Mitsui Toatsu Chemicals,Inc.	EXAFS of fine acicular particles of α-Fe
90-Y020	J. Miyahara Fuji Photo Films Co., Ltd.	Analysis for clinical effects of dual energy subtraction mammography
90-Y021	S. Oda Fuji Photo Films Co., Ltd.	Application of EXAFS to characterization of silver halide
90-C001	K. Kinoshita Hamamatsu Potencies K.K.	Magnetic-imaging photoemission-spectromicroscope study with synchrotron radiation
90-C002	K. Yamazaki Engineering Research Center, NKK Corp.	Study on designing technologies of synchrotron radiation beamlines and optics
90-C003	S. Kawado Research Center, Sony Corp.,	Characterization of Si crystals and process-related materials
90-C004	M. Matsumoto Mechanical Research Laboratory, Hitachi Ltd.	Photodesorption and photon cleaning of practical materials
90-C005	T. Mochizuki Division of Nuclear Power Plant, NKK Corp.	Development of a beamline for high brilliance quasi-monochoromatic x-rays
90-C006	H. Hashimoto Toray Research Center	Fluorescence EXAFS spectrometer for soft X-ray region
90-C007	K. Kawashima Electronics & Control System R&D	Department of a high-resolution CT imaging system using the high energy X-rays
90-C008	T. Takigawa ULSI Research Center, Toshiba Corp.	Study of new technique in synchrotron radiation processing of Semiconductor materials

Proposal Number	Spokesperson	Title
90-C009	A. Aoki Technical Research Center, NKK Corp.	Structure analysis of materials bombarded with particle beams
90-C010	Y. Muramatsu Applied Electronics Laboratories, NTT	Monochromator technologies for highly brilliant insertion device radiation
90-C011	S. Suzuki Tsukuba Research Center, Sanyo Electric Co., Ltd.	Micro patterning by synchrotron radiation
90-C012	H. Morikawa Nippon Steel Corp.	Dynamic observation of materials processing using synchrotron radiation
90-C013	S. Yasuami Research & Development Center, Toshiba Corp.	Characterization of semiconductor materials using soft X-ray EXAFS and X-ray diffraction
90-C014	T. Kojima Takatsuki Research Laboratory, Sumitomo Chemical Co., Ltd.	Dynamic structure of synthetic polymer materials using small angle X-ray scattering
90-C015	T. Kitano Central Research Laboratories, NEC Corp.	Characterization of semiconductor materials by high precision X-ray optics
90-C016	N. Yoshioka LSI Research Research & Development Laboratory, Mitsubishi Electric Corp.	Industrial application of soft X-ray spectroscopy
90-C017	M. Funabashi Research Development Corp. of Japan	Study of photochemical processes on surfaces using synchrotron radiation
90-C018	H. Nagata Research development Corp. of Japan	Analytical studies on fabricated surfaces using synchrotron radiation
89-C009	H. Ayato Research Laboratories, Ashigara, Fuji Photo Film Co., Ltd.	Structural analysis of halogen compound by EXAFS method with SR
89-C020	T. Yagi Development Center, Konica Corp.	Structure analysis of halogen compound by powder diffraction method with synchrotron radiation
90-C021	K. Konashi Power Reactor and Nuclear Fuel Development Corp.	Basic study for development of high intensity CW electron accelerator
90-C022	Y. Fukuda Canon Inc.	Studies on the optical properties of soft X-ray dispersion elements
90-C023	S. Morita Petroleum Energy Center	Study on the catalytic desulfurization of petroleum fractions by means of EXAFS
90-C024	S. Suzuki Nuclear Power Division, Shimizu Corp.	Study on the effect of the building distortion to the beam orbit in the Photon Factory storage ring
90-C025	H. Nagata Nikon	Characterization of X-ray multilayer-mirrors using synchrotron radiation

Proposal Number	Spokesperson	Title
90-C026	K. Sano Shimazu Corp.	Development of SiC grating for soft-x-ray
90-C027	Y. Maejima Tokyo Denshi Yakin Laboratory, INC.	Growth of dislocation-free <110> Ge crystal

Y: approved for charged beam time,
C: Collaborations between the Photon Factory and institutes of private companies.

Injector Linac Division

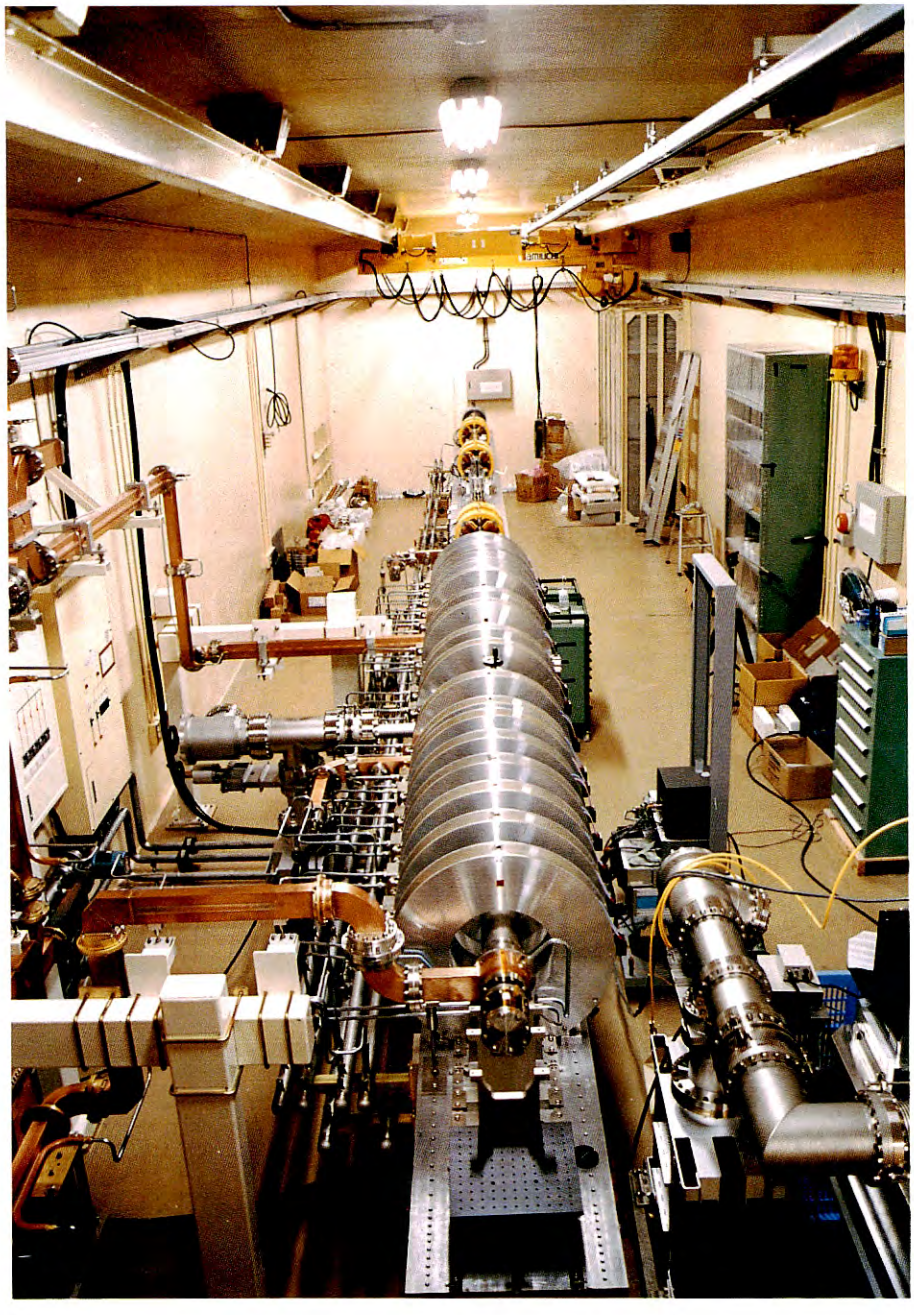

Test Linac under construction beside the PF 2.5-GeV Linac electron-gun room.

CONTENTS

INJECTOR LINAC DIVISION

A. INTRODUCTION

In recent years the annual operation time of the linac has exceeded 4,500 hours; between October 1989 and September 1990, it reached 5,100 hours. In spite of this long operation time, the operation rate has been further improved from the previous year (97 %), reaching around 99 %. This high operation rate is achieved as the result of various efforts to increase the accelerator reliability.

Continual efforts have been made to improve the linac control system by extending the main control network to two other buildings; it has become possible to monitor various operational conditions of the linac there. Improvements in the DS-Link system were also carried out by expanding its function, enabling a graphical display, the use of various computers, etc. An EXPERT system was developed to aid in trouble-shooting of an electron gun system. Most of the klystrons used now have barium-impregnated cathodes; most of the PFN capacitors are a new type which can operate at higher working voltages. The tuning procedure of the accelerator was carefully examined and determined in detail, which was also effective for improving the accelerator reliability. The rf power and phase should be varied at high power to achieve the optimum condition in the injector section of the linac. However, these two quantities are closely related to each other in devices currently being used, making accelerator tuning quite complicated. A new device has recently been developed, which enables us to vary the power and phase independently.

From February 1990, the TRISTAN group started high-luminosity experiments as the phase-II stage of e^+/e^- collision research; they needed more positrons. It was therefore decided to reinforce the focusing system of positrons. This system comprises a pulsed solenoid coil, a DC solenoid, and succeeding quadrupole magnets. New pulsed and DC solenoid coils were designed to produce magnetic fields twice as large as those of the old ones. Fourteen quadrupoles were to be added. Fabrication and installation of half of these focusing elements were achieved during the summer shutdown time; the remainder will be installed in early 1991. By this reinforcement of the focusing system we expect to double the positron intensity.

For advanced accelerator studies it is necessary to have a dedicated linac. Such a linac is also useful for testing various components of the accelerator, resulting in improvements. The construction of a small linac, Test Linac, was started for this purpose. The main parameters of this linac are that the maximum energy is to be 60 MeV at a 10 μA maximum average current. A few of the major subjects to be investigated are: (1) high-brightness beam production and acceleration, (2) the rf gun, and (3) experiments involving a free electron laser.

In recent years a considerable improvement of high-power klystrons has been achieved by adapting a barium-impregnated cathode; the breakdown of their ceramic windows, however, is still one of the major problems to be solved regarding the klystrons. An investigation of the breakdown mechanism has been continued, and it was recently shown that puncturing of the alumina disk is induced by localized surface melting, which is caused by multipactor electron bombardment.

Other research programs were recently undertaken concerning the following subjects: (1) new alignment system, (2) new accelerator structure, (3) wake-field in multibunch beam, (4) plasma wake-field accelerator, and (5) positron channeling. The new alignment system is for future advanced accelerators, and is aimed at very precise alignment using a laser and interferometers. The new accelerator structure study concerns very high-duty operation of an linac. One of the most important problems is to suppress production and to efficiently remove heat. A study of a wake-field in a multi-bunch short-pulse beam is one of the subjects to be carried out regarding future linear colliders. In a plasma wake-field accelerator experiment, the energy change of the beam was 12 MeV; a deceleration though, was observed, the largest value ever obtained experimentally. Following the previous period an experiment was continued concerning positron channeling; after much effort to produce a highly collimated beam and to reduce back-ground, a 2.5-GeV positron channeling phenomenon was confirmed in a silicon crystal.

A. Asami

B. OPERATION

During the period from October 1989 to September 1990, the linac has been successfully and stably operated with a total operation time of 5,181 hours, and a highly reliable operation rate of 99.1%.

Operation statistics for this period are listed in Table 1. During this run, the operation group was able to improve the linac start-up procedure after a scheduled shutdown. Several tens of steps according to a fixed order are used to maintain the reproducibility of the machine parameters. This precise tuning at the start of operation seems to keep the linac stable for a long time. This is one of the reasons for achieving a high operation rate.

Cumulative usage hours and averaged fault rate along with the averaged applied anode voltage during the last eight years are shown in Tables 2 and 3, respectively. Klystrons with barium-impregnated (BI) cathodes were introduced into the linac from 1987, and occupied more than 70% of total klystrons used in the linac at the end of July 1990. A very low fault rate of BI tubes has considerably reduced operation interruptions.

H. Kobayashi

Table 1. Operation and failure time of each cycle.

Term-cycle	Date	Operation time (hrs)	Failure time (hrs)	Operation rate (percent)
FY 1989				
2-1	Oct. 3 - Oct. 25	524	3.7	99.3
2-2	Oct. 31 - Nov. 28	638	3.8	99.4
2-3	Dec. 1 - Dec. 25	564	5.0	99.1
3-1	Feb. 13 - Mar. 10	592	10.6	98.2
3-2	Mar. 10 - Mar. 26	380	5.7	98.5
FY 1990				
1-0	Apr. 4 - May 3	684	3.3	99.5
1-1	May 10 - June 1	516	4.7	99.1
1-2	June 10 - June 20	448	6.3	98.6
1-3	June 25 - July 31	835	4.0	99.5
total		5,181	47.1	99.1

Table 2. Cumulative usage hours of klystrons during the past years.

Period	Total	Unused	Failed		Living		MTBF
	No. of tubes	No. of tubes	No. of tubes	Mean age (hours)	No. of tubes	Av.op.time (hours)	(hours)
up to 1985/7	79	2	28	3,600	49	6,200	13,400
up to 1986/7	91	3	39	4,400	49	7,400	13,100
up to 1987/7	106	4	52	4,400	50	9,600	13,600
up to 1988/7	120	2	67	4,500	51	11,400	13,500
up to 1989/7	140	5	82	6,400	53	12,400	14,400
up to 1990/7	158	7	97	8,600	54	11,200	14,800

Table 3. Averaged fault rate and averaged applied voltage to klystrons.

Period	Fault rate (/day·tube)	Applied voltage (kV)	Total operation (tube-days)
1982/8 - 1983/7	2.5	238	4,470
1983/8 - 1984/7	1.6	242	4,150
1984/8 - 1985/7	1.2	240	4,420
1985/8 - 1986/7	1.0	238	5,600
1986/8 - 1987/7	1.0	239	7,740
1987/8 - 1988/7	1.0	240	9,990
1988/8 - 1989/7	0.6	241	10,510
1989/8 - 1990/7	0.3	244	10,690

C. PROGRESS AND IMPROVEMENTS

1. INJECTION SYSTEM

1a. New High-Power Hybrid Attenuator & Phase-Shifter Systems

Two kinds of hybrid attenuator & phase-shifter systems have been newly designed and manufactured combining 3-dB hybrids and variable short plungers: One is for the prebuncher, and the other is for the buncher. Both of the two systems have the distinctive feature that they can change independently the attenuation and phase of the high power rf, and do not introduce an rf phase shift as the attenuation is varied. After introducing the new system, the process of converging on the optimum phase and power settings for the prebuncher and buncher were greatly improved (speeded up) by the new systems.

The former high-power variable attenuators had a problem in that a phase shift is introduced as the attenuation is varied. This feature made it complicated to search for the optimum parameters of the prebuncher and buncher. Accordingly, new systems were designed in order to solve this problem.

The old system for the buncher was pressurized with SF_6, so that it required windows which separate the gas from the vacuum. Bored holes with small cracks were found on the vacuum sides of the windows last Spring. Fortunately, the holes had not reached the other side. In order to avoid this kind of problem the new systems were designed to be used under a vacuum.

The new systems have the configuration illustrated in Fig. 1. Each system has two short plungers which move independently and simultaneously. By a 3-dB directional coupler, the rf power is first divided into two parts. After being phase shifted, they are combined by either the same or the other 3-dB coupler. When the phase shifts are the same, the system works as a phase shifter. On the other hand, when the phase shifts are equal but opposite, the system works as an attenuator. It is, of course, possible to simultaneously change the attenuation and phase, if necessary.

Figure 2 shows the microwave characteristics for the buncher system. It exhibits phase shifts over a frequency range when attenuations are changed: the phase shifts are shown in the upper part, and attenuations in the lower part. Figure 2 shows that the phase shifts are small over a power range of 0 ~ -20 dB. At a frequency of 2856 MHz, the phase shifts are less than ± 2°, as shown in Fig. 3.

S. Ohsawa

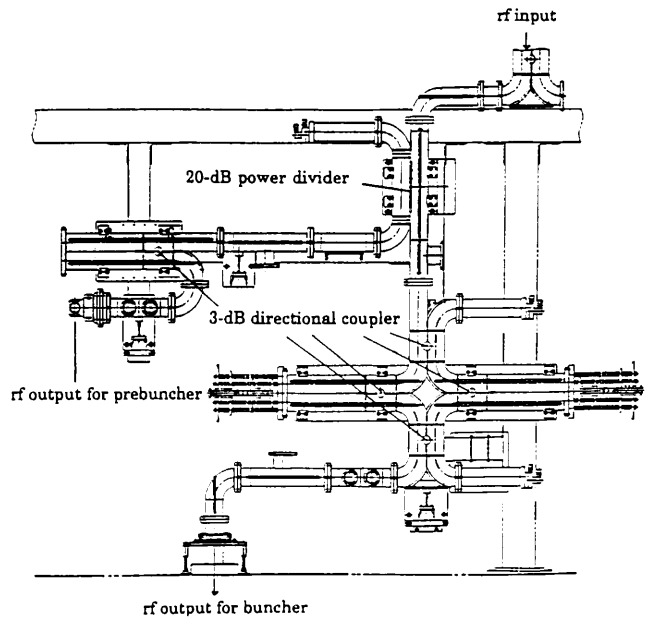

Fig. 1 New hybrid attenuator & phase shifter systems.

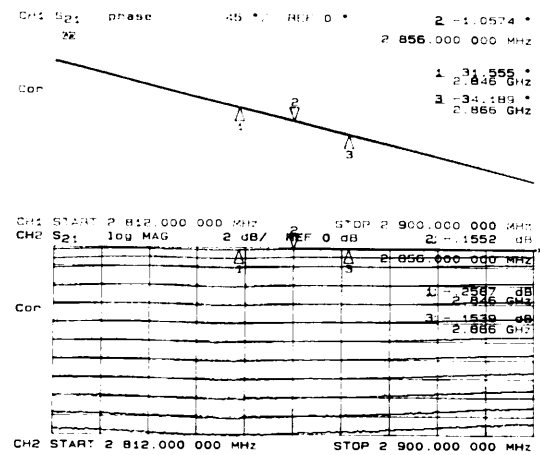

Fig. 2 Characteristics used as an attenuator.

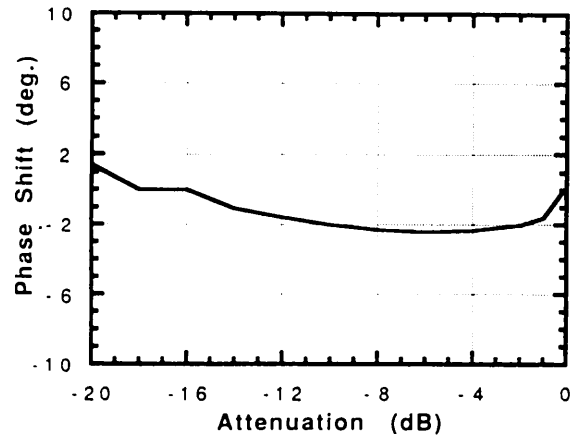

Fig. 3 Phase shift vs. attenuation at 2856 MHz.

1b. Improvement for the Gun High-Voltage Dome Control System

A new gun device controller (HV-dome Controller) has been constructed and installed in the floating decks (HV-dome) at a gun high voltage of 160 or 100 kV. It was developed to remote control and monitor devices at high voltage. It also has a function to protect the gun cathode by turning off its heater when the vacuum pressure is increased extremely.

The new controller uses a commercially available, general-purpose programmable controller with a microprocessor. A personal computer at ground potential is used to communicate with the controller through optical fibers, interchanging control commands and status signals for such equipment as the grid pulser, bias voltage supply and heater voltage supply as well as their interlock circuit. With another programmable controller for the gun vacuum system, both controlling and monitoring the entire gun system became possible through the computer network. It is also possible to obtain electron gun information at a long distance through CATV at any time. The entire system (illustrated in Fig. 4) is very useful in that we can always know the gun operational states.

M. Yokota

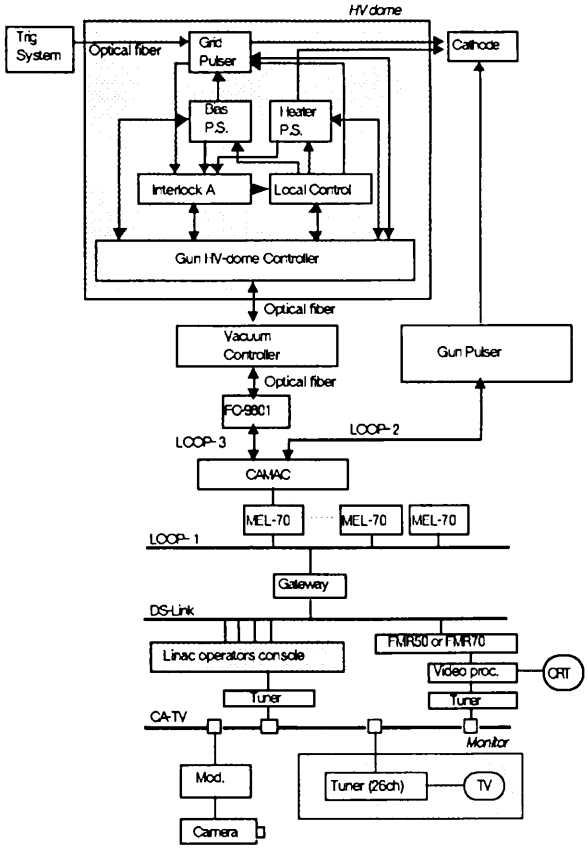

Fig. 4 GUN control system.

2. MICROWAVE SOURCE

Failures of high power klystrons are mostly caused by an arcing between the electrodes of the electron gun and a breakdown of the rf output window. During the last several years investigations concerning these phenomena were carried out and some improvements have been applied: the bake-out process, material choice and surface finish of the gun electrodes, cathode material, rf window material and TiN coating on the window surface. The use of a barium-impregnated (BI) cathode instead of an oxide cathode was one of the most effective methods to suppress the internal arcing of the klystron because of less electrode contamination.

2a. Operational Performance of Klystrons with a Barium-Impregnated Cathode

In FY 1987, a klystron with a BI cathode was developed, and up to FY 1990, 45 klystrons with a BI cathode have been produced. At present (July 1990), as shown in Table 4, 37 of them are working in the gallery, where 48 sockets and modulators are installed. They indicate a much longer MTBF (mean time between failures) than that of the oxide cathode ones. Table 5 shows the operational performance of the klystrons. During these three years, the contribution of the BI cathode klystrons to the total operation time increased by up to 67 %, and their fault rate has been 0.26/day·tube, which is a much lower value than that of oxide cathode klystrons. Consequently, the averaged applied voltage could be increased. The improved performance of the BI cathode klystrons has resulted in a stable, successful operation of the linac (about 14 times per day of klystron down trips for the whole linac).

Y. Saito & K. Nakao

2b. Further Improvement of the Klystron by Decreasing Surface Electric Fields in the Gun Electrode

The klystron gun was improved so as to decrease the surface electric field of the electrodes and to make higher applied voltages possible, while keeping the outer diameter of the housing the same as that for normal klystron gun in order to use the existing focusing magnets. The maximum surface electric fields could be decreased from 244 to 213 kV/cm for the beam focusing electrode, and 284 to 197 kV/cm

Table 4. Cumulative status of klystrons up to July 1990 corresponding to the year of production. Unused tubes are those which have never been used in the klystron gallery. STB (Stand-by) tubes are those which have been used in the gallery and can be used there again.

Year of production	Cathode	Total No. of tubes	Unused No. of tubes	Living No. of tubes	(STB working e^- e^+)	Av.op.time (hours)	Failed No. of tubes	Causes (arcing windows others)	Mean age (hours)	Cumulative operation (tube-hours)	MTBF (hours)
1979	oxide	4	0	0	(0 0 0)	——	4	(2 1 1)	3,900	15,600	3,900
1980	oxide	20	0	1	(1 0 0)	3,700	19	(13 5 1)	9,100	175,600	9,200
1981	oxide	20	0	5	(1 4 0)	27,600	15	(9 2 4)	11,400	309,500	20,600
1982	oxide	9	0	1	(1 0 0)	2,100	8	(5 2 1)	10,100	82,500	10,300
1983	oxide	13	0	4	(1 3 0)	24,300	9	(6 2 1)	15,400	235,300	26,100
1984	oxide	13	1	1	(0 1 0)	21,000	11	(10 0 1)	8,500	114,400	10,400
1985	oxide	12	1	3	(0 3 0)	20,200	8	(7 0 1)	8,400	128,000	16,000
1986	oxide	15	0	1	(1 0 0)	11,600	14	(13 0 1)	3,500	60,900	4,400
1987	oxide	7	0	0	(0 0 0)	——	7	(5 1 1)	4,300	30,400	4,300
1987	BI	7	0	6	(0 6 0)	12,300	1	(0 1 0)	10,200	84,200	84,200
1988	BI	20	3	16	(1 10 5)	8,800	1	(0 1 0)	8,200	149,200	149,200
1989	BI	18	2	16	(0 14 2)	3,400	0	(0 0 0)	——	54,400	>54,400
	oxide	113	2	16	(5 11 0)	20,900	95	(70 13 12)	8,600	1,152,300	12,100
	BI	45	5	38	(1 30 7)	7,100	2	(0 2 0)	9,200	287,800	143,900
	total	158	7	54	(6 41 7)	11,200	97	(70 15 12)	8,600	1,440,100	14,800

Table 5. Fault rate and applied voltage of oxide-cathode and BI cathode tubes during each one-year operation period.

Period	Fault rate (/day·tube)		Applied voltage (kV)		Total operation (tube-days)	
	oxide	BI	oxide	BI	oxide	BI
1982/8 - 1983/7	2.5	---	238	---	4,470	---
1983/8 - 1984/7	1.6	---	242	---	4,150	---
1984/8 - 1985/7	1.2	---	240	---	4,420	---
1985/8 - 1986/7	1.0	---	238	---	5,600	---
1986/8 - 1987/7	1.0	---	239	---	7,740	---
1987/8 - 1988/7	1.03	0.28	238	239	9,290	710
1988/8 - 1989/7	0.79	0.27	238	244	6,640	4,060
1989/8 - 1990/7	0.42	0.25	242	245	3,440	7,250
total (up to 1990/7)	1.15	0.26	239	244	45,570	12,020

for the anode at an applied voltage of 270 kV. However, decreasing the strength of electrostatic focus, which is necessarily caused by lowering the surface field while unchanging the perveance, requires an extension of the focal length, shifting down the cathode position by 16.3 mm (Fig.5). This extension of the gun length requires an extension of the magnetic field and a rearrangement of its distribution around the gun area. Figure 6 shows the magnetic field distribution which generates the highest rf power obtainable for the use of existing magnets without any modification, except for the pole piece mounted on the klystron (see Fig.5).

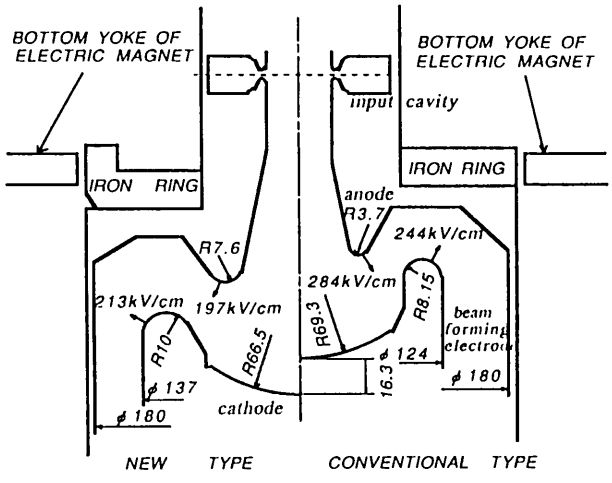

Fig. 5 Test dimension of the klystron gun housing.

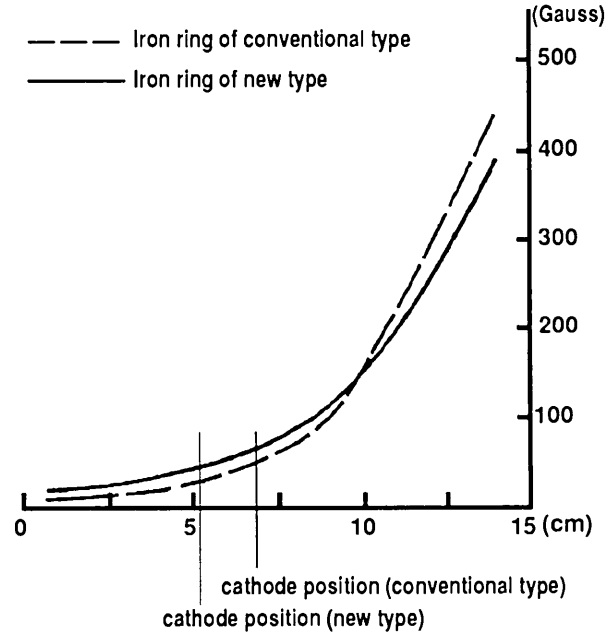

Fig. 6 Transverse magnetic field.

We obtained an output power of 39 MW and an efficiency of 46 % at a 277 kV cathode voltage, which was limited by the output power capability of pulse. The results are shown in Fig.7, and summarized as follows:

1, The maximum allowable cathode voltage is more than 280 kV.
2, Although the efficiency begins to decrease over a 260 kV cathode voltage, more than 45 % is still maintained for over 280 kV.
3, Although the magnetic field is not necessarily suitable for this improved klystron, we obtained an output power well above the objective value by using an existing magnet.

Since the maximum outer diameter of the gun is restricted to be 190 mm, we can not drastically decrease the surface field of the focusing electrode; it is therefore difficult to apply in excess of 290 kV to the cathode. However, a 40 MW output power may be achieved as practical operation values, even for this small-size klystrons.

Y. Saito & K. Nakao

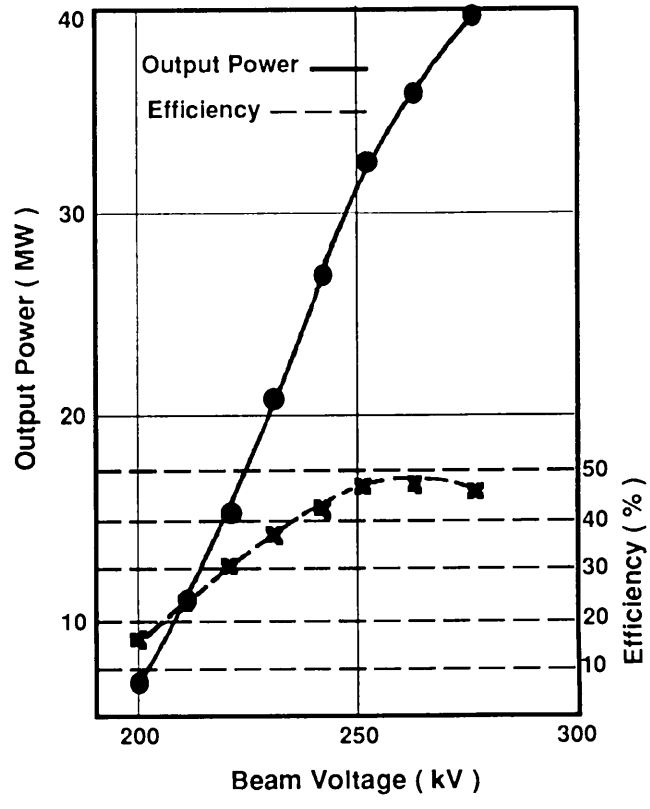

Fig. 7 Cathode voltage, output power and efficiency.

3. CONTROL SYSTEM

3a. Linac Control System Upgrade

The linac is controlled by a distributed processor network having nine minicomputers and hundreds of microcomputers. The system has operated well since its commissioning. However in order to maintain this reliable operation the control system should be upgraded within a few years. The main reasons are that the computer company won't continue maintaining the minicomputers and that there exist many requests for an increased functionality of the control system not included in the original design.

We are now planning the upgrade schedule and developing the required components. Not all of the system needs to be upgraded. We plan to replace the minicomputers (MELCOM 70/30) and the main network (LOOP-I) between them, since LOOP-I was exclusively designed for MELCOM70/30. Thus, the architecture of the main software will also be revised. Hundreds of local controllers, mostly managed by microcomputers, and LOOP-II/LOOP-III local networks, which transfer messages between local controllers and minicomputers, will continue to be used. In the new system we should adopt both software and hardware standards. If international standards are employed, we can utilize a large amount of software and hardware resources, making future upgrades easier.

As accelerators become larger, distributed processing in the control system is necessary. In the current system, although the network is used to transmit control messages, most of the control process is done on a minicomputer, called the console station. With a standard network protocol suite, it's possible to distribute a single process over the network. In the next control system we employ the media of Ethernet (IEEE 802.3) and the TCP/IP (DARPA) protocol suite for the main network. Unix workstations will be utilized to replace minicomputers.

For connections to the local controllers, a VME bus (IEEE 1014) will be employed to drive the LOOP-II/LOOP-III local networks. The LOOP-II/LOOP-III controller modules are under development. A VME bus may be utilized also for local controllers, themselves, in the future.

Basic software has already been developed, such as gateways between old and new networks. For message exchanges, a more generic format has also been defined and tested. For distributed processing, dynamic and static parameter servers, a locking server, an alarm server are provided. A method for remote procedure calls will be also utilized.

K. Furukawa & N. Kamikubota

3b. Improvements in DS-Link

The DS-Link (IEEE802.3 10BASE5 by FUJITSU Co.) system for the operator's console has been successfully and stably operated in the PF linac since 1988.

This system, especially the graphics, is programmed using BASIC interpreter language on the DS-Link with MS-DOS. Since the system reached the limit of file and memory size, several OS/2 multitask stations were linked to the MS-DOS server network system through the DS-Link. OS/2 provides more powerful tools for program developers.

Those OS/2 stations are mainly operated so as to monitor such linac devices as magnets, klystrons, vacuum, gun, etc. Although the MS-DOS stations in the operator's console are capable of executing a single task only, they can receive alarm signals from any OS/2 station and can display some statements on the CRT. This function was achieved without changing the existing application programs.

Computers FMR70HX3 (386CPU, 25 MHz, 16MB, FUJITSU Co.) and C language were used for OS/2 stations.

The server station of the DS-Link were also equipped a 300MB hard disk and 600MB MO (Magnetic Optical disk cartridge), enabling such large files as those containing waveform data.

A neural-net system for waveform diagnosis in a klystron pulse modulator has been tested on the MS-DOS station; after the test, it will be installed on the OS/2 station. The neural net has already learned six patterns of waveform and can diagnose it very quickly. After the diagnosis, the station can send some message as an alarm to an appropriate CRT display in the operator's console.

I. Abe

3c. Expert System for Electron Gun

Diagnosis and operation support using an Expert System (ES) of the phase-II project for the electron gun of the PF-linac injector has been developed on the basis of KMTS (Klystron Modulator Trouble Shooting system developed in 1989). The system is highly graphic, allowing rapid incremental development with direct access to the reasoning mechanism on a visual

thinking interface. Basically, this system has almost the same configuration as dose KMTS: HP9000/375, HP-UX, C, NEXPERT-OBJECT(shell), and Data-View (graphic tool).

From the experience gained during KMTS development, several points were modified and some features were added. Especially, knowledge taken from the domain and Knowledge Base (KB) manipulation or installation in the computer were the main subjects. The efficiency of the problem-solving task depends upon the quality of knowledge resources. The interface between the domain expert and the system was developed. In the first stage, a HyperCard system was developed for knowledge taking and problem structuring. When a new KB is added and tested for possible phenomena, the transparency of the stored KB would be the most important problem; therefore, this problem was solved in this project by making a tool program.

This ES station can access the computer network of the PF 2.5-GeV linac to receive real-time data.

At present, this ES has less than hundred rules concerning beam loss diagnosis. Knowledge about beam instability is going to be added as the next step.

I. Abe

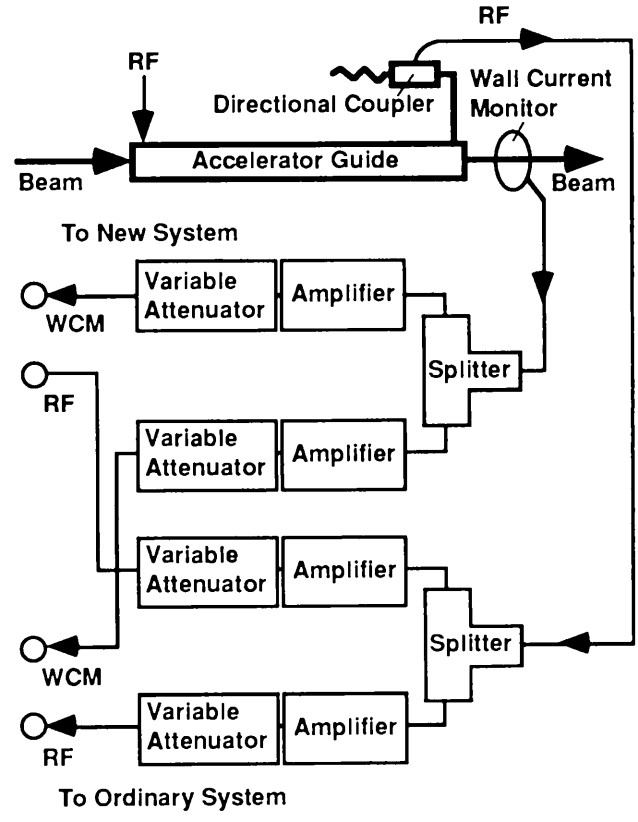

Fig. 8 Block diagram of the rf and beam timing monitoring system.

4. OPERATION GROUP

4a. Improvement of Starting Sequence of the Linac

The start-up procedure has been improved during this period. This has been effective for stable operation during long term. Fine adjustment of the timing between a microwave (rf) and a beam in accelerator guides is one of the steps in the newly established start-up procedure; improvements using a digitizing signal analyzer are described.

The optimum timing between the rf and the beam can be known from phasing data. The timing of an induced rf by the microsecond beam is compared with that of the rf for acceleration in the phasing process. After adjusting the timing of the microsecond beam, the timing of the short pulse beam is adjusted precisely by the newly developed system.

To upgrade the start-up procedure, it is necessary not to disturb the normal operation, as is usual with the 2.5-GeV linac. Both the rf and the electron/positron beam signal are divided into two. One is for ordinary operation, and the other is for the improved system. A block diagram of this newly developed timing monitoring system is shown in Fig. 8. Circuits are

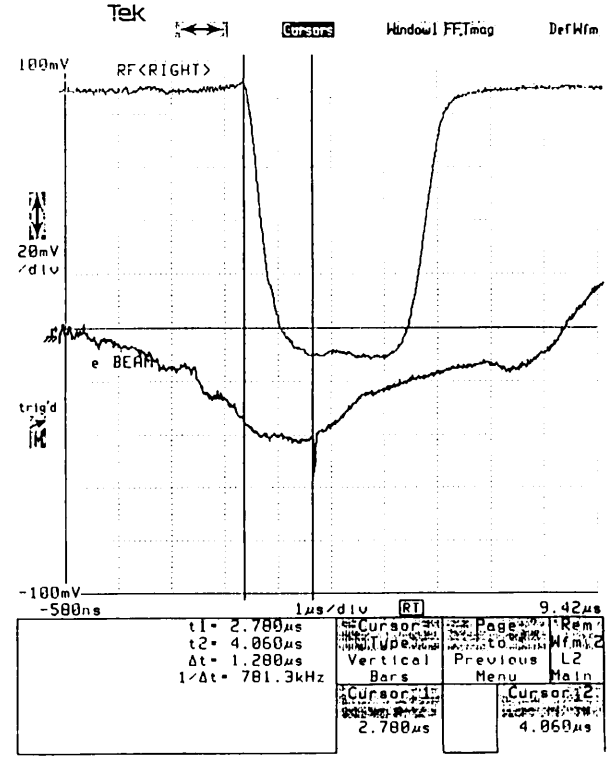

Fig. 9 An example of the timing between rf and positron beam.

composed of fast pulse amplifiers and variable attenuators. From an adjustment of the gain, the output amplitude can be made to be just the same as an input. The ordinary system is not affected by further developments of this new system; hardware and/or software. Figure 9 shows an example of the rf and positron beam waveforms measured by a digitizing signal analyzer (Tektronix DSA602). Using a cursor function, the timing between the rf and the electron/positron beam, beam amplitude , and other values can be measured digitally. Under usual operation, these values were measured from the divisions of an oscilloscope; it was rather ambiguous. Furthermore, the process was troublesome, because both a trace of very short pulses (nanosecond for beam) and that of long pulses (microsecond for rf) were observed with very much different brightness in one screen. Both waveforms were observed with same brightness in the digitizing signal analyzer. By memorizing the normal waveform in the digitizing signal analyzer, it is easy to compare the waveforms when trouble shooting.

T. Kurihara

5. POSITRON GENERATOR GRADE UP

The KEK positron generator has successfully provided positron beams to TRISTAN since 1986 and to the Photon Factory (PF) since 1988. In FY 1990, instead of energy-front studies in the TRISTAN PHASE-I experiment, high-luminosity operation of the colliding ring was started as PHASE-II. Furthermore, in a few years, a B-physics plan is eagerly expected to be realized as PHASE-III. In these experiments, additional positron beams are required in order to save the injection time; especially, the B-Physics plan requires roughly ten times as many positrons as the present beam produces. To meet such requirements completely, an integrated upgrade is necessary for the overall injector linac. An improvement of the focusing system started first; tests of a high-power klystron,which enables the primary electron energy to be increased, is being prepared. The improvement in the focusing system aims to increase the number of positrons by roughly twice.

5a. Reinforcement Plan of the Positron Focusing System

The positron beam is produced by a high-energy primary electron beam striking a positron radiator (heavy-metal target). The specific positron yield, n, for primary electrons with an energy E is approximately (for the forward angle) given by

$$n/E = (\mathrm{d}^2n/E\mathrm{d}\Omega\mathrm{d}P)\,\delta\Omega\,\delta P,$$

where $\mathrm{d}^2n/E\mathrm{d}\Omega\mathrm{d}P$, the measured specific yield at 0° normalized by E, has a moderate dependence on the target material and produced positron energy, and is considered roughly to be constant. Hence, the intensity of the positron beam is proportional to the number of primary electrons, the primary electron energy, and focusing parameters $\delta\Omega$ (the solid angle) and δP (the momentum width of the acceptable positrons). Increasing the primary electron number and energy is discussed separately.

The KEK positron generator adopts the QWT-type focusing system which has a solenoid field distributed as shown in Fig. 10. A strong short-range axial field, B_i (effective length L), just behind the radiator is produced by a pulsed solenoid; it is followed by a lower field, B_f, applied over the accelerator sections. Using the analytical expression for an ideal QWT field distribution, the solid angle and the momentum acceptance for the positron beam are expressed by

$$\delta\Omega \propto L^{-2}$$
$$\text{and } \delta P \propto B_f L.$$

Therefore, the following conclusion is introduced for improving the focusing system: (1) For a larger solid angle, it is necessary to fabricate a shorter pulsed solenoid; the strength, B_i (times L), determines the acceptable positron momentum, P. It is preferable that B_i be higher, since it suppresses any debunching effects due to the speed and orbit differences of positrons. (2) For a wider momentum acceptance, it is effective to make B_f stronger. (3) The positron yield is proportional to B_f / L.

A. Enomoto

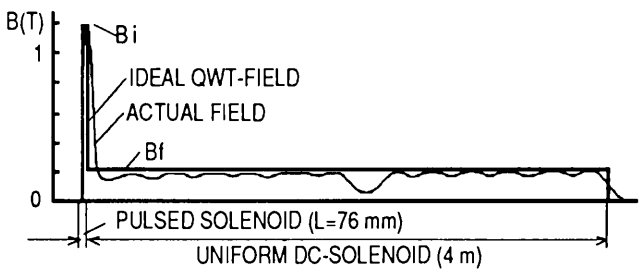

Fig.10 Field distribution of the position focusing system at KEK (before improved).

5b. Beam Optics of the Quadrupole Magnets

Upgrade of the quadrupole system after the solenoid is described here. To match the solenoid system, the layout of the quadrupole system was also changed so as to enlarge the acceptance of the system (Fig. 11). The previous beam-transport system consisted of a simple periodic quadrupole triplet system (Fig. 11 (a)). In the new system, a FODO system is used in the P–5 unit and the triplet system is improved to have larger acceptance in the P–4 and P–6 units (Fig. 11 (b)).

The P-4 unit consists of a quadrupole triplet focusing system. A beam separator is also placed between the triplets. It separates positrons from electrons which are also generated in the radiator and transported through the solenoid coil. In the previous system, both electrons and positrons were transported down to the 30-degree bending magnet at the end of the P-6 unit. The positron beam current was inaccurately measured due to cancellation by electrons.

In order to obtain a larger acceptance in the P-5 unit, quadrupole magnets were placed not only between the accelerating structures but also halfway between them. The bore radius of the quadrupoles was designed to be sufficiently large to place the accelerating structure in the bore. A strong magnetic field is required on the pole face when the bore is large. A FODO focusing system is used because it requires a smaller magnetic field gradient than does a doublet or triplet system, and it loosens the design requirements on the magnets.

The P-6 unit consisted of triplet focusing system similar to the previous one in which quadrupole triplets are located between the accelerating structures. The four-meter long structures used previously were replaced by structures two meters long. The distance between triplets becomes shorter and the acceptance becomes larger.

After the P–6 unit, positron beams are transported into the KEK 2.5-GeV main linac through a 30-degree bending achromatic transport system comprising two bending magnets and ten quadrupole singlets. No improvement in the achromatic system was made since the system already has a sufficient acceptance. This is because the maximum beam size in the achromatic system is determined dominantly by the energy spread rather than by the beam emittance.

Using the computer code TRANSPORT we have confirmed that the upgraded system has an acceptance more than 0.30 π (MeV/c)(cm) which is twice as much as the previous value. The code can optimize the quadrupole strength of the magnets for a beam to pass through the transport system with a finite beam size. Figure 12 shows the change in the size of positron beam with an emittance of 0.30 π (MeV/c)(cm) in the system with optimized parameters. It shows that the beam can pass through the transport system with a beam size smaller than the apertures of the components (~ 2 cm).

T. Kamitani

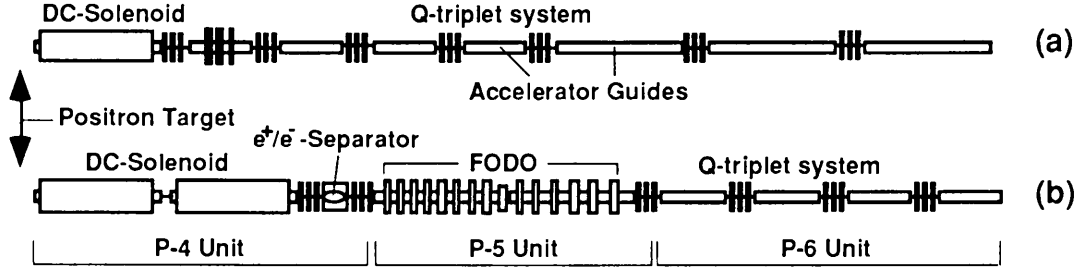

Fig. 11 Change of the positron generator layout from the present (a) to the improved one (b).

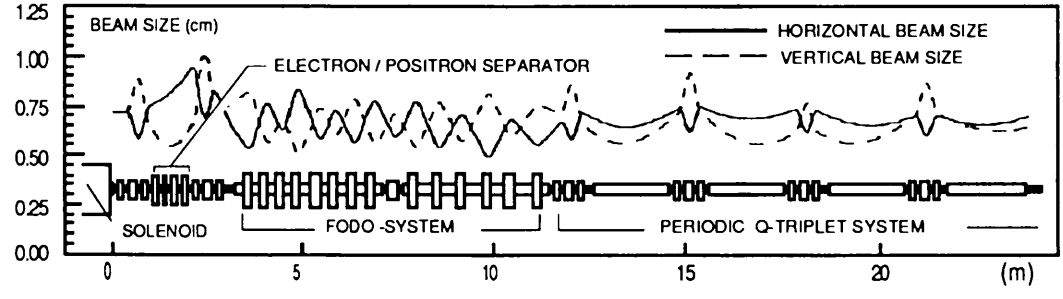

Fig. 12 New configuration of the reinforced positron generator focusing system and calculation of the matched beam using the computer code TRANSPORT.

5c. Newly Fabricated Long Solenoid

The maximum field for B_f excited by the present solenoid is 2 k Gauss (0.2 T), because of the cooling problem. A newly designed solenoid consists of 224 double pancakes, using a hollow conductor of 14 × 14 mm^2 (t 4.5 mm); it is directly water-cooled and produces 4 k Gauss (0.4 T). However, a coil using such a thick wire has disadvantage in producing a symmetrical field. Each pancake was therefore carefully fabricated in order to produce a field as uniformly as possible; each one has a return-yoke of low-carbon steel; intersecting points of the layers are made so as to be distributed at four points (a,b,c,d) throughout the entire length of the solenoid (Fig. 13).

In the next period, the solenoid will be assembled and installed, together with bridge-coils to compensate for field dips due to waveguides located behind the target and between the 4-m accelerator sections.

T. Oogoe

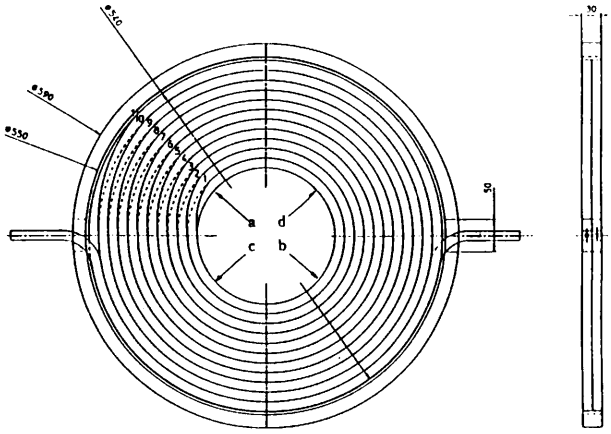

Fig. 13 Structure of a double-pancake for the long DC solenoid.

5d. Improvement during this Period

A two-stage reinforcement of the KEK positron generator focusing system will be performed (Table 6). At first, using the present pulsed solenoid, the DC-solenoid (B_f) will be reinforced from 0.2 to 0.4 T. In this condition, though, the solid angle will not be changed, the momentum acceptance thus increases. As for the matching condition of the beam on the radiator, the beam radius may be twice as large as the present radius; this means that beam adjustment on the target becomes rather easy. In the next stage the pulsed solenoid will be improved.

Table 6. Parameter change of the QWT system.

	Present	Step 1	Step 2
Solenoidal field			
pulsed solenoid B_i (T)	1.2	—>	2.0
effective length L (mm)	76	—>	50
DC solenoid B_f (T)	0.2	0.4	0.4
Acceptance			
U (π(MeV/c)(cm))	0.15	0.30	0.30
Matched beam on the radiator			
radius x (cm)	<0.12	<0.24	<0.14
momentum P (MeV/c)	8.7	—>	9.5
transverse momentum p (MeV/c)	1.25	—>	2.1
Positron yield (relative values)			
solid angle $\delta\Omega$	1	—>	2.3
momentum acceptance δP	1	2	1.3
specific yield n/E	1	2	2.4

During the 1990 summer shutdown, the P5 and P6 units were completely reconstructed according to the new design. The quadrupole triplet system was replaced by the FODO system in unit P5. However, the improvement of P4 unit just behind the positron target will be performed during the next winter shutdown, since the accelerator sections which fit the new solenoid structure will be completed at the end of 1990. Computer simulations show that the new quadrupole system also matches the old solenoid system.

T. Oogoe & K. Kakihara

D. RESEARCHES

1. TEST LINAC

As was described in the last issue, construction of the test linac has already started. During this period, one part of the electron gun room of the 2.5-GeV linac was partitioned by concrete blocks with a thickness of 1 meter; a room 18 meters long by 4.5 meters wide has been prepared for the test linac. A universal bed with a length of 13.5 meters was installed in the room. An electron gun, a prebuncher, a buncher, a regular accelerator guide and the other components shown in Fig.14 have been installed on the bed. Other necessary components such as a klystron modulator, a high-voltage source for the electron gun, a vacuum system, a safety interlock system similar to that of the 2.5-GeV linac, and waveguides from the klystron to accelerator guides were installed during this period.

At the beginning, experiments will be focused on the development of high-brightness electron guns. An electron gun with a very small cathode diameter of 1 mm is being developed. A calculation using the code developed by Herrmannsfeldt and the fabrication of the electron gun based on results of the calculation have

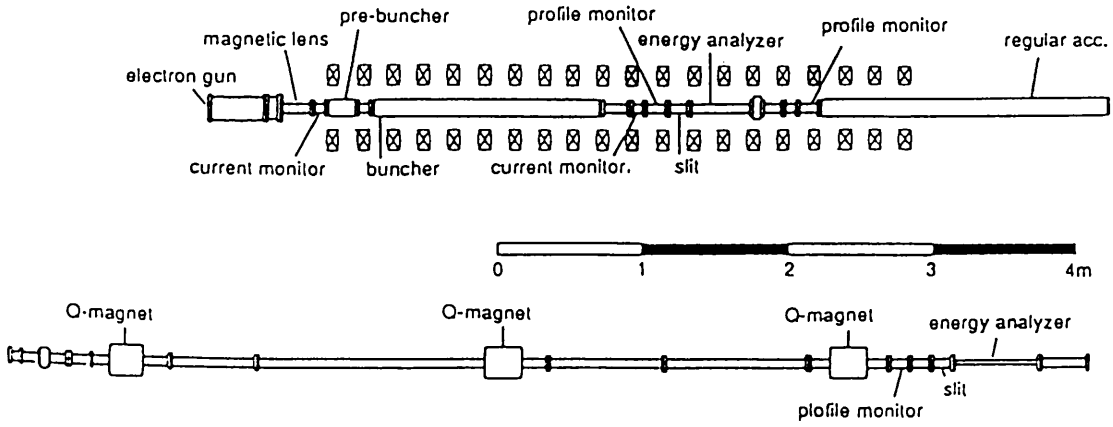

Fig. 14 Components installed on the universal bed of the test linac.

been completed. In the calculation, the entire area of the gun is divided into 4 blocks along the z-axis. One mesh size is 0.1 mm by 0.1 mm and 6400 points are calculated in each block. A calculated ray-trace in the gun is shown in Fig. 15. Emittance of 1.1 π mm-mrad at the current of 600 mA is obtainable according to the calculation. Experiments have just started.

T. Kurihara & H. Kobayashi

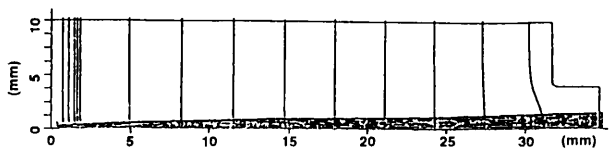

Fig. 15 Ray-trance of the gun. The beam slightly diverges in the gun.

2. NEW ALIGNMENT SYSTEM

In future linear colliders, an extremely small beam size (nanometers) will be required at the collision point to increase luminosity. It involves an elaborate final focus system with a precise alignment technique of the magnets and their support in a range of distances over several hundred meters. In order to realize this nanometer alignment system over a long distance, we introduced an ultra-precise laser interferometer technology, which had been developed in gravitational-wave experiments. Several kinds of interferometer noise limiting the sensitivity were examined on the basis of a sensitivity theory regarding laser interferometer for gravitational waves.

Preliminary experiments were carried out on a long-arm interferometer in air (Fig. 16). The arm length is about 80 m and a frequency-stabilized 0.7 mW He-Ne laser is used as a coherent light source. The optical configuration is arranged so that the beam reflected back into the laser does not disturb its stabilization system. The interference pattern was observed on a screen, indicating a large fluctuation which seems to be coupled with environmental acoustic noise and the fluctuation of the air in the light path. We plan to prepare a long vacuum system to diminish these effects.

In a linear-accelerator alignment, a transverse displacement with respect to the beam direction must be measured precisely. In order to utilize laser interferometer for this purpose, an optical system with phase-conjugate mirrors was proposed and is now under experimental investigation.

Y. Ogawa & K. Furukawa

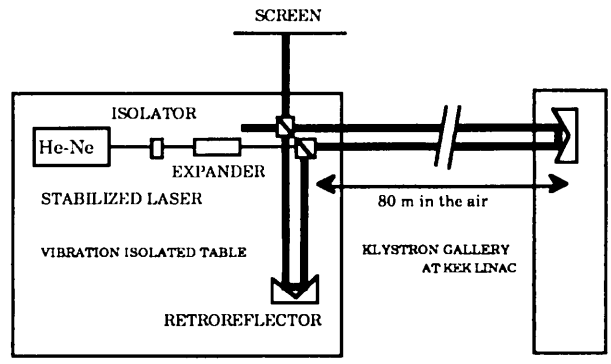

Fig. 16 Preliminary experiments on a long-arm interferometer in air.

3. NEW ACCELERATOR STRUCTURE

A new type of traveling-wave linear accelerator structure is being developed. This structure is like a

disk-and-washer structure, but it is simpler than that. There are no protrusions in the inner surface of the cylinder. The washers, without noses, are like disks. Between the disks and cavity wall there are coupling slots. In other words, we cut the round coupling slits on the disks in the disk-loaded structure.

This structure has a high shunt impedance, high group velocity, high Q value and low attenuation. Therefore, this structure with traveling wave resonant ring has high efficiency. Especially, for a large beam current and CW linac its efficiency can reach as high as 90 %. We thus call it HELAS (High Efficiency Linear Accelerator Structure).

In addition, it has an important characteristic: its TM_{11}-like mode is not a backward wave, but a forward wave. Its Brillouin diagram is shown in Fig. 17. It has a high threshold current of beam breakup (BBU).

The theoretical study was performed using computer codes of SUPERFISH and MAFIA. Some experiments have been carried out. The experimental and theoretical results are in agreement.

Y. L. Wang & I. Sato

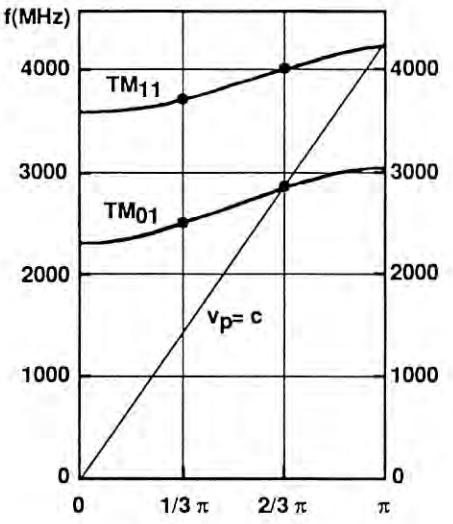

Fig. 17 Brillouin diagram of HELAS.

4. WAKE-FIELD IN MULTI-BUNCH SHORT PULSE

A multibunch instability due to a transverse wake field is considered to be one of the crucial problems related to future linear colliders. Although this transverse effect has already been investigated both theoretically and experimentally in the case of a single bunch, no multibunch instability has been directly observed so far, except for beam break-up (BBU) or pulse-shortening effects for a very long train of bunches, where only the beam loss was observed. We directly observed the multibunch instability at the primary electron section of the positron generator linac.

An intense electron beam of a peak current of 10 A with a pulse width of 2 ns, which corresponds 5-6 bunches with a charge of several nano-Coulomb, is accelerated to 250 MeV at the primary section of the positron generator linac. The accelerated multibunch beam was deflected at the energy-analyzing station in front of the positron conversion target; its beam profile was then measured at the screen monitor, indicating the multibunch structure due to beam loading effects. The last bunch was deflected vertically (transversely) when the initial offset (vertical) of the beam position at the entrance of the first accelerator guide was given (Fig. 18(a)). The displacement of the last bunch was found to be proportional to the initial offset (Fig. 18(b)).

We performed several tests to confirm that the observed effect is caused by the transverse wake field: a check of the beam optics, the dependence on the charge per bunch etc. A rough estimation based on Wilson's two-particle model was also made, which explained the effects semi-quantitatively. A more rigorous numerical analysis is presently being carried out.

Y. Ogawa & T. Shidara

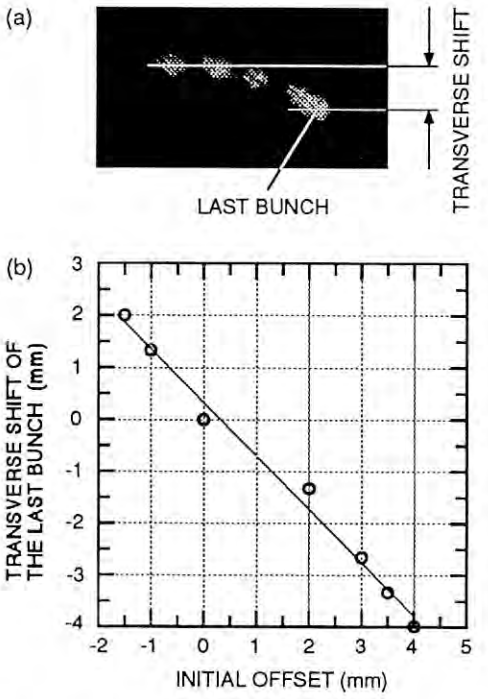

Fig. 18(a) Transverse (vertical) shift of the last bunch observed at the profile monitor at the energy-analyzing station.

(b) Transverse shift at the end of the accelerator as a function of the initial offset. The sold line shows a least-squares fit.

5. PLASMA WAKE-FIELD ACCELERATOR EXPERIMENTS

The plasma wake-field experiment, which was started last period, has continued in order to investigate more precisely and at higher plasma-densities. The main improvements are as follows: (1) The tungsten multi-filament cathodes were replaced by 4 lanthanum hexa-boride (LaB_6) cathodes, thus increasing the plasma density from approximately 10^{11} to 10^{12} cm^{-3}. (2) By solving a radiation safety problem, full acceleration of the electrons throughout the positron generator linac became possible; the electron energy was then raised from 250 to 500 MeV. This made the beam size smaller, decreasing multiple scattering at the beam windows. Other beam conditions were similar to those for the last experiments; 2-ns pulse with several (6 or 7) bunches, roughly 5-nC total charge, etc.

The energy spectrum of each bunch passing through the plasma chamber was measured with a bending magnet and a streak-camera system. Typical spectra of the bunches with maximum charge are shown in Fig. 19, where the data given by the solid line was obtained in the presence of a plasma with a density of 9×10^{11} cm^{-3}, and the dotted line without plasma (a) and in a plasma off the resonance (b). The energy shift of the bunch, defined by the difference of the mean energy between two conditions, is about 12 MeV. The observed plasma density dependence is shown in Fig. 20. The first resonance around a density of 4×10^{11} cm^{-3} was observed again as in the last experiment and a second resonance around 9×10^{11} cm^{-3} was observed in this experiment. This dependence agrees with a calculation using a linear two-dimensional model.

A. Enomoto

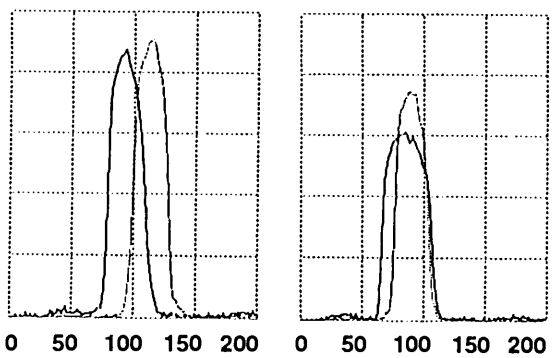

Fig. 19 Typical energy spectra, .547 MeV/ch. (a) Those of the bunch with the maximum intensity. (b) Those of the bunch just after the one with the maximum intensity. Solid line: in the presence of a plasma with the resonant density. Dotted: without plasma (a), in a plasma with density off the resonance (b).

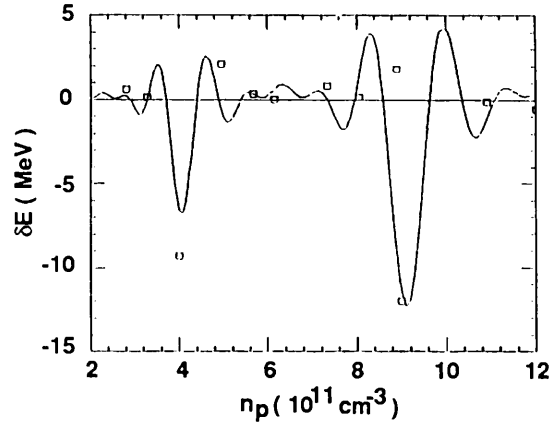

Fig. 20 Observed plasma density dependence of barycenter energy shifts of the maximum bunch.

6. CHANNELING RADIATION EXPERIMENT

Using the new beam line constructed in the last period, the channeling radiation measurement started in the autumn of 1989. A 2.5-GeV positron beam, which is expected to radiate about 8-MeV photons in a silicon crystal, was deviated to this beam line. Two lead collimators, which have 2 mm ϕ and 1 mm ϕ apertures each and are separated by 6.8 m, restrict the beam divergence within the critical angle for channeling. A 330-μm thick silicon crystal was installed in a goniometer so that the beam was parallel to the <001> axis. In order to search for a channeling axis quickly, the scattered-positron distribution was measured. When channeling occurs positron scattering decreases and the forward positron transmission increases. Figure 21 shows the first observation of this effect. As a next stage we plan to measure the photon spectrum and polarization.

A. Enomoto

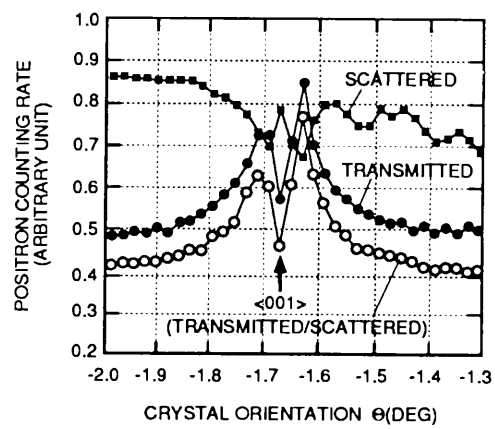

Fig. 21 Channeling radiation phenomena observed using a 2.5-GeV position beam incident in parallel to the <001> axis of a 330-μm thick silicon target.

Light Source Division

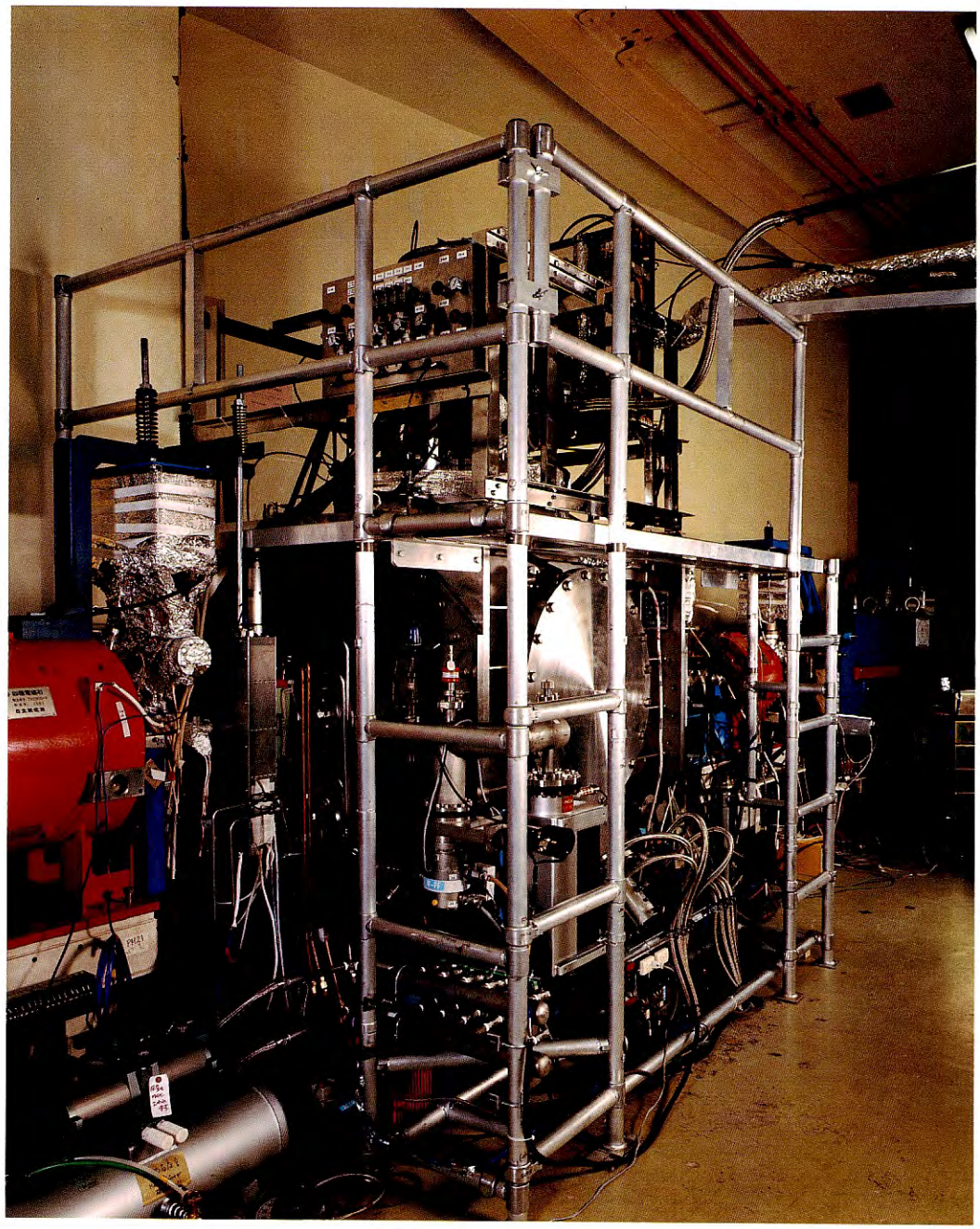

New 5-pole, 5-T superconducting vertical wiggler installed in the PF ring.

CONTENTS

LIGHT SOURCE DIVISION

A. INTRODUCTION

Movements of the photon-beam axes disturb user experiments in the Photon Factory. In particular, after the reduction of emittance of the circulating beams in 1987, such movements were emphasized. Efforts have been carried out for stabilizing the movements, and great progress has been made this year; movements were largely suppressed through (1) thermal insulation of the building roof, (2) improvement in the temperature regulation of cooling water, and (3) operation with a high betatron tune. Moreover, the beam lifetime was increased by a factor of two by using modified optics which have a low betatron function at the long straight sections where the vertical aperture is the smallest in the ring.

Late this year, an in-vacuum-type undulator was installed at beamline NE3 of the TRISTAN AR. Light from the undulator was observed on December 17, 1990.

A study regarding the use of the TRISTAN MR as a synchrotron-radiation source is in progress. Present tasks include the extraction of the large capabilities of the MR as a light source and a plan to convert the MR to an extremely-high-brilliance source. The implementation of new optics can lead to a very low emittance; high brilliance and coherent radiation would then be obtainable. The MR has four 200-m straight sections where long undulators can be installed; self-amplification during a single pass in the soft X-ray region can therefore be expected. These special features are unattainable for other existing plans involving next-generation rings.

A design study for a next-generation ring using the VUV and soft X-ray regions started this year. The beam energy is to be 1.5-3 GeV and the circumference of the ring 480 m.

Preparation work for the FEL project has started; this project involves research for developing the shorter-wavelength region. A gain measurement in the 200-nm region using the PF ring is our present goal. A high-quality beam under low-energy operation is essential for this project. In a preliminary study, a peak current of 20 A was observed with 0.8 GeV-operation.

SUMMARY OF STORAGE RING OPERATION

During the scheduled shutdown from August to October, 1990, modifications and maintenance related to vacuum components were carried out and 2/3 of the vacuum ducts of the storage ring were vented to the atmosphere. In six front-ends, bad vacuum components were replaced. The front-ends of beamlines BL-20 and BL-27 were installed during the shutdown. An RFQ was installed in the straight section between B4 and B5 for the suppression of transverse instabilities

Figure 1 is a plot of $I\tau$ (beam current × lifetime) obtained during user runs in July of this year. The average value is 900 Amin. It was 400 Amin last year; the lifetime is limited mainly by beam loss due to Coulomb scattering with residual gas in the MPW#16-duct, which has the narrowest vertical aperture in the storage ring. In an operation with optics with a low

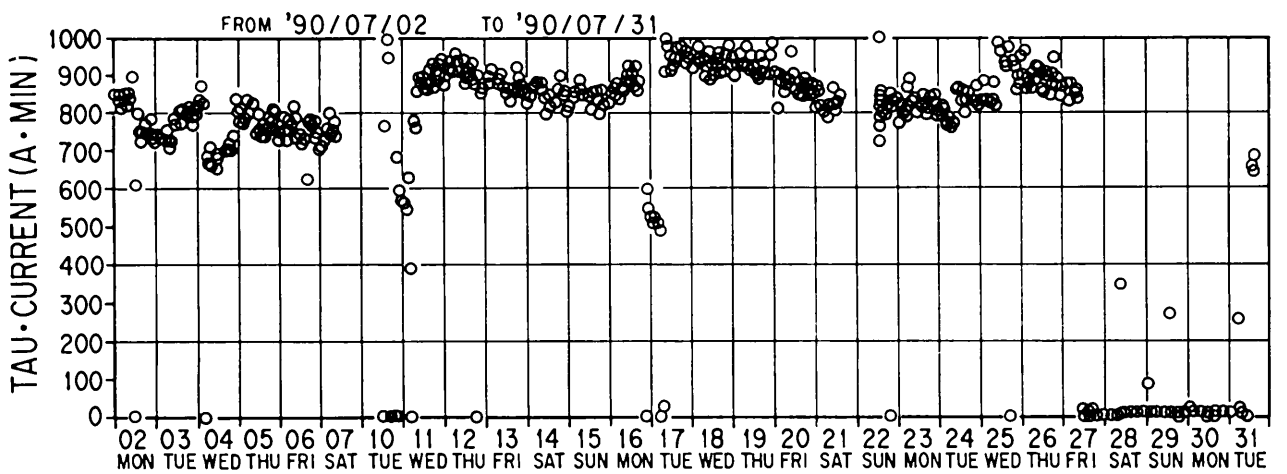

Fig. 1 Plot of $I\tau$ (current × lifetime) from July 2 to 31, 1990.

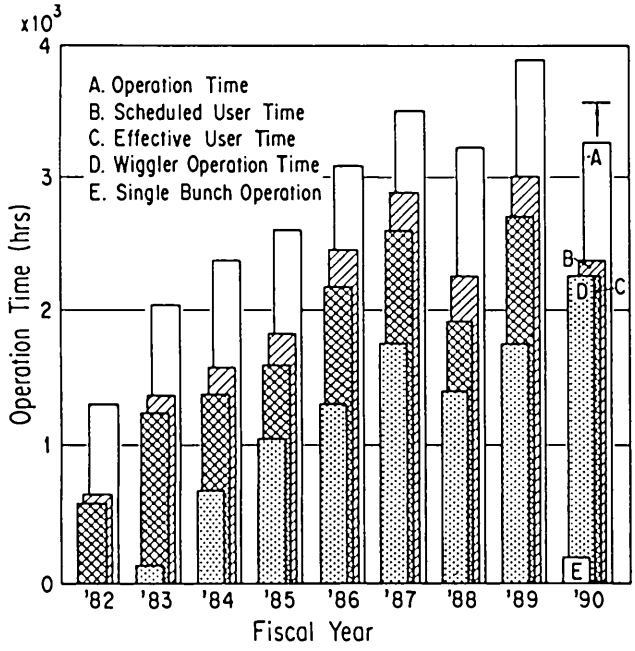

Fig. 2 Operation times of the storage ring from April 9 to December 25,1990.
A: Total operation time.
B: Scheduled user time.
C: Effective user time.
D: Wiggler operation time.
E: Single bunch operation.

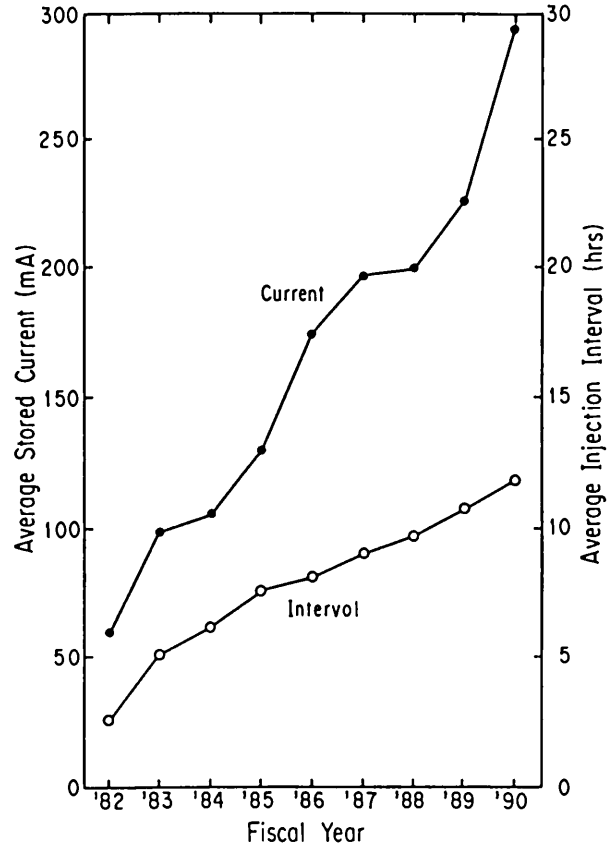

Fig. 3 Average stored currents and injection intervals.

betatron function at the location of MPW#16, the beam lifetime increased by 100%. After a re-measurement of the parameters of the correction magnets necessary for gap-tuning of insertion devices, operation with the new optics started in April, 1990.

A summary of the operation times of the storage ring is given in Fig. 2. The injection intervals and average currents are illustrated in Fig. 3. The initial stored currents are 350 mA and the beam lifetime is 50 hours at 300 mA. The average stored current is more than 300 mA during 12-hour operation and 280 mA during 24-hour operation. During this year, 187 hours (8.3% of the user time) was provided for single-bunch users. This was the first time to use a single-bunch beam for user experiments at the Photon Factory. The maximum single-bunch current is limited to 70 mA due to a rise in pressure in the isolation-valves and the bellows within the ring. The beam lifetime at 30 mA is 5 hours, which is limited by both the Touschek effect and the vacuum pressure rise. Progress has been made in reducing the population of unwanted positrons in adjacent buckets; scrapers installed in the section between B4 and B5 kicked out positrons with abnormal trajectories. Table 1 shows the operation statistics between April 9 and December 25, 1990.

The drift of the photon beam axes during the daily period is the largest, and is related to thermal distortion within the Light Source building. In order to eliminate this effect, we provided thermal shieldings by covering the building roof with 50 mm-thick urethane-foam mats. This work took two months and completed (January 1990). After installing the insulation, the drift was reduced to 1/5. Drift due to temperature changes of the cooling water was about 100 μm at 10 m from the source point. After improving the temperature-reguration system this summer, the drift

Table 1. Statistics of storage ring operation between April 9 and December 25,1990

Ring Operation Time (hr)	3256.0
Scheduled user time (hr)	2376.0
Net user time: T (hr)*	2254.0
Time spend for injection (hr)	91.3
Integrated current in T (Ahr)	661.2
Average current in T (mA)	293.4
Number of injection	196
Interval between injections (hr)	11.5

* Except single-bunch user time of 187.1 hours.

Table 2. Movements of photon beams in μm observed with an X-ray position monitor at BL-4C.

	Low Emittance (87.2)	Global Feedback (89.11)	Thermal Insulation (90.1)	Water Temperature Regulation (90.10)	High Betatron Tune (ν_y=3.3) (90.11)
Thermal distortion of the building	1000	300	170	→	70
		No Feedback	220	→	80
Water temperature	80	→	→	25	8
Tristan cycle	90	→	(90)	→	30

decreased significantly. The photon axes are three-times more stable during operation with a vertical betatron tune of 3.3. After carrying out crucial tests before changing the optics for user runs, operation using this optics started on October 30,1990. Table 2 is a summary of the photon-axis movements observed at BL-4C.

Undulator #2, which had been operated from 1983 at beamline BL-2, was removed from the storage ring in December, 1989. After significant modifications the undulator was reinstalled in May, 1990. The upgraded-undulator has the same periodic structure as that of the old one; the period length is 6 cm and the number of periods is 60. The magnet configuration (a pure type with $SmCo_5$ in the old one) was changed to the hybrid type with NdFeB permanent magnets and NEOMAX35H. Since the maximum magnetic field is 0.45 T, the lowest photon energy of the first harmonics is 270 eV (it was 400 eV). The uniformity of the magnetic field has been greatly improved to 0.1% (it was 0.7%).

Tuning the magnet gaps of the insertion devices causes a small drift in the beam-orbit and, thus, the photon-beam axes; this small drift disturbs user experiments. Efforts for free-tuning are now progressing; the parameters of the correction coils of each insertion device were carefully measured. At present, however, such weak field devices as undulator #2, the undulator mode of MPW#16 and the multi-undulator #19D are available for free-tuning.

The installation of an in-vacuum-type undulator was carried out in the straight section between bending magnets NE2 and NE3 in the TRISTAN AR. We observed the first photon beam on a fluorescent screen at beamline NE3 on December 17, 1990. Figure 4 is a copy from the logbook, depicting the first observation of undulator light. The operating energy was 6.5 GeV, and the storage beam current was 0.04 mA.

H. Kobayakawa

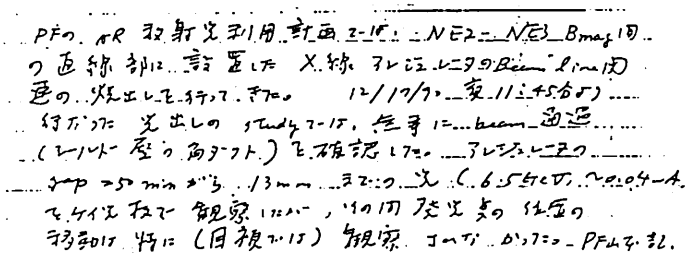

Fig. 4 A copy of the logbook depicting the first observation of light from an in-vacuum-type undulator at beamline NE3 of the TRISTAN AR.
"As PF project of using synchrotron radiation from AR, we have been working on conditioning the beamline for the x-ray undulator installed in the straight section between NE2 and NE3 Bending Magnets. In our study from 11:45 p.m. on December 17, 1990, we observed undulator light going through the beamline including the square duct in the shield wall. Changing the gap of the undulator from 15 mm to 13 mm (6.5 GeV, ~0.04 mA), we observed undulator light on a fluorescent screen. During that time we found the light-axis did not move on the screen.(S. Yamamoto)".

B. OPERATION

1. A NEW OPERATING POINT

The orbit movements for various time scales have been observed. In particular, movement during a daily period is most serious. The orbit can be presently stabilized by correcting the COD every 30 min. However, movements in time scales shorter than 30 min cannot be corrected using this method.

As is well known, the amplitude of COD is proportional to $1/\sin(\pi\nu)$, with ν being betatron tune. Until July, 1990, the ring had been operated with betatron tunes of $(\nu_x,\nu_y)=(8.41, 3.11)$. The use of ν_y closer to a half integer (3.5) was expected to result in smaller vertical orbit movements. We surveyed the betatron tunes and found a new operating point (8.45, 3.30) where the injection rate and the beam lifetime were as good as that of old ones. This operating point was expected to yield a reduction in the orbit-movement amplitude by a factor of 2.4. The user run was started with the new operating point in October, 1990. Preliminary data show that the movement has been reduced, as expected. In addition, the vertical dispersion function, which has the same tune dependence as COD, has also been reduced.

M. Katoh

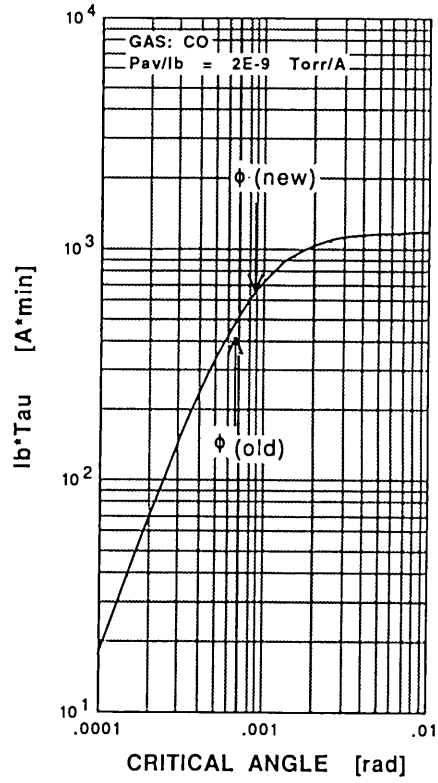

Fig. 5 Estimate of the beam lifetime as a function of the critical angle (ϕ_c). The beam lifetime is expressed by the product $I_b \cdot \tau$.

2. MODIFICATION OF BEAM OPTICS

Coulomb scattering by residual gas molecules is the dominant process of beam loss. In such cases, the beam lifetime strongly depends on parameter ϕ_c, which is expressed as

$$\phi_c = \mathrm{MIN}[\phi_i], \quad \text{and} \quad \phi_i = a_i/\sqrt{\beta_{av}\cdot\beta_i}\,.$$

Here, a_i and β_i are the half width of the aperture and the betatron function at a given place in the ring. β_{av} is the betatron function averaged over the ring circumference; this equation means that the place where ϕ_i is smallest limits the beam lifetime. In the original low-emittance optics, ϕ_i took the smallest value of 6.6×10^{-4} at the location of MPW#16. The beam optics were modified in order to improve the beam lifetime. Using the new optics, the betatron function at MPW#16 was reduced to 5m, from the previous 13m (for this reason, the new optics are conventionally called "low-β optics"). This modification results in the smallest ϕ_i of 8.5×10^{-4} at the location of MPW#13 and Revolver#19. The beam lifetime was expected to be improved by 35% (Fig.5). User runs with this new optics started in April, 1990.

It was found that the beam lifetime was improved by about 50% (Fig. 6), slightly larger than expected.

Although the beam emittance was not changed by this modification, the brilliance of synchrotron light on some beam lines was expected to significantly change due to changes in the betatron functions. In many cases the brilliance was increased as shown in Fig.7.

M. Katoh & Y. Hori

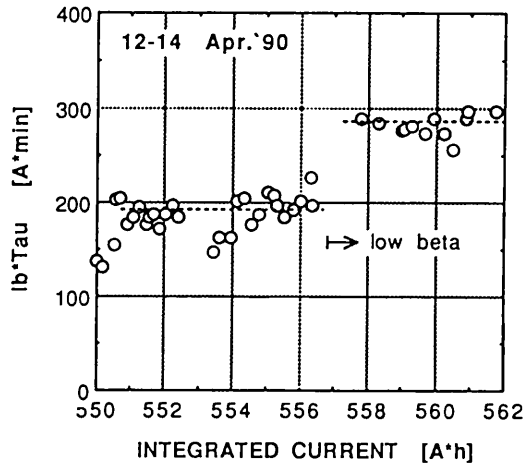

Fig. 6 Changes of $I_b \cdot \tau$ before and after the modification of the beam optics.

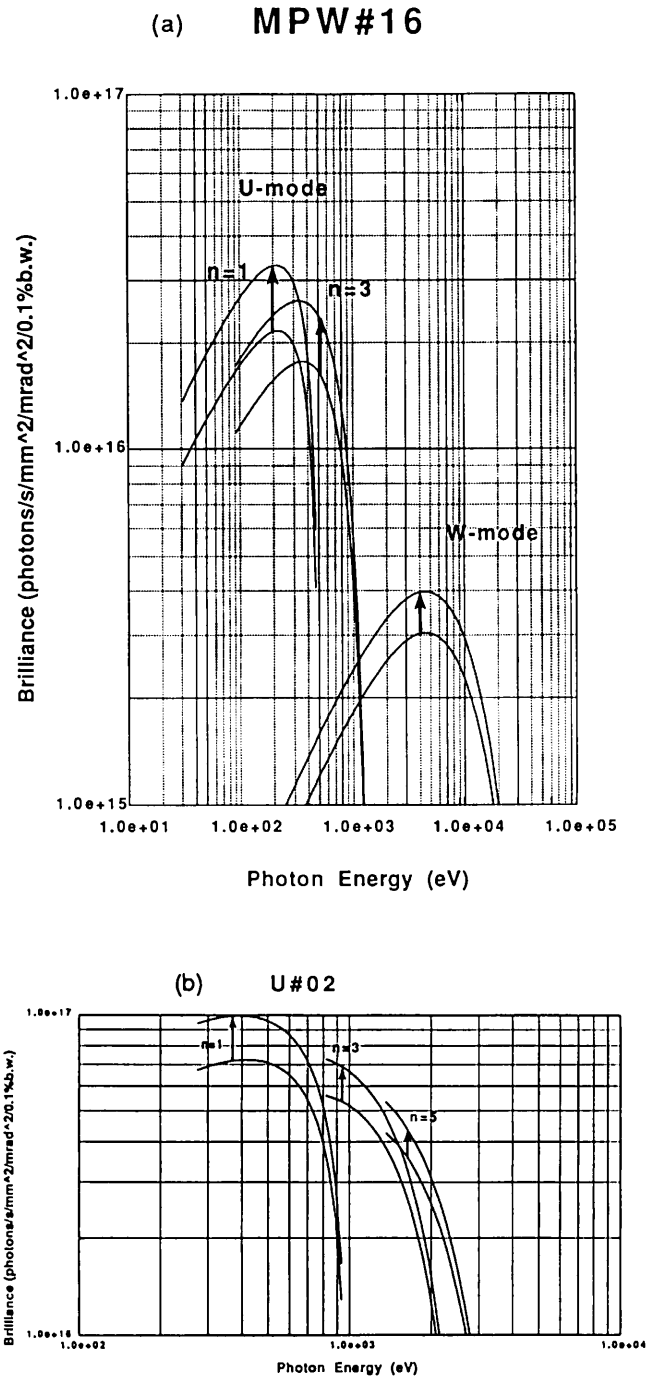

Fig. 7 Expected changes in the brilliance of synchrotron radiation on some beam lines (a) BL-16 and (b) BL-2.

3. BEAM INSTABILITIES

The beam instabilities observed during multi-bunch user runs were summarized in a previous issue (Activity Report #7 (1989) p.R-8).

The origin of the longitudinal impedance which drives the longitudinal coupled bunch instability has not yet been determined. The longitudinal instability causes an increase in the horizontal size of light coming from a non-zero dispersion region for a high stored current. An inquiry is now in progress to find out the structures (both rf cavity and vacuum chamber component).

Since positron accumulation started, a vertical instability which was not observed in electron accumulation has been one of the important problems.

For electron accumulation during multi-bunch operation, a two-stream instability due to ion trapping was only the vertical instability observed during user runs. It was sufficiently corrected by partial-filling operation and octupole magnets. However, a vertical instability observed during positron accumulation cannot be suppressed by exciting the octupole magnets. It causes an increase in the vertical beam size at stored currents higher than 150 mA. The vertical beam size at 350 mA is about 1.3 times as large as that at low stored currents.

The features of the instability are as follows:

1) coupled oscillation;
2) $I_{th} \approx 15$ mA without exciting the octupole magnets; and
3) broad distribution of the betatron side bands.

The threshold current of 15 mA is comparable to that of the strongest coupled bunch instability (vertical) due to the HOM(TM111V) of rf cavity. However, it seems difficult to attribute the instability to the HOM's of the rf cavity, since the cavity-induced coupled-bunch instability can be observed in both electron and positron accumulations. Moreover, the HOM's of the rf cavity causing such strong instabilities are narrow-band resonators. Therefore, if the instability is a coupled-bunch instability due to the impedance of the resonator, it should be attributed to low-Q ($\Delta f > 10$~20 MHz) and, therefore, to the large number of resonators around the ring. It should be pointed out that the mechanism of the instability, especially the reason why it appears only during positron accumulation, must be clarified, even if such resonators could be realized.

Much effort to investigate the cause of the instability and to avoid it is now being made (for example, see the report on development of RFQ in this issue). Up to now, the most effective way to avoid the instability is by operation with a small number of bunches. This was found to increase I_{th}, even at a low exciting current of the octupole magnets. At least, I_{th} becomes more than 230 mA under 26 equidistant bunch operation. However, high stored currents with a small number of bunches cause single-bunch effects such as local heating of the vacuum duct components, resulting in a shortening the beam lifetime.

M. Isawa

4. LOW-ENERGY OPERATION

Low-energy operation has been studied since November 1989, preparing for future FEL experiments. During test operation, the positron beam was injected at an energy of 2.5GeV in a single bunch; the beam energy was then lowered to a level less than 1 GeV.

An operating point of $(\nu_x,\nu_y)=(8.41,3.11)$ was used during the initial test operation; it was then changed to (8.43,3.36), relatively far from dangerous resonance lines. This new operating point was additionally expected to reduce the COD amplitude during deceleration; in fact, it resulted in a remarkable reduction of the beam loss during deceleration.

A horizontal beam blow-up due to a longitudinal coupled-bunch instability was observed during deceleration. In order to cure this instability, Robinson damping was applied: two cavities were used for beam acceleration; the other two were properly tuned to produce Robinson damping. As a result, the longitudinal instability was largely suppressed. The rf voltage was kept at 0.84MV during deceleration. This rather high rf voltage led to the obtainment of a short bunch length and a long Touschek lifetime.

By properly selecting the operating point and correcting the instability, a beam of up to 6.2 mA could be stored at an energy of 0.8GeV. The bunch length was measured with a streak camera at this beam energy. The measured average bunch length was 29psec at bunch currents of 3-1.5mA. This was 2.3 times as large as the natural bunch length. We estimated the peak current to be about 20A from the result. Other important beam parameters, horizontal and vertical emittances and energy spread etc., will be measured in future.

M. Katoh, N. Nakamura & S. Sakanaka

C. IMPROVEMENTS AND DEVELOPMENTS

1. INJECTION

1a. Single-Bunch Injection with a Horizontal Scraper

Single-bunch operation for user runs was undertaken three times in April, July and December, 1990. The accumulation speed was typically 0.08 mA/sec with a short-pulse positron beam having a peak current of 18 mA at a repetition rate of 25 Hz. Under this operation, the purity of the single bunches observed with a streak camera was few percent (typically 2-3 %). This population in the neighboring bunchs arose from an injected beam which was not captured by the rf field. The injected beam according to a phase-flow diagram is shown in Fig. 8. The pulse width of the injected short pulse beam from the linac was 2 nsec, which typically has 6 bunches in each pulse. The energy spread of the short pulse beam was about 0.5 %. The top and end parts of the beam are not captured by the rf bucket and drift on a flow curve. A spilled beam is thus captured by an adjacent rf bucket by either radiation dumping or excitation. To prevent this type of beam capturing, a horizontal beam scraper was installed in the straight section between bending magnets No.4 and 5. The spilled beam from the rf bucket oscillates around the captured beam. We can thus kill most part of the spilled beams by using a horizontal scraper. Figure 9 shows the results of injection both with and without a horizontal scraper, as observed with a streak camera. Injection with no scraper resulted in a beam population of 6.6 % in the next bunch (Fig. 9a). After the scraper was set at a position of +/-21mm apart from the center orbit,

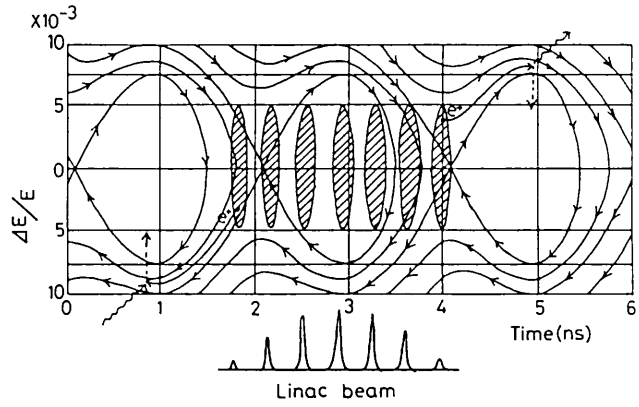

Fig. 8 Injected beam in phase flow diagram (simulation).

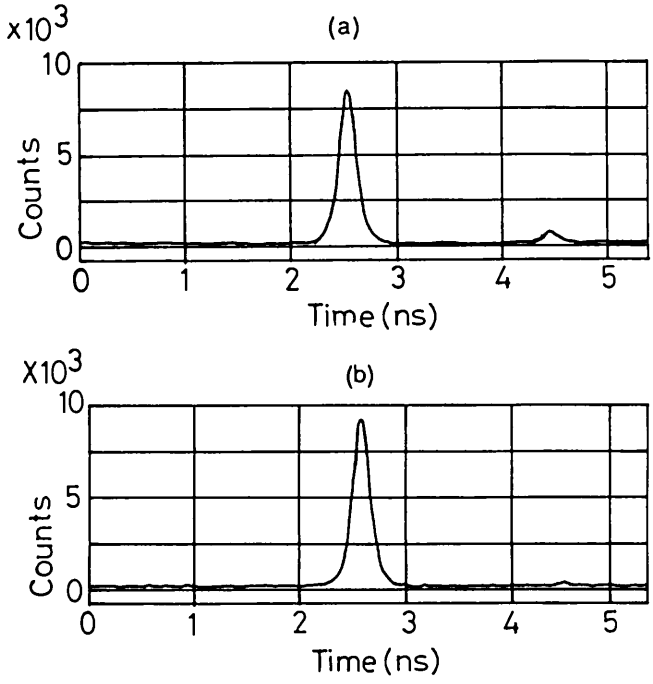

Fig. 9 Injection with and without the horizontal scraper. (a) beam population before inserting the scraper; (b) beam population after inserting the scraper.

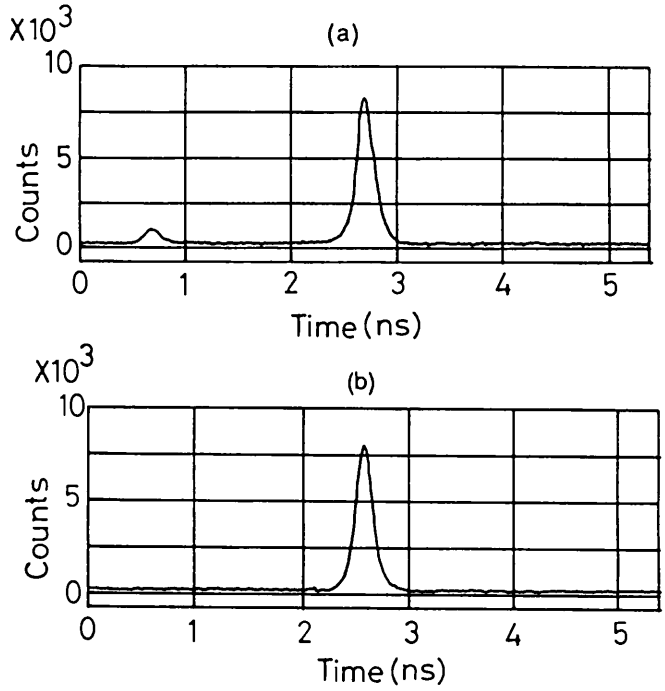

Fig. 10 Purification with RFKO and a vertical scraper: (a) Population before purification: (b) beam population after purification.

the population of the next bunch was reduced to 1.5 % (Fig. 9b). The accumulation speed at the injection with the scraper was reduced by half that without using it.

T. Mitsuhashi

1b. Purification of Single Bunch with RFKO and a Vertical Scraper

Shifts in the coherent betatron tunes with the stored current were observed;[1] these were those induced by a transverse broadband impedance. The measured tune shift was about -2×10^{-4}/mA. If the beam population of the neighboring bunches is small, a rather large tune difference exist between the center bunch and the adjacent bunches. We can therefor excite betatron oscillations of the neighboring bunches with an rf knock-out (RFKO) technique, and can kill the beam with a vertical scraper. A vertical scraper was installed at a position adjacent to the horizontal scraper. The results of this method are shown in Fig. 10. The beam population in the neighboring bunch was 8.6 % (Fig. 10a). After the scraper was set at a position of +/- 2.7mm away from the center orbit and betatron oscillation was exited by RFKO, the population of the neighboring bunch was reduced to a value less than 0.2 % (Fig. 10b). The beam in the center bunch was reduced by only 5 %.

T. Mitsuhashi

Reference

1) Photon Factory Activity Report #7 (1989) p.R-3. 1

2. RF

2a. Construction of an RF Quadrupole Magnet Used to Cure Transverse Coupled-Bunch Instabilities

A vertical beam-instability has been observed which enlarges the vertical beam size at high currents.[1] Some of its features suggested that this instability is a kind of coupled-bunch instability. One of the cures for transverse coupled-bunch instabilities is to produce a spread in the betatron frequencies of individual bunches in order to decouple coupled-bunch oscillations.[2-5] This is a promising method for the next-generation light sources which would have very small emittances and store high-current beams with multi-bunches. As an R&D effort to cure beam instabilities, and also aimed at suppressing the vertical instability, we have developed a new device called an RF Quadrupole Magnet (RFQM) in order to produce such a bunch-to-bunch tune spread.

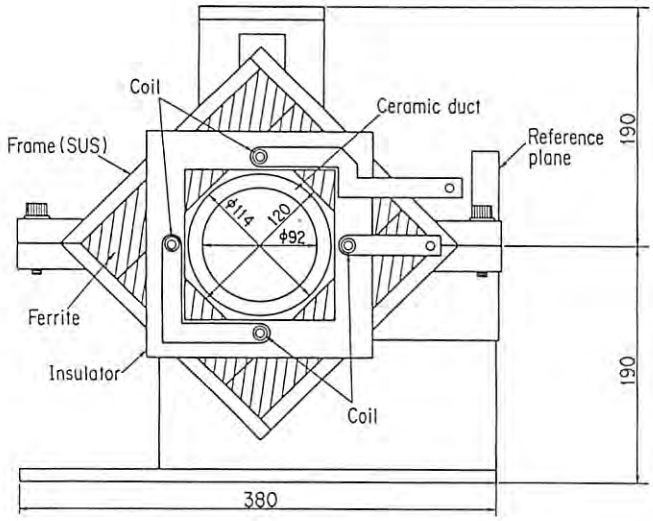

Fig. 11 Front view of the RF quadrupole magnet.

The RFQM can produce a field gradient oscillating at the revolution frequency of the ring (1.6 MHz). As shown in Fig. 11, this magnet has four conductors pipes which are connected so as to constitute a one-turn coil. Electric currents flow in the same direction on the left and right conductors and in the opposite direction on the top and bottom conductors. There is ferrite yoke outside the conductors to guide the magnetic flux. The magnet coil, together with external capacitors and resistors, constitutes a parallel-resonance circuit which is excited by an rf power amplifier. The peak field gradient is 0.017 T/m with a maximum peak current of 43.1 A. A beam duct inside the RFQM is made of ceramics coated with titanium of 1.4 μm thickness so as to allow wall-currents to flow smoothly. There are gaps on the coating to prevent it from heating-up due to eddy currents induced by the oscillating magnetic field. The principle parameters of the RFQM are given in Table 3.

We installed the RFQM in the PF ring October, 1990, as shown in Fig. 12. Several studies have been made so far. The tune shifts produced by the RFQM

Table 3. Specification of the RF quadrupole magnet

Maximum peak field gradient	0.017	T/m
Maximum peak current	43.1	A
Excitation frequency	1.6	MHz
Bore diameter	120	mm
Core length	0.34	m
Effective magnetic length	0.38	m
Self inductance	2.1	μH
Maximum horizontal tune spread (peak value)	1.3×10^{-3}	
Maximum vertical tune spread (peak value)	0.7×10^{-3}	

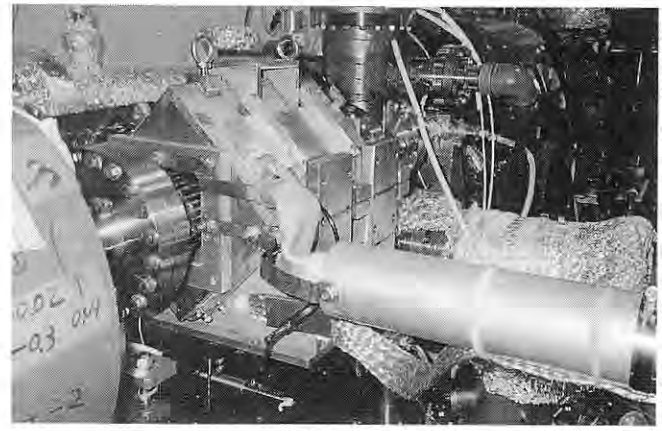

Fig. 12 Photograph of the RFQM installed in the RF ring.

were measured with a single-bunch beam by changing the phase of the RFQ field against bunch passages. Peak tune shifts of 1.3×10^{-3} and 0.7×10^{-3} were observed in the horizontal and vertical directions, respectively, with the maximum field. The threshold currents of a horizontal instability induced by TM-111-mode-resonance of the accelerating cavity and the vertical instability were observed to increase by a factor of about two by exciting the RFQM. More detailed studies are now in progress.

S. Sakanaka & T. Mitsuhashi

References

1) PHOTON FACTORY ACTIVITY REPORT #7 (1989) p.R-7.
2) R.D. Kohaupt, IEEE Trans. on Nucl. Sci., NS-22, No. 3 (1975) 1456.
3) G. Saxon, DL/SCI/P 204A.
4) Y. Kamiya, KEK 82-15.
5) Y.H. Chin and K. Yokoya, DESY 86-097.

3. VACUUM

3a. Beam Lifetime in Single-Bunch Operation

The beam lifetime in single-bunch user runs was much shorter than that in multi-bunch user runs. The product of the beam current and the beam lifetime, $I_b \cdot \tau$, deteriorated to about 1/80 during single-bunch operation, as shown in Fig. 13. Although a pressure rise was first conceivably responsible for this deterioration, a comparison of P_{av}/I_b in single- and multi-bunch operation showed that the pressure rise during single-bunch operation was only about 15 times as high as that during multi-bunch operation. We

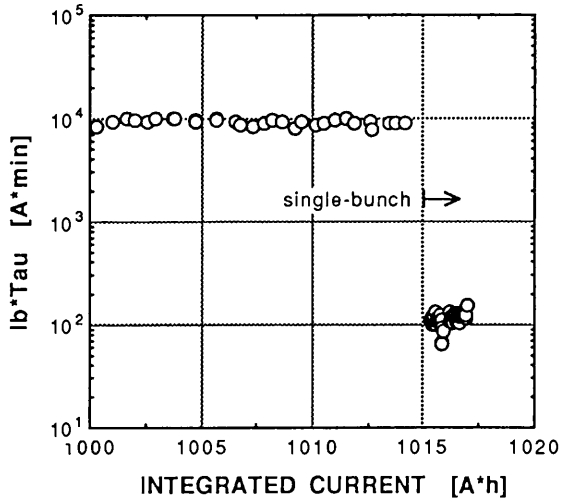

Fig. 13 Change of $I_b \cdot \tau$ as a function of the integrated current.

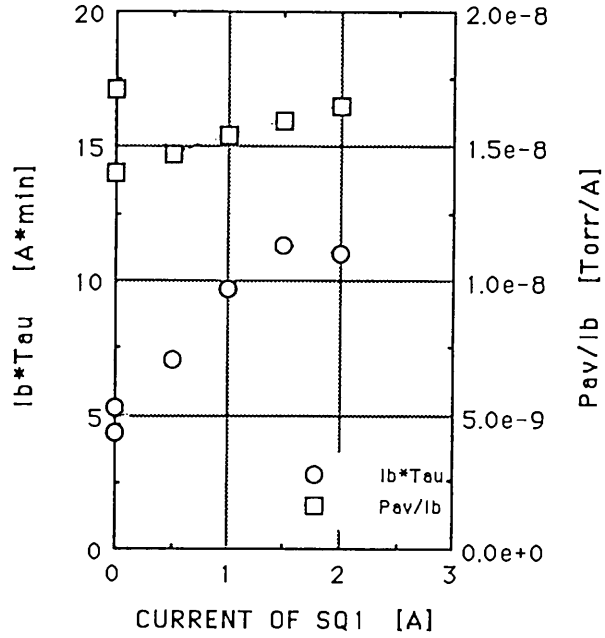

Fig. 15 Change of $I_b \cdot \tau$ by the skew quadrupole magnet field. The stored beam current is 40-34 mA. P_{av}/I_b is referred to in the figure.

therefore examined the partial pressure composition of residual gas. During single-bunch operation the hydrogen partial pressure gradually increased after beam injection. The composition ratio of hydrogen was thus higher during single-bunch operation than under multi-bunch operation, except at the beginning of a run. However, this only little affected the beam lifetime; the value of $I_b \cdot \tau$ was almost constant, and independent of the beam current during a run. We, thus, attributed the beam lifetime limitation to the Touschek effect since the Touschek lifetime is inversely proportional to the beam current. An estimate of the Touschek lifetime showed an $I_b \cdot \tau$ value of about

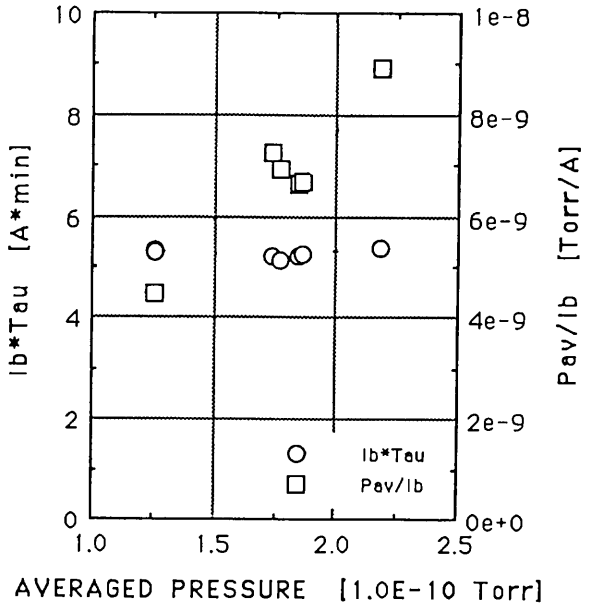

Fig. 14 Change of $I_b \cdot \tau$ due to a deterioration of P_{av}/I_b. The stored beam current was 28-24 mA.

28 A·min under single-bunch operation. This suggested that the beam lifetime is not severely limited by the pressure, but by the Touschek effect. We, thus, examined the dependence of the beam lifetime on the pressure and the beam size during single-bunch operation. The pressure could be changed by switching off the vacuum pumps, and the beam size by exciting a skew quadrupole magnet (SQ1). The results are shown in Figs. 14 and 15. The value of P_{av}/I_b increased by about 1.5 times upon switching off the DIP's, and by about 2 times upon switching off both the DIP's and SIP's; the beam lifetime, however, was not changed by the pressure rise (Fig.14). In contrast, an increase in the SQ1 field resulted in a longer beam lifetime (Fig. 15). These experiments led to the conclusion that the beam lifetime under single-bunch operation is limited by the Touschek effect.

Y. Hori

4. MAGNET

4a. Magnets with Full Aperture for Extracting Synchrotron Radiation

Magnets with apertures sufficiently wide to extract almost full synchrotron radiation from a bending magnet have been designed and installed downstream of bending magnet B22. These magnets are a quadrupole, a sextupole and a vertical steering magnet; their cross sections are shown in Fig.16. In the quadrupole

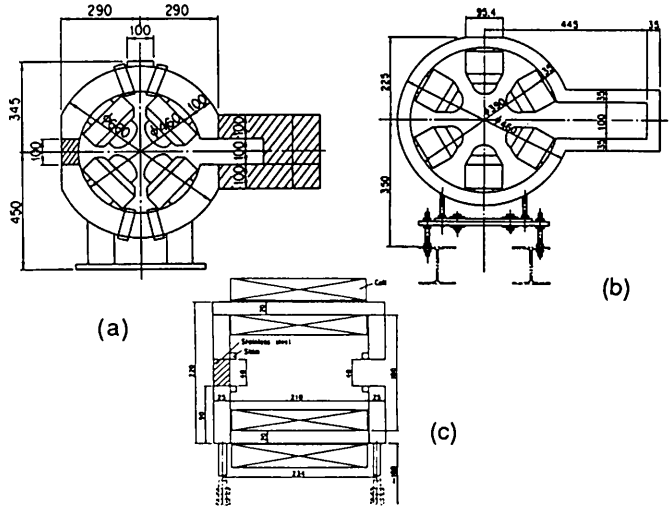

Fig. 16 Cross-section views of the magnets: (a) quadrupole, (b) sextupole and (c) vertical steering.

magnet, the iron yoke is split in the horizontal plane in order to provide a space which would allow synchrotron radiation to pass through it; the mechanical support is made of non-magnetic material (stainless steel). Since the field strength of the wide quadrupole magnet is slightly weaker than that of existing magnets when they are excited in series by the same power supply, a correction coil is implemented in order to compensate for any difference between them. Regarding the sextupole magnet, since the magnetic field is not much influenced by the deformed yoke, an iron yoke with a deformed shape has been adopted. In the vertical steering magnet, the iron yoke is also split, and one of the missing parts of yoke is replaced with stainless steel for the mechanical support, while the other is open to allow the vacuum chamber to pass synchrotron radiation.

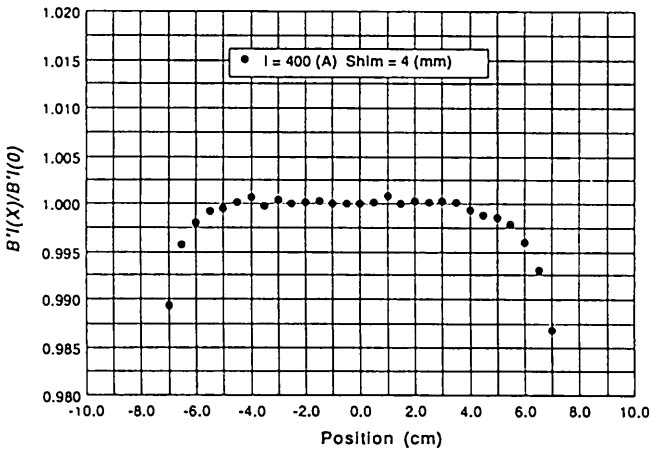

Fig. 17 Field gradient distribution ($B'I(x)/B'I(0)$) versus the horizontal position(x) of the wide quadrupole magnet. Data were taken at a current of 400 A with 4 mm-thick end shims.

Magnetic field measurements were carried out; results for the quadrupole magnet are shown in Fig. 17. A field region with a quality better than 5×10^{-4} is about ±4 cm. The Excitation curve is compared with that of the existing quadrupoles; the difference became apparent above 300 A. The correction coil current is set at 1.0 A for 2.5 GeV operation of the PF Ring. It has been verified that the fields of the sextupole and the vertical steering magnet are sufficiently good for operation.

We studied the effects of the wide quadrupole on the beam orbit (Fig. 18). Data were taken at three correction coil currents (1.0, 2.5 and -4.5 A). Both horizontal and vertical beta functions at 1.0 A agree well with the design value. On the other hand, horizontal beta functions are largely distorted in the case of 2.5 and -4.5 A.

Y. Kobayashi

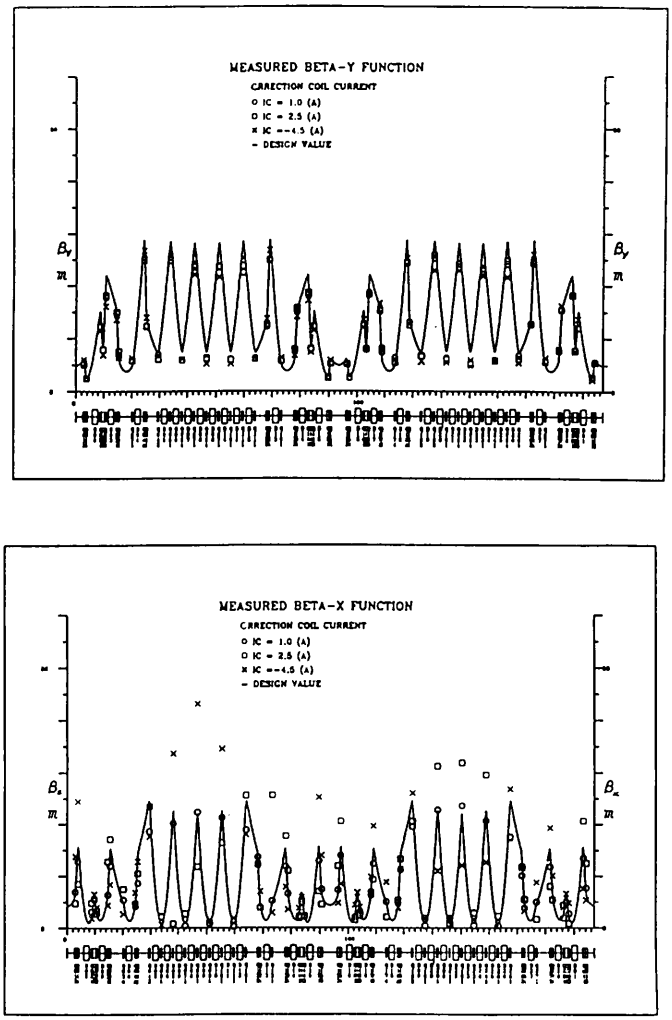

Fig. 18 Measured beta functions. Closed circles for a correction coil current of 1.0 A, open squares for 2.5 A, cross symbols for -4.5 A and a solid line for the design value.

5. INSERTION DEVICES

5a. Renovation of Undulator#2

The oldest undulator in the PF, U#2, was renovated during the term between January and April, 1990, and re-installed in the ring at the beginning of May. The present renovations are as follows: (a) use of a new magnet system (hybrid-type) having the same period length and the same pole number as the old one; (b) reinforcement of the mechanical frame; and (c) use of a new vacuum chamber with pumping ports. The capacity of U#2 has been largely enhanced by the present renovations.

The new magnet system

The specifications of the new U#2 are listed in Table 4 and compared with those of the old one. The fundamental parameters, λ_u=60mm (period length) and N=60 (period number), remain unchanged. The maximum value of the K-parameter has been increaced from 1.7 to 2.3 by adopting a hybrid-type magnetic structure comprising NdFeB magnets (NEOMAX35H manufactured by Sumitomo Special Metals Co. Ltd.; remanent field, B_r=12kG, coercivity, H_c=17kOe) and vanadium permendur poles instead of the pure type structure of $SmCo_5$ in the old system. This resulted in an extension of the radiation spectrum to lower energy regions; the first harmonic energy was lowered from 400 to 270eV.

Mechanical breakdowns of the magnet units frequently took place in the old system. These arose from poor adhesion between the magnets ($SmCo_5$) and their holders (Al) due to an aluminum-oxide surface layer. In each magnet unit of the new system, NdFeB blocks are glued onto a permendur core which is bolted to a stainless-steal holder. Since the stability and stiffness of this unit have been assured in other insertion devices (e.g. Revolver#19 and MPW#13), the magnetic field of the renovated U#2 will hereafter be stable. We have obtained data on the steering electromagnets for U#2 which minimized the C.O.D. variation with changes in its magnetic field. Thus, since this summer the gap change of U#2 has been freely allowed upon a use's request.

Table 4. Specifications of the new and old U#2.

	new system	old system
Period length, λ_u	60 mm	60 mm
Number of period, N	60	60
Maximum field	4.05 kG	3 kG
Maximum K	2.3	1.7
Magnetic structure	hybrid	pure
Minimum gap	27.6 mm	28 mm
Lowest 1-st harmonic	270 eV	400 eV
Maximum magnetic force	1200 kgf.	600 kgf.

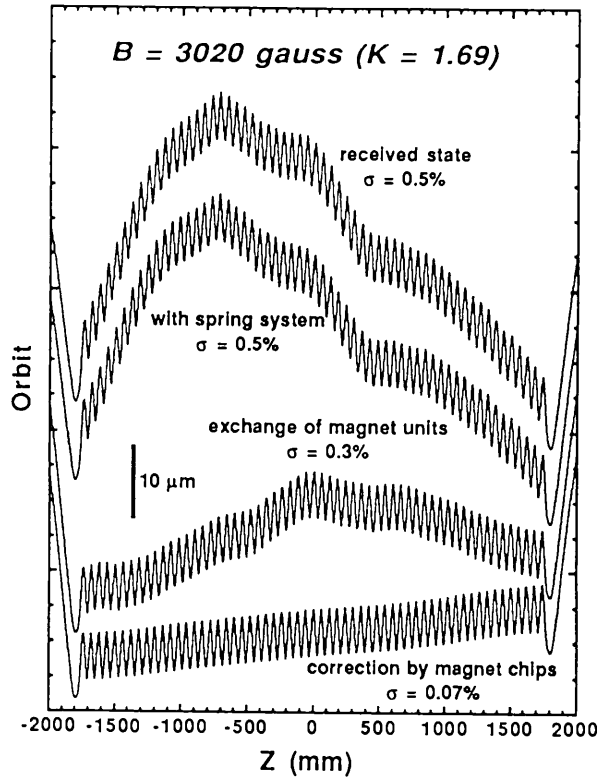

Fig. 19 Summary of field adjustments of U#2. The electron orbits along the undulator axis are shown at various stages of the adjustment. The undulator field was 3020G (K=1.69). A bold bar indicates 10μm. Evolution of the orbit corresponds to a decrease in the field error.

An adjustment of the magnetic field of the new magnet system was made so that deviations of the field integrals at individual poles, BL_{pole}, can be minimized. We tried to achieve an ideally sinusoidal electron orbit during this process. The adjustment was actually made by exchanging magnet units and by embedding 10-mm-diameter magnet chips (NEOMAX35) into 2 holes bored in the magnet holder. By using chips with a thickness ranging from 1 to 6mm, and reversing its magnetization direction, we could select the amount of additional BL_{pole} for the adjustment. Results of the field adjustment are summarized in Fig. 19 for case of K=1.69. The electron orbit has been greatly improved; the standard deviation, σ, of BL_{pole} has been decreased to σ=0.07%. According to an estimate by Kincaid[1] of degradation regarding the undulator radiation arising

from ramdom field errors, the effective brightness, B_{eff}, is given by the brightness without errors, B_o, and a function, G, as

$$B_{eff} = B_o \; G. \qquad (1)$$

Here,

$$G = \exp\left[-16n^2\sigma^2 N \left(\frac{K^2/2}{1+K^2/2}\right)^2\right], \qquad (2)$$

where n is a harmonic number. Although the effect of the field errors is significant for higher harmonics (eq.(2)), it is nearly negligible for σ=0.07%; $G \geq 0.99$ for $n \leq 7$. However, G was as small as 0.19 for n=7 in the old magnet system with σ=1%. The above estimate indicates that the present replacement will remarkably improve the brightness of the higher harmonics

Reinforcement of the mechanical frame

The new magnet system resulted in a remarkable increase in the magnetic attractive force (Table 4). The above-mentioned successful results were obtained at the cost of this problem. The maximum gap deformation amounts to 140μm at a maximum magnetic-force load of 1200kgf. This corresponds to a field error of 25G at 4kG, which is too large to ignore (25/4000=0.63%).

In order to overcome this problem, we devised a spring system which shared the load at supporting positions which are different from those of the existing ball screws (Fig. 20). This system comprises four spring boxes, each of which has a set of springs. The stiffer springs work at progressively closer gaps to support the load of a magnetic force which increases

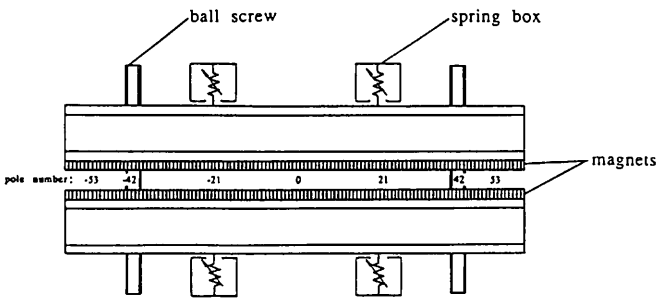

Fig. 20 Illustration of the spring system for the present U#2. Four additional spring boxes share the load of the magnetic force and compensate for any deformation of the magnet-mounting beams caused by an increase in the magnetic force.

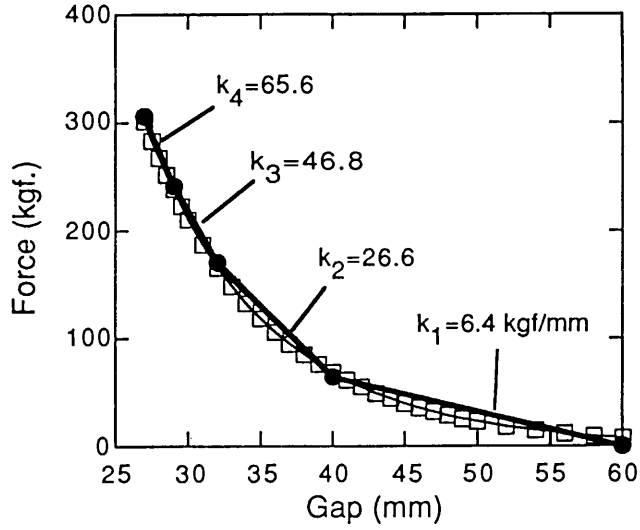

Fig. 21 Load-versus-stroke (or gap) relation of the present spring system. The squares indicate the calculated load to be shared by a single spring box at a minimum deformation of the magnet-mounting beams. The load can be supported by the spring system if it has effective spring constants (shown on the figure).

exponentially. The load shared by the single box was calculated for a minimum deformation of the magnet-mounting beam. The load-gap relation is shown by the squares in Fig. 21. Although the load shows an exponential dependence on the gap, it can be approximated by a force-gap relation of the spring system, which is shown by the bold lines in Fig. 21. The present system has four effective spring constants: k_1=6.4, k_2=26.6, k_3=46.8 and k_4=65.6kgf/mm. Using this system led to a reduction in the deformation of the magnet-mounting beam to 15μm (or 30μm as the gap deformation) at the minimum gap. This result indicates that the present system would also be very useful for a compact design of future undulators.

The new vacuum chamber

The new stainless-steal vacuum chamber has vertical and horizontal apertures of 24 and 110 mm, respectively. Both the top and bottom walls of the chamber have pockets which accept the pole tips when the gap is reduced towards the minimum value; the wall is 1 mm thick and the pocket is 2 mm deep. The chamber is evacuated with two sputter ion pumps (a total speed of 200 l/s) and eight Ti-getter pumps (a total speed of about 8000 l/s). The ultimate pressure of the chamber was about 4×10^{-11} Torr, and the pressure increase with the stored current was measured to be 1×10^{-10} Torr/100mA, in contrast with an estimated value of 1×10^{-8} Torr/100mA in the old chamber without a pumping system. Thus, the use of the

present chamber will lead to a two orders-of-magnitude decrease in the bremsstrahlung level.

S. Yamamoto

Reference

1) B.M. Kincaid, J. Opt. Soc. AM. B2,1294 (1985).

5b. 5-Pole Superconducting Vertical Wiggler

A new superconducting vertical wiggler was installed in the PF ring in Sep.1989 and has been operated for users since Oct.1989. The wiggler stopped its operation between Jan.1990 and Apr.1990 in order to repair a vacuum leak of its duct.

Although, the new wiggler has 5 magnet poles with a maximum field strength of 5 T, it has been operated at a field strength of 4 T using 3 magnet poles. Helium consumption was 0.25L/h without the beam and 0.9L/h with a beam current of 350mA in 3-pole, 4T operation. The wiggler vacuum duct is made of aluminum with a thickness of 7 mm. X-rays emitted by the wiggler hit the vacuum duct. The X-rays which impinge on the duct and pass through the duct wall reach the helium vessel. X-rays produced by a field of 4 T hit the duct with a total energy of about 1.2 kW at stored currents of 300 mA; 0.1% of the energy reached the helium vessel. Under 5-pole 5 T operation, the duct is hit with the energy of 5 kW. An estimate by Monte Calro simulation indicated that 3% of the energy reaches the helium vessel. Since the energy inflow into the helium vessel should be reduced to a value less than 1W, a wiggler duct with a radiation shield was designed and constructed in oder to reduce the amount of transmitted X-rays to a level less than 10^{-2} of the present one.

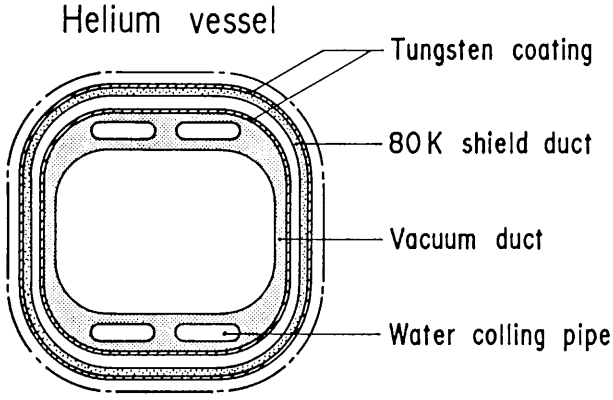

Fig. 22 Cross section view of the duct for 5-pole superconducting vertical wiggler.

The cross section of the duct is shown in Fig. 22. The duct has an aperture 42mm in width and 31 mm in height. The outer duct is cooled by 80-K refrigerators and set in an adiabatic vacuum between the ring vacuum and helium vessel. The inner one is cooled by water and is a boundary between the adiabatic vacuum and the ring vacuum. The aluminum duct was coated with tungsten with a total thickness of 1mm by a plasma spray. A simulation estimate showed that energy inflows into the helium vessel could be reduced to about 0.3 W under 5-pole, 5 T operation. The old duct was replaced with a new one in January, 1991.

H. Ohmi

6. MONITOR

6a. Bunch-Length Measurements Under Single-Bunch Operation

The bunch length under single-bunch operation was measured with a new streak camera system (C1587 temporal disperser with C2280 analyzer (Hamamatsu Photonics)), which has a maximum time resolution of 2psec.

Synchrotron radiation extracted at bending section B21 was used to measure the bunch length. The synchrotron light was reflected downwards using a water-cooled copper mirror mounted in a vacuum chamber, and then transported to a streak camera located on an optical table in the basement under the ring. A trigger system was constructed in order to synchronize with the synchrotron light. In this system, the 500MHz radio-frequency of the cavity was converted to a signal with the revolution frequency (1.6MHz) divided by N (N:integer, ≈1000). The signal was fed to a DG535 pulse generator (Stanford Research Systems), which produced trigger signals for the streak camera.

Bunch-length measurements were made for two values of the rf voltage: 1.1 and 1.7 MV. The results are shown in Fig. 23. For both cases, the bunch length increased with the bunch current and reached 1.6-times the natural bunch length at high currents, even though it was nearly equal to the natural bunch length at very low currents. This bunch-lengthening phenomenon suggests that the acceleration potential might be distorted by electromagnetic interaction between the beam and vacuum chambers with complicated structures. The obtained data will be analyzed in detail, together with data from additional measurements.

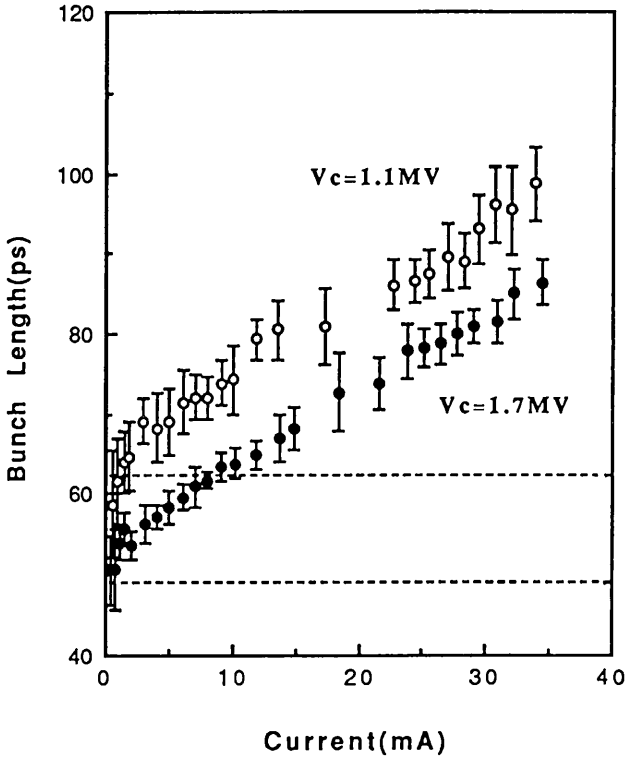

Fig. 23 Current dependence of the bunch length for two rf-voltage values, 1.1 and 1.7 MV (open and filled circles). The natural bunch length for each rf-voltage value is represented by a broken line. The error bars indicate the standard deviation of ten data.

In a previous issue of this report, measurements regarding the coherent betatron tune-shift in single-bunch operation were presented. However, it has turned out that the linearity of the DCCT system was bad at high bunch currents. Hence, the data obtained in a high-current region (>10mA) were unreliable. New measurements of the tune-shift will be carried out and then reported in the next issue of this report.

N. Nakamura

6b. New Method Concerning Vertical Orbit Feedback

A new orbit-feedback method, called the "variable pattern method", was devised in order to more effectively suppress vertical orbit movements than the old one. Operation of the digital feedback (DFB) system using the variable-pattern method started in November, 1989.

The variable-pattern method follows the following sequence:

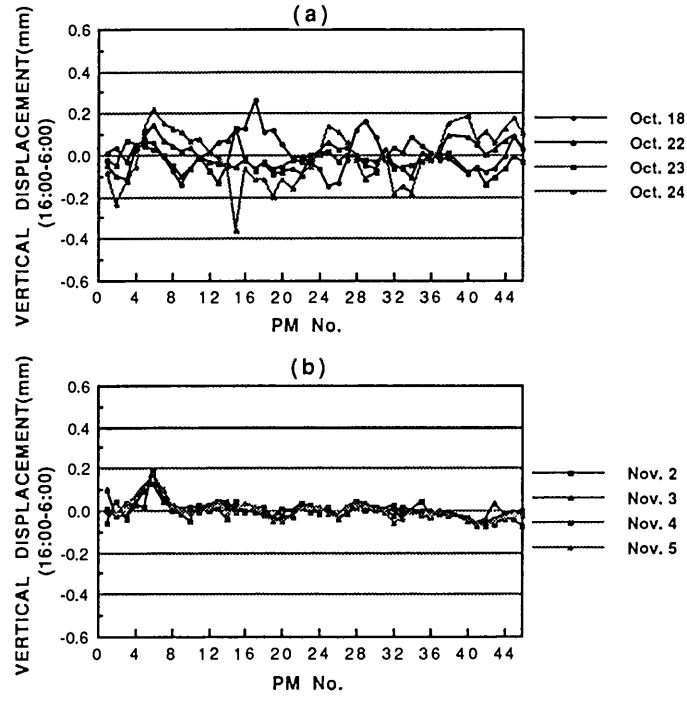

Fig. 24 Residual vertical orbit displacements in (a) old and (b) new methods: differences of orbits measured at 16:00 and 6:00.

(1) to set a reference orbit which is optimized for experiments on all beamlines;
(2) to measure the vertical orbit with the beam position monitors;
(3) to calculate the current pattern of the steering magnets for orbit corrections using the difference between the measured and the reference orbits; and
(4) to set the calculated current pattern.

Processes (2)-(4) are repeated with a period of 10-30 minutes by computer control. Process (4) is performed at hundreds of steps throughout the period in order to smooth the orbit correction. Since orbit correction patterns are updated, the variable pattern method can cope with any change in the orbit shape slower than the period.

The DFB performances in the old and new methods are shown in Figs. 24a-b. The residual orbit displacement was reduced using the variable pattern method by at least a factor of two. More frequent orbit measurements are required for making a finer correction. However, the amount of orbit movement during the measurement period is comparable to the positional resolution of the position monitor system. Further improvements of the position monitor system should make the DFB performance more effective.

N. Nakamura

6c. SR Beam Position Monitors for Insertion-Device Beamlines BL-NE-1 and BL-2

A newly constructed SR beam position monitor was installed in multipole wiggler beamline BL-NE-1. A schematic drawing of the monitor is shown in Fig. 25. The design of the monitor is based on the split-cathode photoemission chamber (SEC). The monitor comprises two pairs of right-triangle emitters at both horizontal edges of the SR beam. The emitters face the x-rays at an angle of a few degrees. With this arrangement of electrodes, we can observe any vertical fluctuations of the beam by means of SEC and horizontal fluctuations by a bleade-type monitor. The distance of the two emitters was set at 50 mm. The electrodes are made of water-cooled copper bleades, and no heat problem occurred at a ring current of up to 30 mA with the energy of 6.5 GeV. Since the SR beams from the fringing field of bending-magnets were almost cut by a Be-window, the ratio of the signal from wiggler light to that from bending-magnet light was heigher than 1000.

The observed fluctuations of the SR beam position are shown in Fig. 26. The SR beam drifted by 300 to 500 μm for about 30 min after acceleration from 2.5 to 5.8 or 6.5 GeV.

The same type of SR beam position monitor was installed in undulator beamline BL-2. Since this beamline has no Be-window, SR beams from the bending magnets directly hit the emitters. An optimization of the horizontal position of the emitters to undulator light resulted in a distance between the emitters of 8 mm. Under this condition, the ratio value of the signal from undulator light to that from bending-magnet light was about 500.

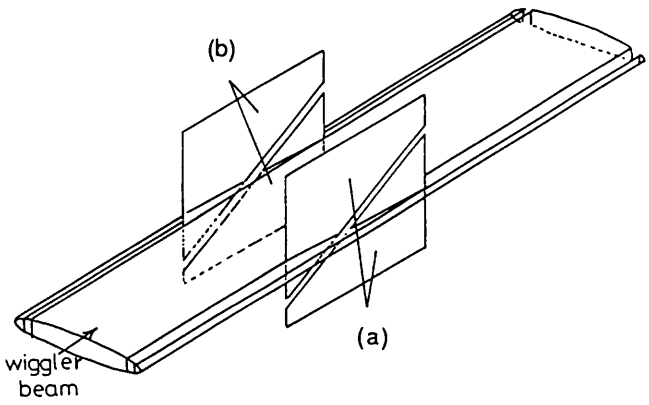

Fig. 25 Schematic drawing of the monitor. a) right side emitters; and b) left side emitters.

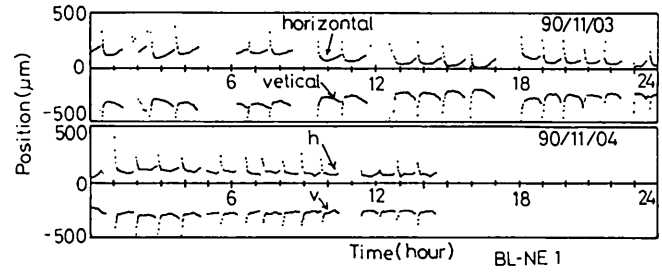

Fig. 26 Observed fluctuations of the SR beam position on AR BL- NE-1.

The observed fluctuations of the SR beam position are shown in Fig. 27. The SR beam often moved horizontally by 20 to 50 μm. This movement was coincident with the acceleration of the TRISTAN main ring.

T. Mitsuhashi

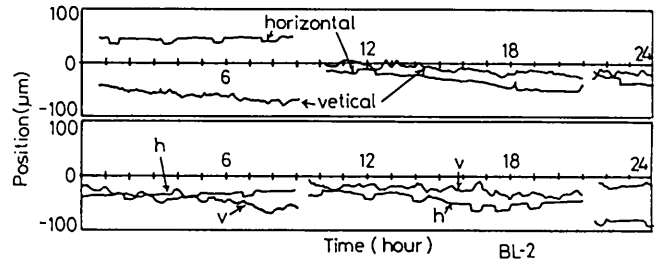

Fig. 27 Observed fluctuations of the SR beam position on BL-2.

6d. Measurements of Building Distortion

Beam position variations were observed to have a close correlation with the atmospheric temperature. The thermal distortion of the PF building could conceivably cause the building floor to be displaced and the beam position to move diurnally. A simulation model was made by Shimizu Corporation to analyze how the building was distorted due to thermal stress. The displacement of the storage-ring floor was measured by using a hydrostatic leveling system comprising twelve water tanks connected in series with pipes. The water tanks were evenly distributed along the storage ring and located under the quadrupole (Q)-magnets. Figure 28 shows a schematic of the hydrostatic leveling system. The Q-magnets are not shown here. Each tank is numbered by the name of the Q-magnet to which it belongs. The water level was measured using a laser displacement sensor mounted on the top cover of each tank.

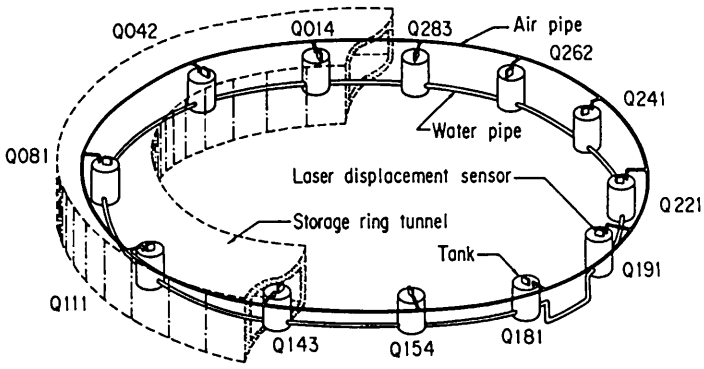

Fig. 28 Schematic of the hydrostatic leveling system.

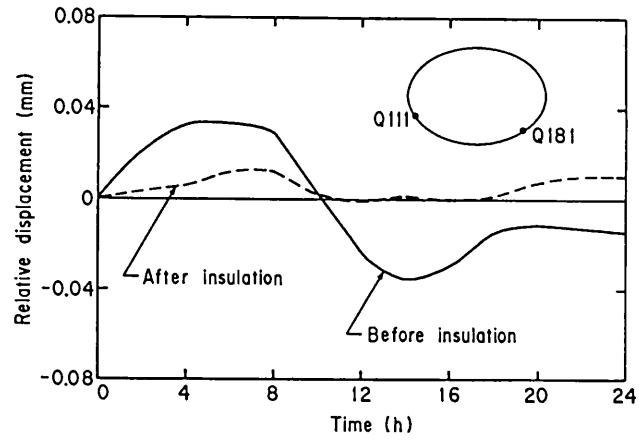

Fig. 29 Diurnal relative displacement of the Q111 tank (Q181 tank is its reference) both before and after insulation. An ellipse shows the locations of the Q111 tank and the Q181 tank in the storage-ring.

In order to reduce the distortion, the PF building was insulated with polyethylene-foam mats placed on the roof in January 1990. Figure 29 shows the typical relative displacements of the Q111 tank (Q181 tank is its reference) both before and after insulation. Table 5 shows the relative peak-to-peak displacements of all tanks one day before insulation, after insulation, and the ratio between the wo. Before insulation the displacements were 34μm~120μm. After insulation they were 14μm~36μm. The ratios of the displacementsafter insulation to that before were 1/5 ~ 1. The insulation was effective to reduce the distortion. The amount of the displacement after insulation was, however, of the same order as the resolution of present measuring system.

H. Nakamura

Table 5. Relative peak-to-peak displacements during one day for all tanks. A comparison of the displacement both before and after insulation.

	Q014	Q042	Q081	Q111	Q143	Q154	Q191	Q221	Q241	Q262	Q283
before insulation (A) (μm)	66	34	106	69	51	55	51	91	120	111	46
after insulation (B) (μm)	15	12	—	14	13	23	33	36	23	30	35
(B) ÷ (A)	1/4	1/3	—	1/5	1/4	1/2	1/2	1/3	1/5	1/4	1

7. CONTROL

7a. Upgrading of Computers

The control system uses four 32-bit minicomputers (FACOM S-3000 series from Fujitsu) as device controllers, and a general-purpose computer as a library computer. These computers are connected to each other through a token ring-type network[1]. We replaced three of four minicomputers from S-3300 to S-3500 on February, 1990; thus, all control computers are the S-3500, which has a computing power twice as large as that of the S-3300. No modification was required concerning the control program, since S-3500 is exactly compatible with S-3300. A general-purpose computer was also replaced (from FACOM M-360MP to FACOM M-780/10R); the new calculating speed is about 5-times faster as the old one. The other features of the control system, such as a network or device interfaces, remain the same.

C.O. Pak

Reference

1) C. O. Pak, Nucl. Instr. Meth. A277 (1989) 501.

7b. Control of Pulse Magnets for Injection

We realized the computer control of six pulse magnets for injection, which comprise four kicker magnets and two septum magnets.

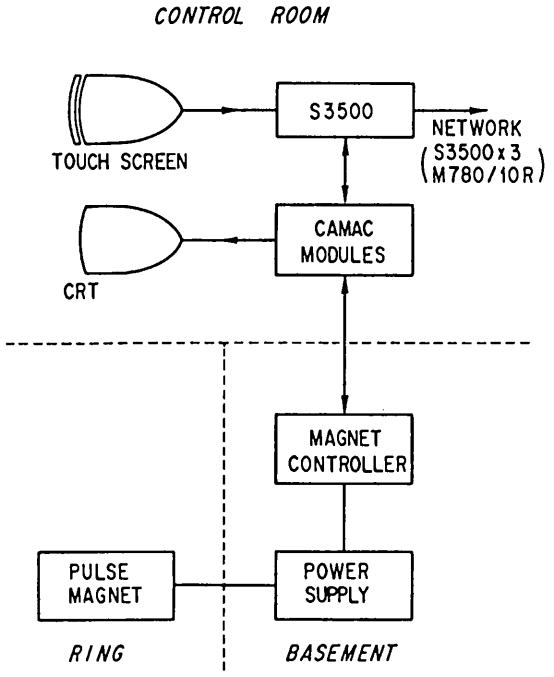

Fig. 30 Computer control system of the pulse magnets for injection.

A block diagram of the computer control system is shown in Fig. 30. The control computer is a 32-bit minicomputer (FACOM S-3500 from Fujitsu). Four control tasks coded by FORTRAN77 run under a real-time multitask operating system and are separately involved in the following functions:

- initializing interfaces and pulse magnet parameters,
- turning on/off power supplies of pulse magnets,
- changing the values of the pulse magnet parameters and saving these values into the disk, and
- monitoring the interlock status and parameters of the pulse magnets at regular intervals.

CAMAC is used for interfacing the control computer and the pulse magnet controller. The CAMAC input/output registers perform turning on/off the magnet power supplies and setting and monitoring magnet current. The CAMAC display control module (KINETIC 3232) generates a colored information screen regarding the interlock status and the parameter values of the pulse magnets.

Any touch screen of the operator console can provide an operation menu for the pulse magnets. By touching the screen, operators can easily change the deflection angle of each pulse magnet. Furthermore, they can directly set the injection beam position and angle or the height and angle of the kicker closed bump. Optimized values of these parameters for the accumulation rate can be saved into the disk and, if necessary, restored.

N. Nakamura

7c. Auto Correction of COD

We achieved an automatic correction of the COD (Closed Orbit Distortion) using a network of computers. So far, a correction of COD was carried out as follows. Workstation HP takes beam position data and sends them to a large mainframe computer (FACOM M-780/10R) through a routing minicomputer (FACOM S-3500). The currents which are to be applied to the correction magnets are the calculated interactively under TSS (Time Sharing System). These correction current data are sent to a control computer (FACOM S-3500) and applied to magnet power supplies. It was therefore necessary that a skilled person manually operated a complicated correction program at an intermediate step of any correction work.

Each step of the correction work was connected into one stream utilizing a network of different computers. The sequence of automatic correction is shown in Fig. 31. First, a task 'CODAUT' is started by a request from a touch screen. This task controls the flow of the COD correction sequence. 'CODAUT' sends a trigger to start a task, 'CODRUN', on other control computer. Then 'CODRUN' waits for the completion of the 'CODPRO' task, which receives beam position data from HP and sends them to M-780. When 'CODPRO' is successfully completed, data are avilable in a disk file of M-780, and 'CODPRO' send a signal to 'CODAUT'. Then, 'CODAUT' a request to start a correction program on M-780 which calculates

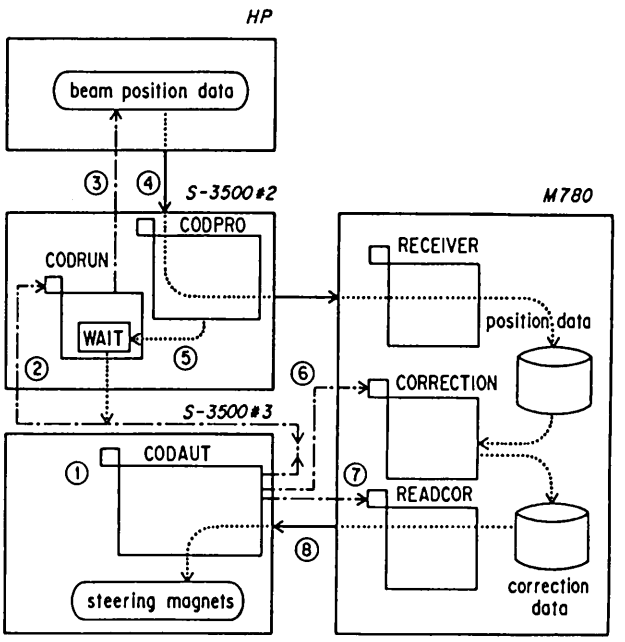

Fig. 31 Sequence of automatic correction of the COD.

correction currents and saves the results into a disk file. Finally, 'CODAUT' starts a program called 'READCOR' on M-780 which reads out the correction currents and sends them to 'CODAUT'. These correction current data are handed to a power supply control task.

In any case, one 'touch' does everything. Only one exception is the starting of data-taking program of HP, which is carried out by a hand. This will be refined by sending a start request from 'CODRUN' in the future. A refinement of a COD correction algorithm is also required, since a kind of 'pattern recognition' of the beam orbit form by a intermediate operator is lost during the automatic sequence.

C.O. Pak

8. BEAM CHANNEL

8a. Improvement of the Beamline Control System

A 53-pole wiggler on beam line BL-16[1] can produce synchrotron radiation with a high power density, two orders of magnitude higher than that obtained with a bending-magnet source. A fast-closing valve (FCV) was installed in this beam line in order to protect the storage ring vacuum against an instantaneous vacuum failure. The FCV can close a guillotine blade (made of 1.2-mm thick titanium-alloy) within ~11ms. Upon a vacuum failure, intense wiggler radiation impinges on the closing blade until a water-cooled heat absorber closes (~1 sec).

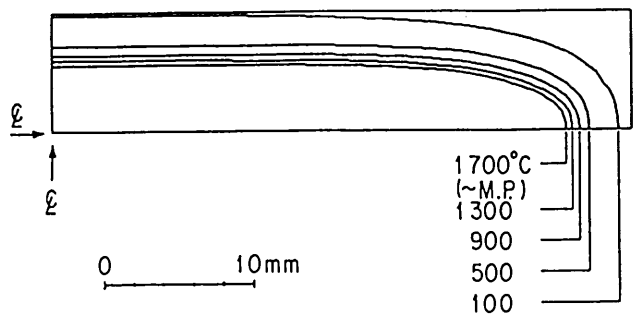

Fig. 32 Calculated temperature distribution across the FCV blade using a finite-element method for I=500mA. The model is symmetric about the center lines; one quarter of the blade area is shown. The exposure time is 1sec, equivalent to the closing time of the absorber.

The temperature distribution across the blade was calculated using a two-dimensional finite-element method in order to estimate both the melting time and melting area of the blade during exposure to intense wiggler radiation. Figure 32 shows the calculated temperature distribution across the blade at an exposure time of 1 sec (which is equal to the closing time of the absorber) for I = 500 mA. The melting area of the blade has a maximum width of 68 mm and a maximum height of 8.5 mm A transient thermal analysis was also made for the center of the blade as a function of time for various beam currents (Fig. 33). The temperature exceeds the melting point within 58ms at I = 500 mA. These results indicated a possible meltdown of the titanium-alloy blade within 0.1 sec at a maximum beam current of 500 mA, making the vacuum-protection function of the FCV ineffective.

In order to prevent the blade from melting, the FCV control system has been interlocked with RF klystrons so as to initiate blade closure after dumping the electron

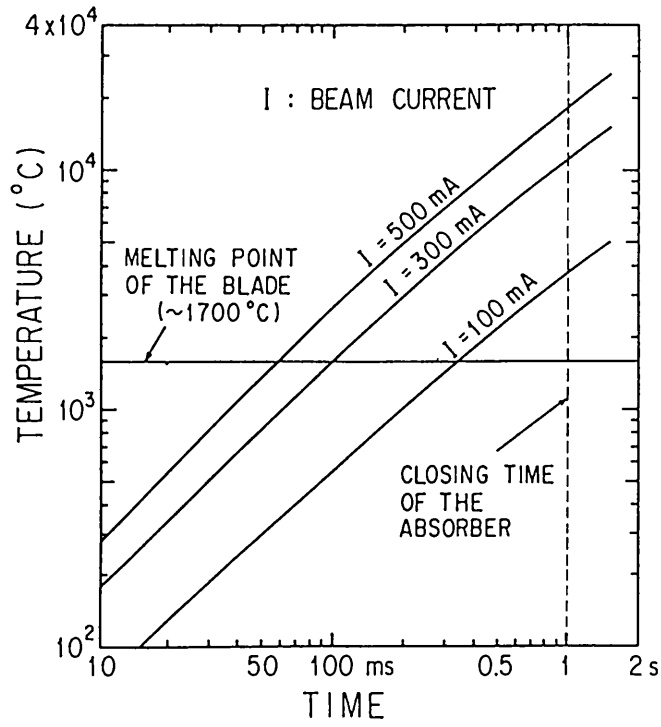

Fig. 33 Calculated transient temperature rise at the center of the FCV blade as a function of time for various beam currents. The temperature reaches the melting point before closure of the absorber for a range of operating beam currents between 100 and 500 mA.The temperature exceeds the melting point within 58ms at I = 500 mA, 100 ms at 300mA, and 340 ms at 100mA.

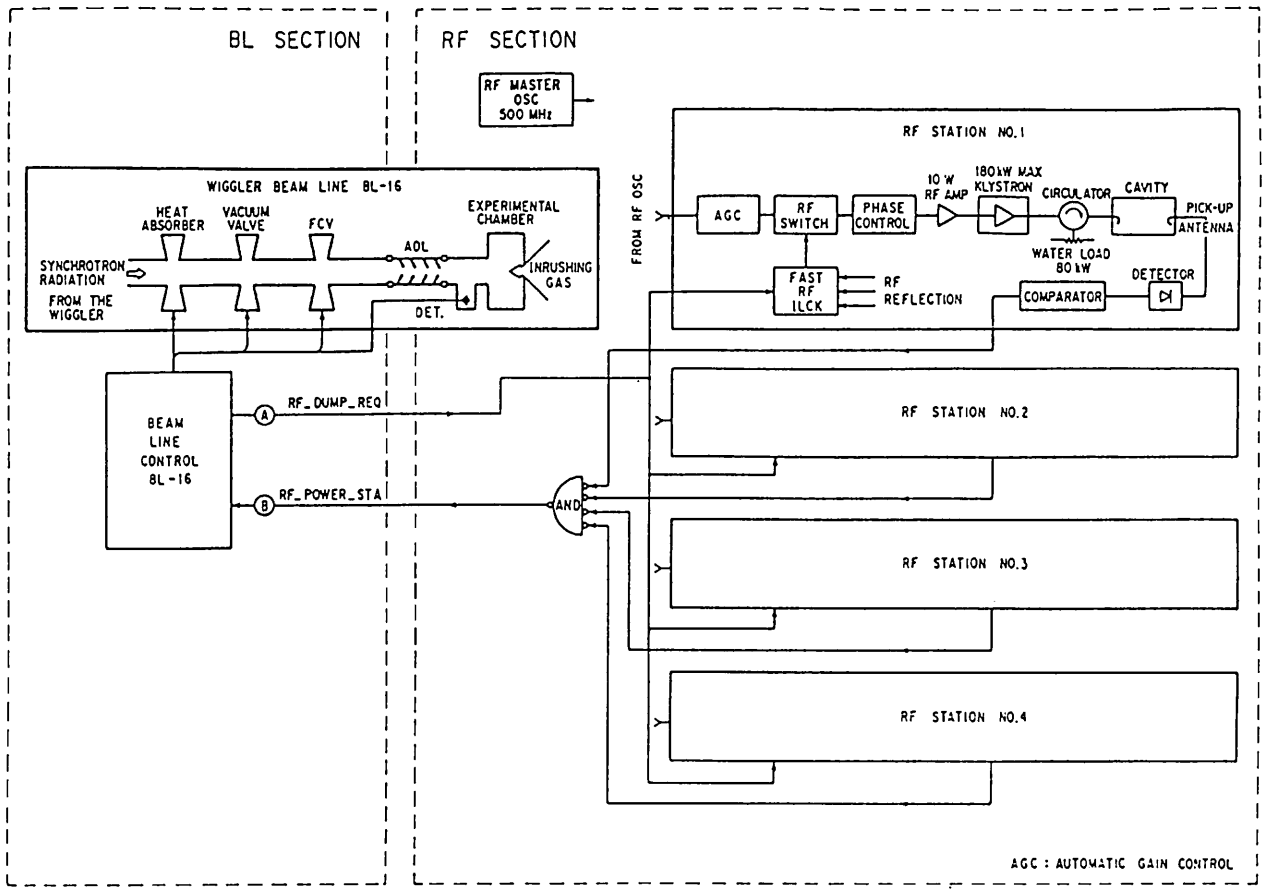

Fig. 34 Schematic diagram of the vacuum protection system for the 53-pole wiggler beam line BL-16.

beam by tuning off the RF power.[2] Figure 34 shows a schematic diagram of the vacuum protection system. There are four RF stations for beam acceleration, each of which consists of a klystron (500 MHz, 180kW max), a single-cell cavity, and low-level electronics (such as a low-level amplifier, automatic gain control and phase control). Each RF station has a fast-interlock circuit which can turn off the RF power within ~1 μs using an RF switch (PIN diode switch). The signal which requests the RF system to turn off the RF power is fed into this fast-interlock circuit.

The Beam Line Control System is a distributed computer-controlled system. Upon receiving an activated signal, it immediately initiates closure of the absorber and a backup vacuum valve. The FCV control system has the following additional three ports for two output signals and one input signal:

RF_DUMP_REQ	An output signal that Requests the RF system to turn off the RF power upon vacuum failure.
RF_POWER_STA	An input status signal of the RF power in all cavities.
CLOSE_BL	An output signal that requests the Beam Line Control System to close the absorber and the backup valve.

It should be emphasized that only when a vacuum failure is detected should the FCV control system dump the electron beam by activating the RF_DUMP_REQ signal. However, when the operating condition of the FCV is illegal the system should not dump the beam, but only close the beam line by activating CLOSE_BL in order to allow all of the other beam lines to continue operation.

A performance test for the system was made on wiggler beam line BL-16. A test pulse generator in the FCV control system can simulate an instantaneous vacuum failure of 5×10^{-4} Torr. The visible part of synchrotron radiation was observed with a photomultiplier. An electron beam of 300 mA was stored in the ring. A simulation pulse for a vacuum failure triggered the FCV control system. The FCV control system immediately sent the RF_DUMP_REQ signal to the RF sections; then, the RF power of the

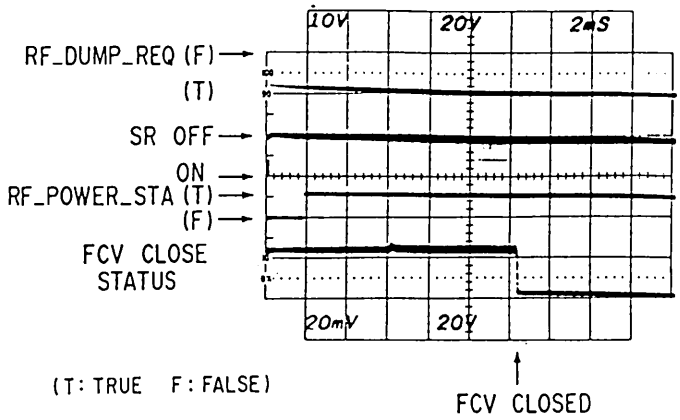

Fig. 35 Results of the performance test.
Four signal traces: 1) RF_DUMP_REQ, 2) synchrotron radiation, 3) RF_POWER_STA (logically inverted) and 4) close-status of the FCV. (Horizontal axis: 2 ms/div.)

klystrons was turned off and the blade of the FCV closed. This RF_DUMP_REQ signal also triggered an oscilloscope. Figure 35 shows four signal traces indicating: (1) RF_DUMP_REQ, (2) the synchrotron radiation signal from the photomultiplier, (3) RF_POWER_STA and (4) a FCV close-status. The RF_POWER_STA was activated within 1.8 ms, and the blade closed within 12.4 ms after being triggered. The time required for dumping the electron beam was also measured. A total execution time of 12.4 ms is acceptable since the wave-front of inrushing gas will propagate over a beam line length of 10m, (taking ~20 ms for an inrushing gas velocity of ~1000 m/sec (air), and for the delay time (~10 ms) due to the acoustic delay line). The system has been reliably operated for over a year without any trouble or misfiring.

N. Kanaya

References

1) T. Shioya, S. Yamamoto, S. Sasaki, M. Katoh, Y. Kamiya and H. Kitamura, Rev. Sci. Instrum., 60 (1989) 1859.
2) N. Kanaya, S. Sakanaka, S. Sato, T. Koide and S. Asaoka, IEEE Trans. Nucl. Sci., 37 (1990) 2.

D. LIGHT SOURCE SPECIFICATIONS

This section contains major specifications of the PF and AR rings to provide quick and handy information for users and machine physicists.

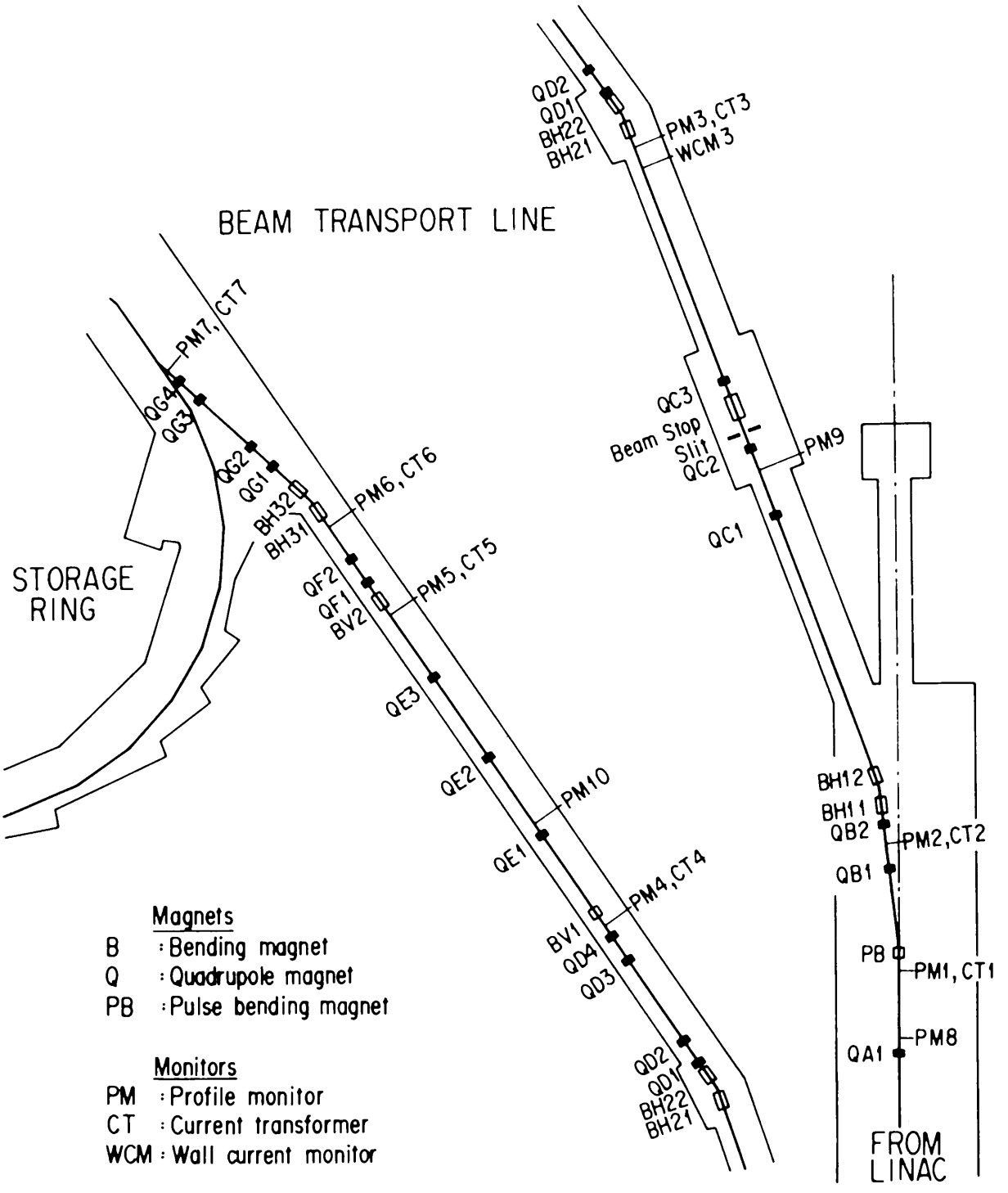

Fig. D-1. Beam transport line.

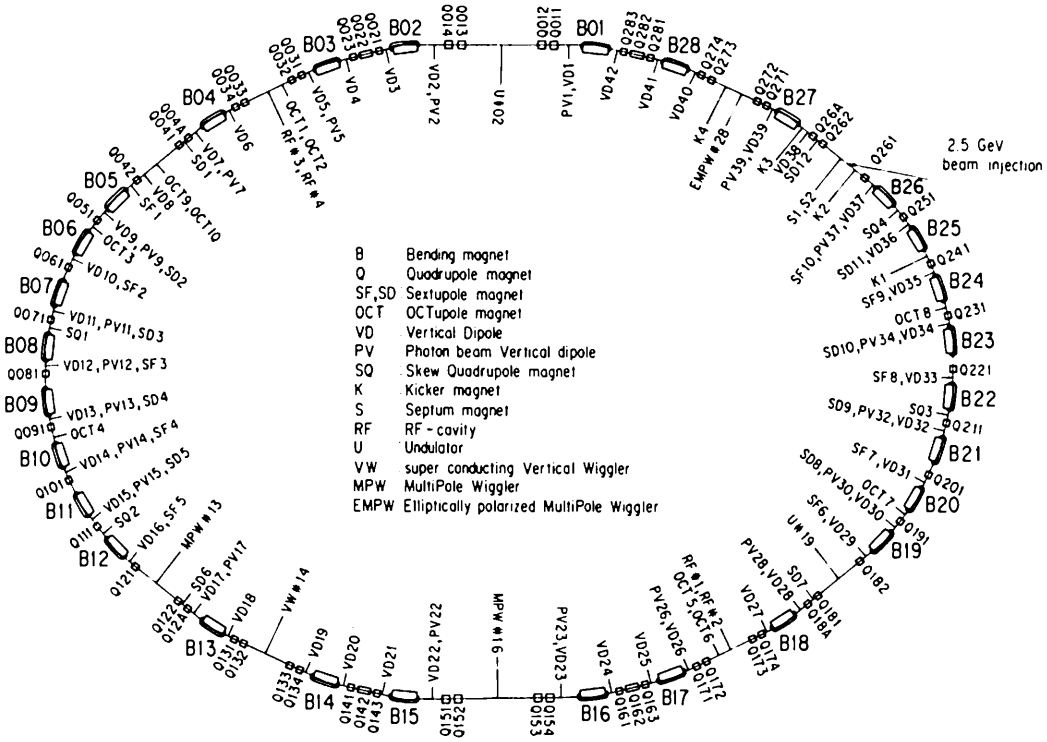

Fig. D-2. Ring lattice components.

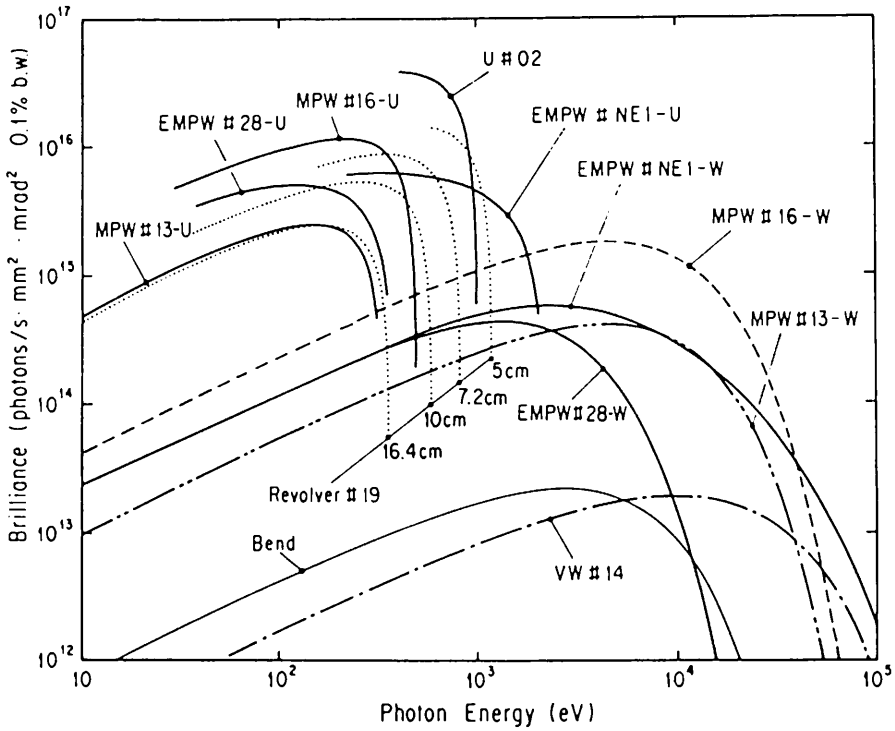

Fig. D-3. Synchrotron radiation spectra.
Brilliance of radiation vs. photon energy for the insertion devices (U#02, MPW#13, VW#14, MPW#16, Revolver#19 and EMPW#28) and the bending magnet (Bend) of the PF, and for the insertion device (EMPW#NE1) of the AR. The name of each source is assigned in Table D-4. Several insertion devices have both undulator and wiggler modes, which are denoted by U or W, respectively. The spectral curve of each undulator (or undulator mode of multipole wiggler) is a locus of the peak of the first harmonic within the allowable range of K-parameter. Spectra of Revolver#19 are shown for four kinds of period lengths.

Table D-4. Insertion devices.

Calculated spectral performances of the bend source and 7 insertion devices (one of them for TRISTAN Accumulation Ring) at the Photon Factory. E/I: beam energy and current, λ_u: period length, N: number of periods, L: length of undulator or wiggler, $G_v(G_x)$: minimum vertical (horizontal) gap height, $B_v(B_x)$: maximum vertical (horizontal) magnetic field, P: pure configuration, H: hybrid configuration, S.C.: superconducting magnet, $\sigma_{x,y}$: horizontal or vertical beam size, $\sigma_{x',y'}$: horizontal or vertical beam divergence, $K_h(K_v)$: horizontal(vertical) deflection parameter, $\varepsilon_1/\varepsilon_c$: photon energy of the first harmonic(critical energy in the case of bend source or wiggler), $\Delta\varepsilon/\varepsilon$: relative bandwidth, Pc: degree of circular polarization, $\mathcal{D}$: photon flux in unit solid angle (photons /s ·mrad^2 ·0.1%b.w.), $\mathcal{B}$: brilliance (photons /s ·mm^2 ·mrad^2 ·0.1%b.w.), P_T: total radiated power, $dP/d\Omega$: power in unit solid angle. Different operating modes of undulator and wiggler are denoted by -U and -W, respectively.

Name	E/I	λ_u	N	L	$G_v(G_x)$	$B_v(B_x)$	Type of	σ_x	σ_y	$\sigma_{x'}$	$\sigma_{y'}$	$K_h(K_v)$	$\varepsilon_1/\varepsilon_c$	$\Delta\varepsilon/\varepsilon$	$\mathcal{D}$	$\mathcal{B}$	P_T	$dP/d\Omega$
	GeV/mA	cm		m	cm	T	magnet	mm	mm	mrad	mrad		keV				kW	kW/mrad^2
Bend								0.74	0.26	0.38	0.037		4.0		3.5E13	2.9E13		0.058
U#02		6.0	60	3.6	2.8	0.4	H(NdFeB)	0.78	0.11	0.16	0.022	2.25	0.28	0.029	5.2E16	9.7E16	0.69	2.8
MPW#13-W		18.0	13	2.5	2.7	1.5	H(NdFeB)	1.66	0.17	0.15	0.019	25.0	6.2		9.7E14	4.9E14	6.7	2.6
-U												2.0	0.108	0.086	5.7E15	3.2E15	.036	0.16
VW#14	PF				5.0	5.0	S.C.	1.05	.096	0.16	0.025		20.8		2.2E13	3.4E13		0.18
MPW#16-W	2.5/300	12.0	26	3.1	1.9	1.5	H(NdFeB)	0.78	0.11	0.16	0.022	16.8	6.2		1.8E15	3.1E15	8.3	4.9
-U												2.0	0.162	0.050	1.6E16	2.8E16	0.12	0.52
Revolver		5.0	46	2.3	3.0	0.28	H(NdFeB)	1.66	0.17	0.15	0.019	1.3	0.637	0.021	4.1E16	2.3E16	0.21	1.27
#19		7.2	32			0.41	H(NdFeB)					2.7	0.176	0.039	2.1E16	1.2E16	0.44	1.54
		10.0	23			0.53	H(NdFeB)					5.0	0.0436	0.047	6.9E15	3.8E15	0.78	1.53
		16.4	14			0.62	P(NdFeB)					9.5	0.0078	0.066	1.2E15	6.3E14	1.05	1.09
EMPW#28		16.0	12	1.9	3(11)	1(0.2)	P(NdFeB)	1.05	.096	0.16	0.025							
-W												15(1)	4.2(Pc=89%)		2.5E14	3.4E14	2.3	0.38
-U												1(1)	.18(Pc=99%)	0.11	6.3E15	9.8E15	0.02	0.058
EMPW#NE1		16.0	21	3.4	3(11)	1(0.2)	P(NdFeB)	1.14	.079	0.14	0.021							
-W												15(1)	28(Pc=83%)		5.3E14	8.8E14	4.5	5.6
-U	AR											1(1)	1.2(Pc=97%)	0.12	5.4E15	9.5E15	0.04	0.49
U#NE3	6.5/50	4.0	90	3.6	1.0	0.83	P(NdFeB)	1.24	.121	0.26	0.018						3.3	35
												1.5	4.68	0.064	1.4E16	1.5E16	0.78	8.95

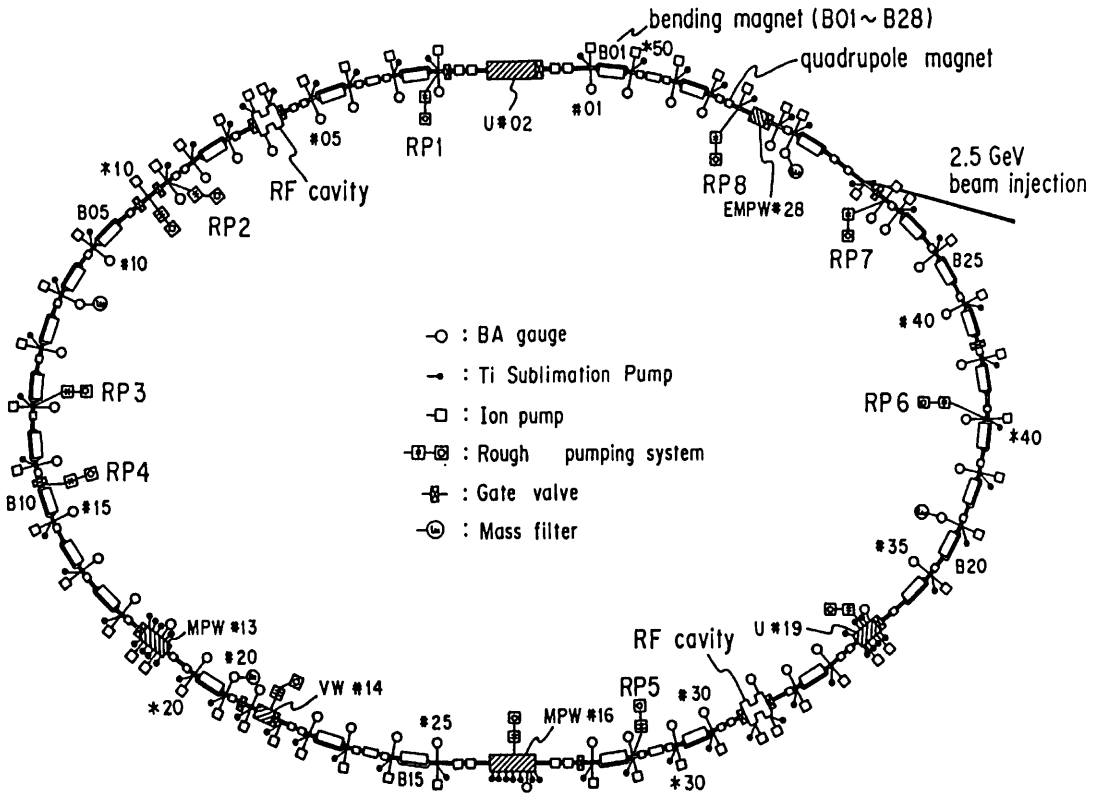

Fig. D-5. Vacuum system components.

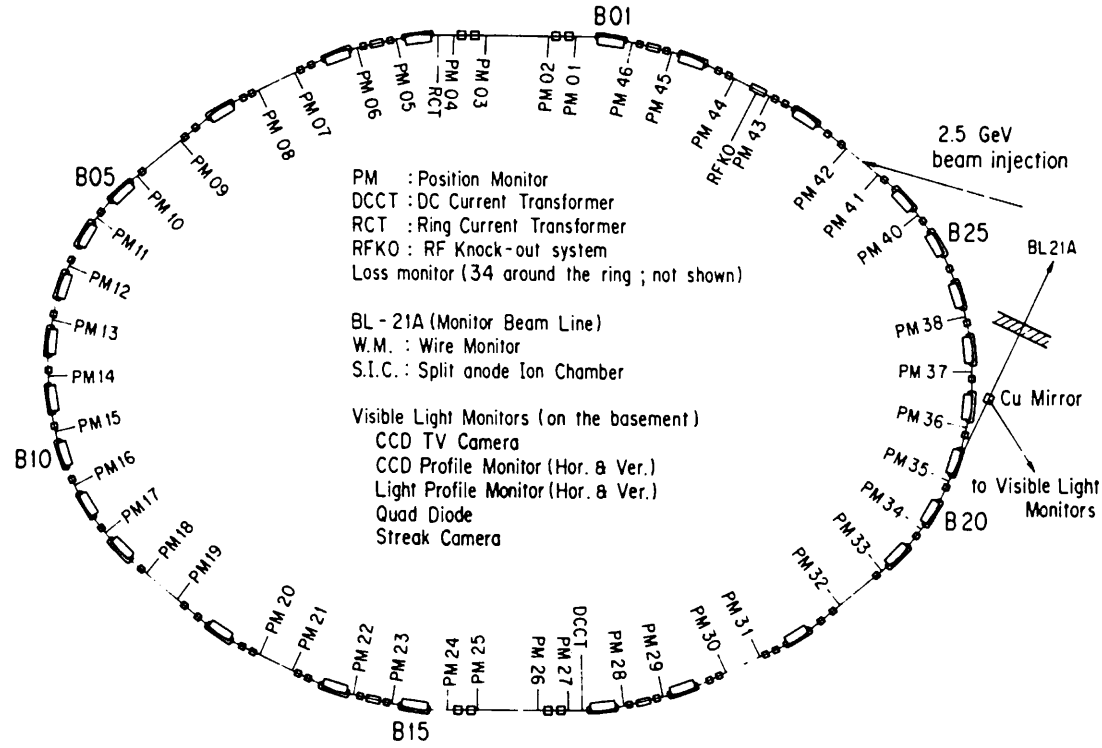

Fig. D-6. Beam monitors.

Table D-7. General parameters of the storage ring.

Energy	2.5 GeV	(1.6 GeV to 3 GeV)
Initial stored current	350 mA	(250 mA with vertical wiggler) (max. 500 mA)
Emittance	130nm·rad(horizontal) ~2nm·rad(vertical)	
Circumference	187m	(bending radius=8.66m)
RF frequency	500MHz	(harmonic number=312)
Injection	2.5GeV Linac	(positron/electron)
Beam lifetime	55 h (at 300 mA)	$I \cdot \tau \geq 16$ A·h (at ~250 mA ~ 350 mA)
Vacuum pressure	$\leq 3\times10^{-10}$ Torr (at 300mA) P/I ~ 8×10^{-10} Torr/A (at ~250 mA ~ 350 mA) ~ 3×10^{-11} Torr (at 0 mA)	
Insertion devices	Superconducting vertical wiggler 5T 60 period undulator K=1.78~0.1 26 period multipole wiggler/undulator 1.5T~0.04T Four way revolver type undulator 14 period multipole wiggler Elliptically polarized multipole wiggler	
SR channels	SR experiment 20 (5 under installation, 1 under design) Beam diagnosis 3	

Table D-8. Beam parameters.

Horizontal tune n_x	8.45
Vertical tune n_y	3.30
Compaction factor α	0.015
Natural chromaticity ξ_x	-15.8
ξ_y	-8.6
Bunch length σ_z	1.5cm
Transverse damping time	7.8msec
Longitudinal damping time	3.9msec
Energy spread	7.3×10^{-4}
Radiation loss	400keV

Table D-9. Principal parameters of the accelerator system.

Magnet system

	number of magnets	number of power supplies
Bending	28	1
Quadrupole	58	12
Sextupole	22	2
Octupole	11	10
Skew quadrupole	4	4
Dodecapole	6	6
Vertical steering	42	42
Photon beam steering	20	20
Others		
Backleg winding of bending magnet	28	
Electric shunt for tune compensation	12	

RF system

Number of RF stations	4
Number of klystrons	4 (180kW/klystron)
Number of RF cavities	4 (single cell cavity)
Shunt impedance	32MΩ (four cavities)
Unloaded Q	39000
Total power dissipated in cavity wall	89kW
Total cavity gap voltage	1.7MV
Synchrotron frequency	37kHz

Vacuum system

main pumping system

pump	pumping speed	number
SIP (Sputter Ion Pump)	128 l/sec	54
DIP (Distributed Ion Pump)	150 l/sec	26
Ti sublimation	----------	71
NEG (Non-Evaporable Getter)	----------	2

total effective pumping speed = 2×10^4 l/sec (for CO)

Rough pumping system

	pumping speed	number
TMP (Turbo Molecular Pump)	300 l/sec	12

Measurement

	number
B-A gauge	48
mass filter	4
cold cathode gauge	16 (for baking)

Sector gate valve

	number
all metal with RF shield	3
all metal without RF shield	3
Viton seal with RF shield	7
(wothout steps	3)

Injection system

Septum magnet

name	Septum I (S1)	Septum II (S2)
core material	laminated silicon steel (passive type)	
length [mm]	1500	1000
maximum current [A]	6000	6000
deflection angle [degree]	7.0	5.0
pulse width [msec]	88	60

Kicker magnet

name	K1 , K2 , K3 , K4
core material	ferrite (window frame type)
core length [mm]	300
maximum current [A]	3500
maximum deflection angle [mrad]	4.4
pulse width [msec]	5

Superconducting vertical wiggler

Maximum field strength on the beam orbit	5 Tesla
Magnet gap	66 mm
Magnet pole size (widthxhight)	40 mm × 260 mm
Number of magnetic poles	5 poles arranged every 200 mm
Rated exciting current	220 A at 5 Tesla
Superconducting wire	NbTi : Cu 1 : 1 size 1.70 × 0.85 mm^2
Cross section of coils	65 mm × 70 mm
Number of turn	2520
Liquid helium consumption in the permanent current mode	0.1 L/h
Damping rate of the permanent current	1.4×10^{-5}/h
Inductance	1.31 H/coil

Monitor system

PM(Position Monitor)	45
RCT(Ring Current Transformer)	1
DCCT(Direct Current Current Transformer)	1
RFKO(Radio Frequency Knock-Out system	1
LS(Loss monitor)	43
Visible Light Monitor	
CCD TV Camera	
CCD Profile Monitor (H&V)	1
Light Profile Monitor (H&V)	1
Quad Diode	1
BL-21A(Monitor Beam Line)	
W.M. (Wire Monitor)	1
S.I.C. (Split anode Ion Chamber)	1

Control system

		number	memory
Control computers	FACOM S-3500	4	16 Mbyte
Library computer	FACOM M-780/10R	1	32 Mbyte
Computer network (type : optical token ring) number of nodes = 5 (max. 256)			

Table D-10. Beam size and divergence at source point.

location	σ_x [mm]	σ_y [mm]	σ'_x [mrad]	σ'_y [mrad]
B15&B01	0.34	0.16	0.41	0.033
B02&B16	0.60	0.13	0.38	0.033
B03&B17	0.43	0.22	0.32	0.018
B04&B18	0.52	0.18	0.29	0.045
B05&B19	1.26	0.21	0.39	0.037
B06&B20	0.85	0.25	0.38	0.037
B07&B21	1.26	0.21	0.39	0.037
B08&B22	0.85	0.25	0.38	0.037
B09&B23	1.26	0.21	0.39	0.037
B10&B24	0.85	0.25	0.38	0.037
B11&B25	1.26	0.21	0.39	0.037
B12&B26	0.85	0.25	0.38	0.037
B13&B27	0.44	0.23	0.31	0.045
B14&B28	0.50	0.20	0.30	0.018

Table D-11. General parameters of the Accumulation Ring.

Energy		6.0 GeV (2.5 GeV to 8 GeV)
Initial stored current		20 mA (max. 50 mA)
Emittance		130 nm·rad (horizontal) ~ 2 nm·rad (vertical)
Circumference		377 m
Long straight sections		2 × (19.5 + 19.1) m
rf frequency		508.6 MHz
Bending radius		23.2 m
Number of bending magnets		72
Energy loss per turn		4.85 MeV
Damping times	τ_x	3.11 ms
	τ_y	3.11 ms
	τ_E	1.56 ms
Partition numbers	J_x	1.0
	J_E	2.0
Natural energy spread		1.06E-3
Momentum compaction factor		7.1E-3
Natural chromaticity	ξ_x	-22.2
	ξ_y	-12.8

Table D-12. Summary of Beamline in FY 1990.

Beamline	Affiliation	Source	Spectral range	Status
BL-1	NTT	bending magnet (B1)	VUV and soft X-ray	in operation
BL-2	KEK-PF	60-period permanent magnet undulator	soft-X-ray	in operation
BL-3	KEK-PF	bending magnet (B3)	VUV and soft X-ray	in operation
BL-4	KEK-PF	bending magnet (B2)	X-ray	in operation
BL-5	KEK-PF	permanent magnet wiggler/undulator (under design)	VUV and soft X-ray	under installation
BL-6	KEK-PF	bending magnet (B6)	X-ray	in operation
BL-7	University of Tokyo	bending magnet (B7)	VUV and X-ray	in operation
BL-8	Hitachi Ltd.	bending magnet (B8)	VUV and X-ray	in operation
BL-9	Nippon Electrical Co. (NEC)	bending magnet (B9)	VUV and X-ray	in operation
BL-10	KEK-PF	bending magnet (B10)	X-ray	in operation
BL-11	KEK-PF	bending magnet (B11)	VUV and soft X-ray	in operation
BL-12	KEK-PF	bending magnet (B12)	VUV	in operation
BL-13	The Institute of Physics and Chemical Research*)	27-pole wiggler	hard X-ray	in operation
BL-14	KEK-PF	superconducting vertical wiggler	hard X-ray	in operation
BL-15	KEK-PF	bending magnet (B15)	X-ray	in operation
BL-16	KEK-PF	53-pole permanent magnet wiggler/undulator	soft X-ray	in operation
BL-17	Fujitsu Ltd.	bending magnet (B17)	VUV and X-ray	in operation
BL-18	ISSP and KEK-PF	bending magnet (B18)	VUV and X-ray	in operation
BL-19	ISSP and KEK-PF	permanent magnet multi-undulator	VUV	in operation
BL-20	KEK-PF	bending magnet (B20)	VUV and X-ray	under construction
BL-21	KEK-PF	bending magnet (B21)	white, visible light and X-ray (branch line)	in operation
BL-27	KEK-PF	bending magnet (B27)	soft X-ray and X-ray	under construction
BL-28	KEK-PF	25-pole permanent magnet wiggler/undulator	circularly polarized VUV and soft X-ray	in operation
AR-NE-5	KEK-PF	bending magnet of Accumulation Ring (AR)	hard X-ray	in operation
AR-NE-1	KEK-PF	41-pole wiggler	circularly polarized hard X-ray and soft X-ray	in operation

*) Branch lines are constructed by following national institutes; National Research Laboratory of Metrology, National Institute of Researches in Inorganic Materials, Electrotechnical Laboratory, and National Chemical Laboratory for Industry

Instrumentation Division

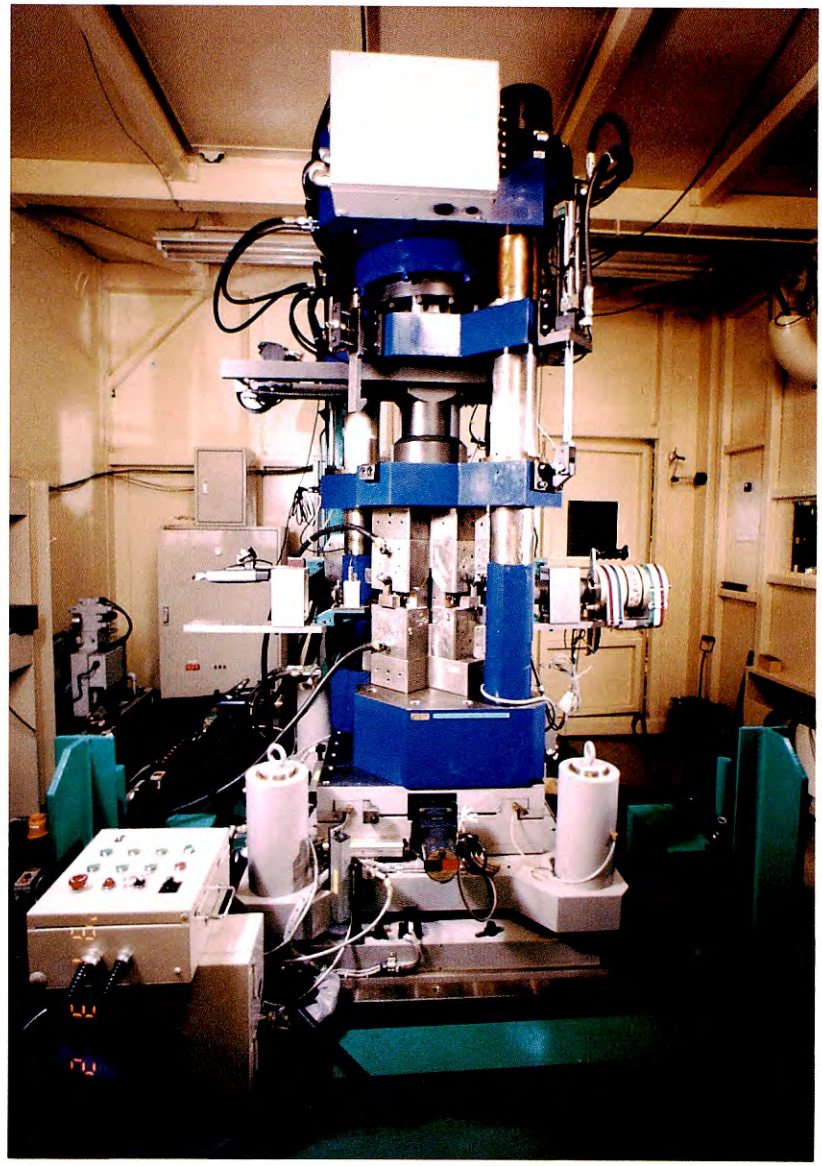

A new type of high pressure and high temperature apparatus with sintered diamond anvils, which is utilized at BL-13 and BL-14

CONTENTS

INSTRUMENTATION DIVISION

A. INTRODUCTION

During 1990, continuous efforts have been made both at the PF 2.5 GeV ring and the TRISTAN Accumulation 6-8 GeV ring to construct new beamlines to meet the increasing demands for utilizing synchrotron radiation. Construction work of BL-3 at the 2.5 GeV ring has been finished. BL-3 is used for VUV spectroscopy of free atoms and molecules (BL-3B) and X-ray diffraction of solid materials (BL-3A). BL-28 has also started its operation. It is the second beamline to provide circularly polarized radiation emitted from an undulator. The energy range of photons available is 5-300 eV. A pronounced magnetic circular dichroism was observed in a 3p-3d absorption spectrum of nickel thin films. BL-20 is now under construction. It consists of two branch lines; one will be devoted to VUV spectroscopy, and the other will be devoted to an Australia-Japan joint program on materials science and macromolecular crystallography.

At the TRISTAN Accumulation ring, a new undulator at NE3 initiated emission of brilliant radiation in December 1990. With advantage of the higher electron energy, it is designed to have the photon energy spectrum in the X-ray region. The brilliance of the most intense peak of the spectrum is higher by an order of magnitude than the maximum brilliance of X-radiation from the multipole-wiggler (53 poles) at the 2.5 GeV ring. It is expected to open a new field in the investigation of surface structure and nuclear resonant X-ray diffraction.

Utilization of the intense circularly polarized X-radiation from the multipole wiggler was made at NE1A at the TRISTAN Accumulation ring. Several new results were obtained in scattering and absorption measurements. Of these the most remarkable is the determination of the momentum distribution of "magnetic electrons" in ferromagnetic iron and nickel by Compton scattering from single-crystal samples. It has been shown that the distribution is in good agreement with the calculated one using a Full Potential Linearized Augumented Plane Wave Method which is based on the one-electron approximation. It is to be noted that the behavior of the magnetic electrons can be described by such a simple picture.

Determination of the atomic structure of biological materials is the most important step to the understanding of their properties. High brightness of synchrotron X-radiation has been shown to be indispensable to structure determination. At BL-6A of the 2.5 GeV ring, a large Weissenberg camera was designed which could carry a high-sensitivity X-ray area detector "Imaging Plate". It can record an array of a huge number of Bragg reflections from macromolecular crystals within ten minutes or so. It has been used by many users including those from China, Australia, the United States and the United Kingdom. An example of biological materials whose structure was analyzed recently is glutathione synthetase.

One of the most exciting opportunities that synchrotron radiation can offer is the ability to perform time-resolved experiments. The PF 2.5 GeV ring operates at a RF frequency of 500 MHz with a single bunch turn time of 624 ns and a bunch width of 100 ps. In 1990, single-bunch operations were tentatively performed in April, July and December.

An example of time-resolved experiments carried out with single-bunch operation is the observation of quantum beats in the nuclear Bragg scattering from an α-$^{57}Fe_2O_3$ crystal, using a new X-ray detector with a high time resolution (< 300 ps).

H. Iwasaki

B. BEAMLINES

B-1 NEW BEAMLINES IN OPERATION

BL-3A X-ray Diffraction/Scattering Beamline

BL-3A is used for diffraction and scattering experiments with synchrotron X-rays vertically and horizontally focused or highly collimated. This beamline can be used for both white and monochromatic X-rays. The optical system includes a collimating mirror (M1), a double-crystal monochromator, and a focusing mirror (M2). The layout of the beamline is shown in Fig. 1.

The performance of the optical elements was evaluated. At the first step the collimation experiment was carried out by bending the M1 mirror (1.5 m in length) in parabolic shape to reduce the vertical angular divergence. The total-reflection mirror of Pt-coated fused quartz (SiO_2) was used as a collimating element of grazing-incidence X-ray optics as well as a low-pass filter. The crystal arrangement of the (+,–,–) setting was applied to examine the degree of divergence. Si(111) crystals were used with a wavelength of 0.8 Å and an X-ray slit of 0.8 mm in vertical size was

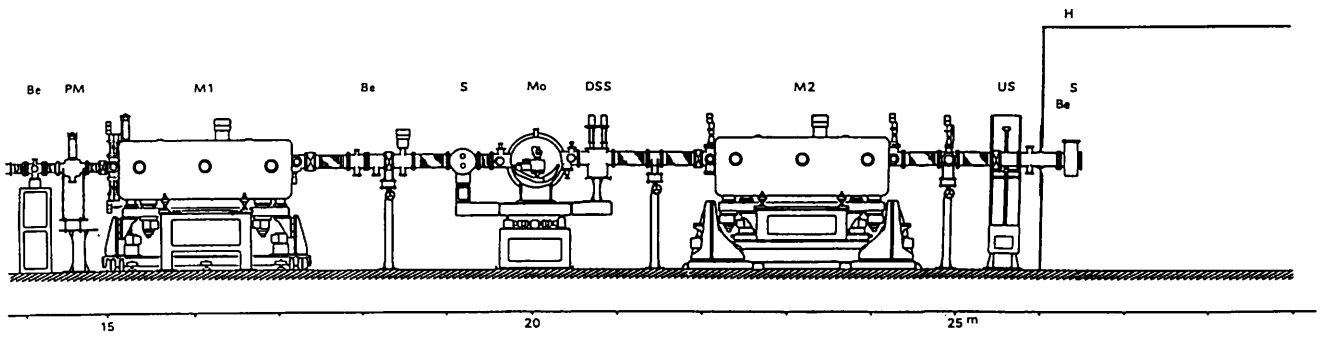

Fig. 1 Layout of BL-3A.

placed in front of the third Si(111). The grazing angle of the mirror was fixed at 3.4 mrad (25 keV). Angle-resolved scattering curves were measured as a function of the translation distance of the bending torques. Figure 2 shows the relationship between the full-width at half maximum (FWHM) and the amount of bending. The minimum with FWHM = 9.5" is significantly smaller than the value of 13.4" without the collimating mirror. The peak intensity has a maximum at the minimum FWHM.

Vertical focusing with the M2 mirror was made for the parallel beam through the M1 mirror. All parameters of the M1 mirror were fixed at the values for FWHM = 9.5". The grazing angle of the M2 mirror was also 3.4 mrad and the outgoing beam from the monochromator was focused at the position of the detector. All slits were fully opened. The incident beam was focused to 0.2 mm (about 1/50) without any slits (Fig. 3).

The second crystal of the monochromator is of a sagittal focus type. A triangular second Si(111) crystal, which can be bent, was designed for horizontal focusing. The size of the crystal currently used is 60 mm in base, 140 mm (max. 200 mm) in length, and 0.4 mm in thickness with 8 mm stiffening ribs on the back side. The bending can be adjusted by tilt and azimuthal rotations to obtain the best condition for the bending. The experiments with sagittal focusing were made at various X-ray wavelengths longer than 0.7 Å. An intensity gain of 20-40 was obtained at the focus position (27 m from the source) with a horizontal slit size of 1.5 mm. The horizontal beam size was reduced to about 1/60.

S. Sasaki

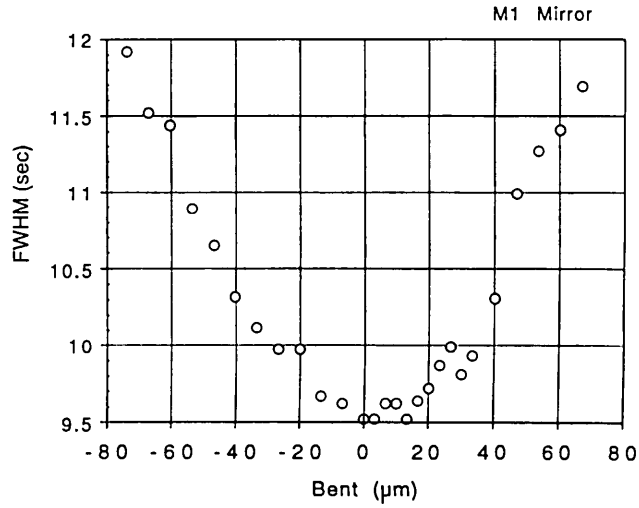

Fig. 2 Degree of beam collimation *versus* the translation distance of the bending torque. Each point shows the FWHM of the rocking curve of Si(111) in the (+,−,−) crystal arrangement.

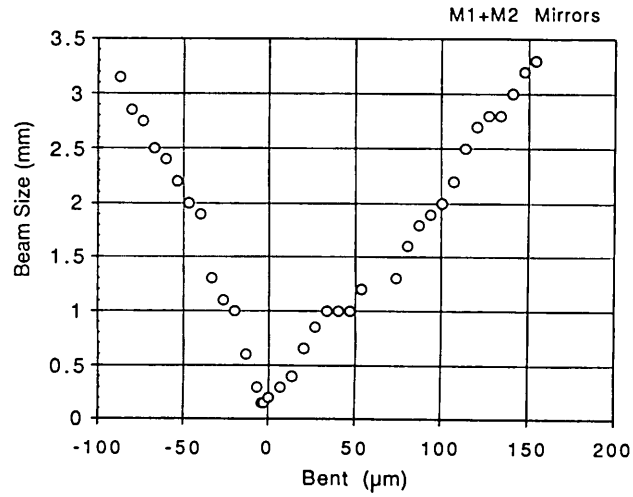

Fig. 3 Vertical focusing by the M1 and M2 mirrors. The vertical beam size is plotted as the function of the translation distance of the bending torque.

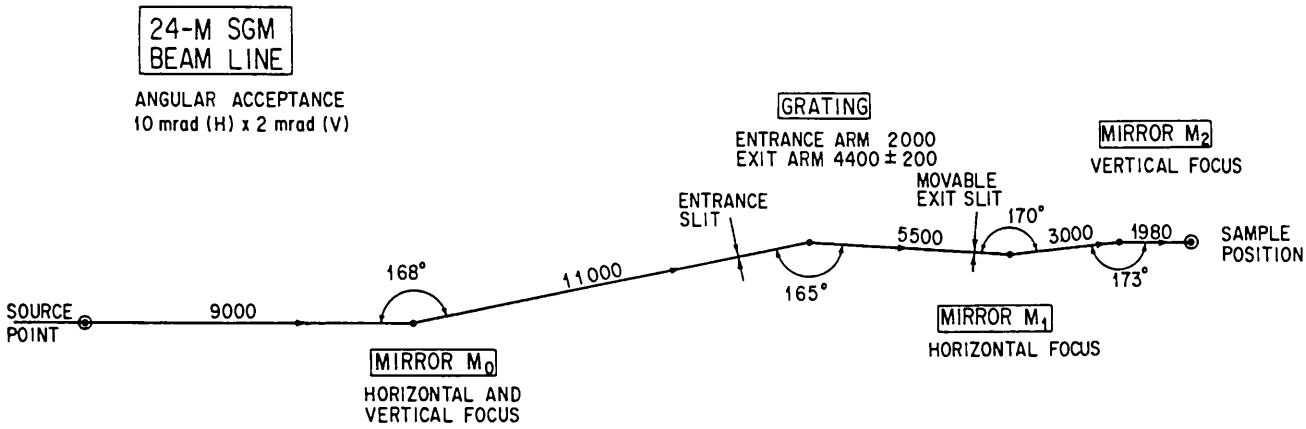

Fig. 4 Schematic layout of the 24 m SGM beamline.

BL-3B VUV Beamline

A 24 m spherical-grating monochromator (24 m SGM) has been constructed for operation in the VUV region at BL-3B. With two in-situ interchangeable gratings the 24 m SGM covers the spectral range 44 to 410 Å (280 to 30 eV). The beamline optical system consists of a 1:1 prefocusing toroidal mirror, a spherical grating monochromator with a movable exit slit, and refocusing mirrors (Fig. 4). Figure 5 shows the spectral flux through the 24 m SGM with 500 μm-500 μm slit widths at a current of 100 mA. The results of performance tests demonstrate that the 24 m SGM has high throughput and relatively high resolution. In the spectral region of 50-140 Å (250-90 eV), the resolving power of the monochromator is 1400-3400 with the 1800 l/mm grating and 100 μm slit widths.

After the performance tests, gas-phase experiments have been successfully done; (1) resonance Auger electron spectroscopy of rare-gas atoms and rare-earth atoms, and (2) photoelectron or Auger electron — photofragment coincidence spectroscopy of some molecules.

In the next fiscal year we will install a 200 l/mm grating to cover the longer wavelength region than 400 Å, because three gratings can be aligned outside the vacuum with respect to each other and to the rotational axis of a sine bar drive.

A. Yagishita

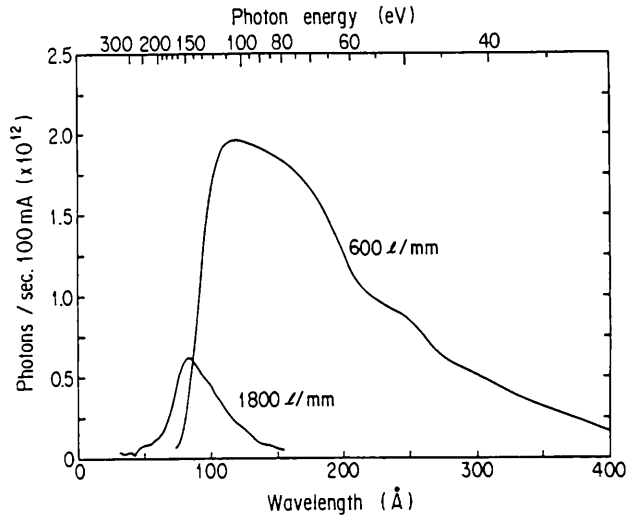

Fig. 5 Photon flux at the sample position for two gratings with entrance and exit slits 500 μm wide.

Table 1. Main parameters of the 24 m SGM beamline

Optical element	Distance from source (mm)	Radii R × ρ (mm)	Material	Coating	Reflective area (mm^2)	Grazing angle
Toroidal mirror M_0	9000	86100×941	CVD SiC/sintered SiC	Au	235×94	6°
Spherical grating G	20000	23800	fused quartz	Au	120×24	7.5°(0 order) 5.8-2.0° (+1 order)
Cylindrical mirror M_1	25500	∞×523	fused quartz	Au	100×100	5°
Spherical mirror M_2	28500	44039	fused quartz	Au	280×50	3.5°

AR-NE3 X-ray Undulator Beamline

AR-NE3 beamline at the Accumulation ring is ready to provide extremely intense X-rays from the 179-pole X-ray undulator. The spectra of the X-ray undulator were measured with a Si(111) double-crystal monochromator installed at the beamline. Figure 6 shows an example of the spectra with K = 1.47 (magnet gap = 19.6 mm). The 1st to 5th harmonics were observed with a NaI scintillation counter in the energy range from 5 to 25 keV. The spectra lower than 5 keV will be measured in the near future.

Effects of high-power radiation heat load on optical elements were observed. A water-cooled first carbon absorber (0.1 mm thick) installed upstream of the beryllium windows was observed to emit brilliant light like the filament of an electric light bulb when the AR operates at 6.5 GeV, 30 mA. The calculated radiation power is about 100 W/mm^2 on the carbon absorber when the gap of the X-ray undulator is 15 mm. The heat load on the directly water-cooled first silicon crystal of the double crystal monochromator was also observed by measuring rocking curves for different gaps (Fig. 7). The peak position of the rocking curves were found to shift to the lower angle when the gap was narrowed. A grazing angle of the SR beam to the first crystal was kept at 7.5 degree when the rocking curves were measured.

Several experimental devices have been installed at AR-NE3. They are the Precise X-ray Optics System and the 6-circle surface X-ray diffractometer. Mössbauer nuclear resonant scattering experiments are scheduled to be carried out from the spring of 1991.

X. Zhang

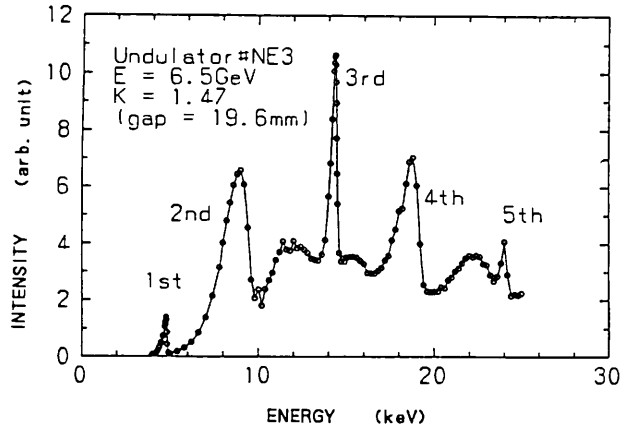

Fig. 6 Spectrum of the X-ray undulator NE3.

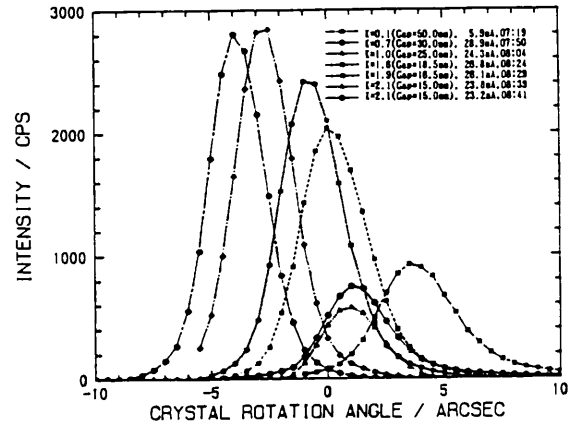

Fig. 7 Rocking curves of the second silicon(111) crystal for various heat loads on the directly water-cooled first silicon(111) crystal.

B-2 BEAMLINES UNDER CONSTRUCTION

BL-20A High Flux 3-M NIM Beamline

A high-flux 3 m normal incidence monochromator (3-m NIM) will be installed at BL-20A. As described in another chapter, the front-end section of BL-20 was completed during the summer shut-down of 1990. We expect a high photon flux in the energy range of 10 - 40 eV from the 3-m NIM, primarily because of a large horizontal acceptance angle of 28 mrad for the SR beam. Time-resolved experiments will mainly be carried out on this beamline, by observing photoelectrons, photoions , and fluorescent photons emitted from atoms and molecules, solid materials, and surfaces.

A schematic view of the optical system for BL-20A is shown in Fig. 8. A water-cooled SiC mirror, **M1**, is installed as close as possible to the source point, **P**, in order to have a large acceptance angle for the SR. The SR beam is focused onto the entrance slit, **S1**, of the 3-m NIM with mirror **M1** (of toroidal shape), with which one can have an ideal 1:1 focus with the condition PM1 ≅ M1S1. A plane SiC mirror, **M2**, between **M1** and **S1**, is installed in order to facilitate the optical adjustment. The 3-m NIM consists of **S1**, a grating, **G**, and the exit slit, **S2**. For wavelength scanning, **G** is rotated and translated on the bisector line of the angle S1GS2. When a 1200 grooves/mm grating is used in the 3-m NIM, the linear dispersion is 0.24 nm/mm. A post-focusing system is composed of plane and toroidal mirrors, **M3** and **M4**, which brings the SR to a focus at point **FP**. We expect a photon flux of 10^{10} - 10^{12} photons/A/sec and an ultimate resolving power of $>10^4$. The 3-m NIM will

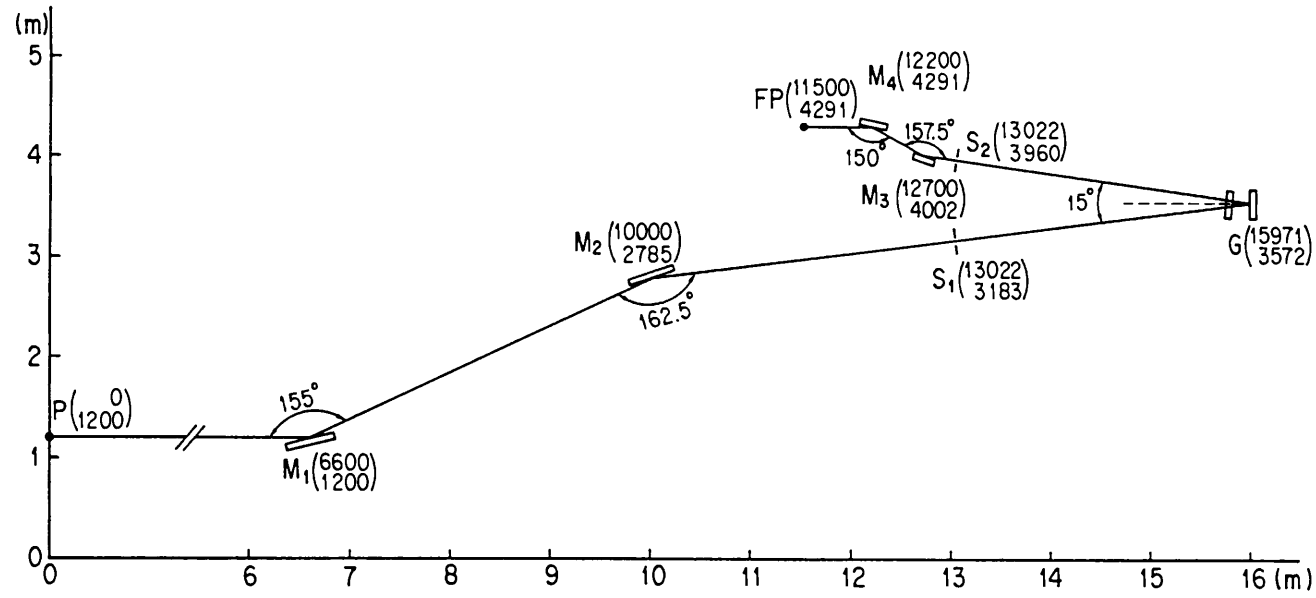

Fig. 8 Schematic view of the optical system of the 3-m NIM installed at BL-20A. **M1**:SiC toroidal mirror whose radii are 30949 mm and 1450 mm, **M2**:SiC plane mirror, **S1**:entrance slit, **G**:concave grating with a radius of 3m, **S2**:exit slit, **M3**:plane mirror, **M4**:toroidal mirror with radii of 3046 mm and 193 mm. Figures in parentheses show the positions of optical components in xy coordinates.

be constructed on the mezzanine floor, and an X-ray beamline, BL-20B, will be constructed by Australian scientists, in collaboration with the Photon Factory, beneath the mezzanine floor.

K. Ito

BL-27 Beamline for Radioactive Materials

BL-27 is under construction in the area where radioisotopes without sealing or wrapping can be handled. It has two branch beamlines, BL-27A for soft X-rays (1-6 keV) and BL-27B for hard X-rays (4-30 keV)(Fig. 9).

BL-27A adopts a focusing optical system which consists of a bent cylindrical mirror and an InSb(111) double-crystal monochromator. All the optical components are installed in ultra-high vacuum. The first crystal of the monochromator is cooled using a heat pipe. BL-27A has two tandem experimental stations. The upstream station is located at halfway of the focusing optics in order to get a large beam size (>20mm × 5 mm) for irradiation of biological samples. The downstream station is located at the focus point to be used for photoelectron spectroscopy. The estimated photon flux is 5×10^{10} cps for 3 keV X-rays at 200 mA with an energy resolution of 4×10^{-4}. BL-27B is designed for XAFS and diffuse X-ray scattering. Horizontal focusing is achieved by a Si(111) sagittally focusing double-crystal monochromator and vertical focusing is achieved by a downstream bent mirror. The flux of 10 keV X-rays is estimated to be 1×10^{11} cps at 200 mA with an energy resolution of 2×10^{-4}. Samples to be used in this area include biological

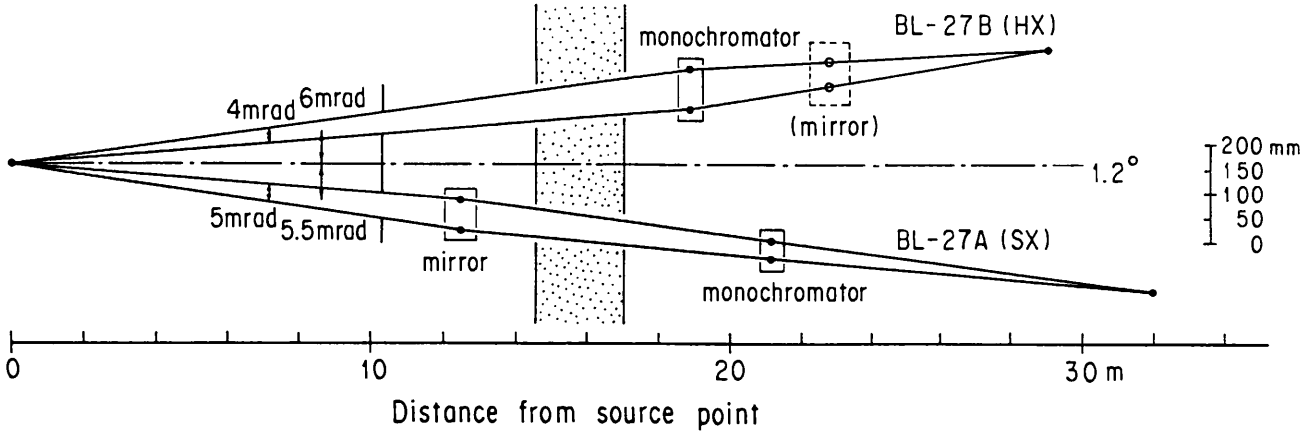

Fig. 9 Layout of BL-27A & B.

specimens which have incorporated radioisotopes as tracers, actinide(uranium and thorium) compounds and specimens bombarded with accelerated particles or with neutrons. Experiments using radioactive samples will start in 1992.

K. Kobayashi

AR-NE5 Beamline from Bending Magnet

BL-NE5 was newly designed and reconstructed in FY 1989-90 as a beamline to provide hard X-rays from a bending magnet of the TRISTAN Accumulation Ring (AR). The previous status of this beamline as a test port was already reported in the preceding volume.

The front end of the beamline was designed to meet the following requirements; (1) sufficient horizontal aperture of synchrotron radiation to achieve angiography (5A) and high pressure experiments (5C) and beam-position monitoring (5B) simultaneously, (2) protection of personnel from radiation hazards, and (3) to bridge the possible pressure difference between the vacuum of the storage ring ($<10^{-9}$ torr) and that of the experimental apparatus ($>10^{-7}$ torr). Due to the spatial restriction by an adjacent quadrupole magnet and a steering magnet of the ring, the maximum horizontal aperture of the beamline available is 34 mrad. The layout of beamline NE5 is shown schematically in Fig. 10. The front end inside the shielding wall consists of a water-cooled copper-block absorber, a water-cooled stationary beryllium filter as a heat absorber, double beryllium windows, several fixed masks, a pair of beam shutters one of which is water-cooled, and vacuum components. However, there is no acoustic delay line nor a fast closing valve which are normally installed in PF beamlines for protecting the storage ring vacuum against inrush of air. Except the copper-block absorber, all components that have moving parts are located in the lower vacuum section to avoid vacuum breakdown caused by possible mechanical trouble. For example, the beam shutters are installed behind the beryllium windows. Optical elements such as a monochromator or variable slits are placed in helium gas at the end part. These three branch beamlines (NE5A, B, C) are constructed with two vacuum lines (i.e. line-A and line-BC).

The beamline will be completed by the end of March of 1991 and it will be open to users.

T. Kikegawa

B-3 IMPROVEMENT OF BEAMLINES

BL-2A, 2B Undulator Beamlines

In the first half of this year, the 60-period soft X-ray undulator has been replaced by a new one with great efforts of the insertion device group of the light source division. One of the most useful benefits from this improvement is that the fundamental of the undulator radiation has been extended to the lower-energy region to cover the carbon K edge. Figures 11(a) and (b) show the typical spectra of undulator radiation measured by the 10 m grazing-incidence monochromator (BL-2B) and double-crystal monochromator (BL-2A), respectively.

Because highly-monochromatized soft X-ray sources are needed by core-level spectroscopists, we

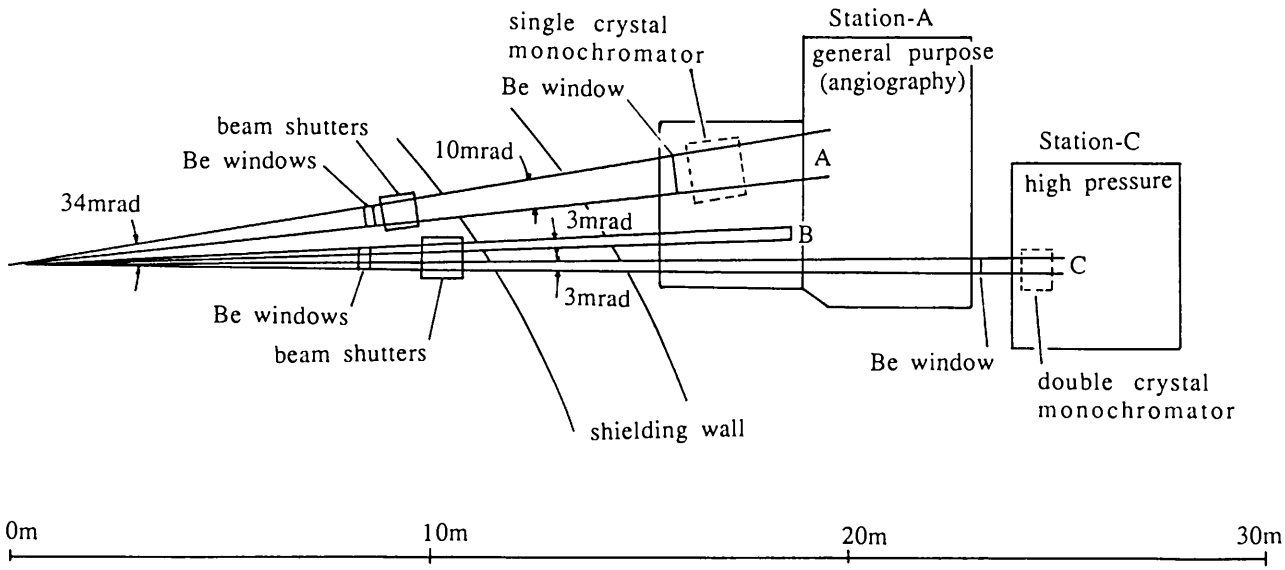

Fig. 10 Layout of AR-NE5 beamline

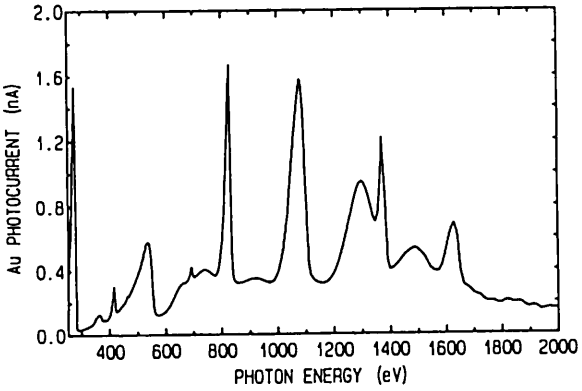

(a)

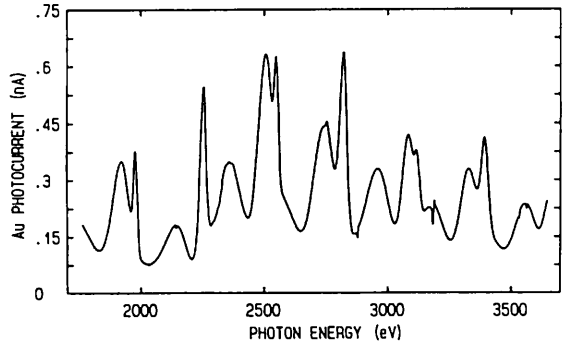

(b)

Fig. 11 (a) Undulator radiation spectrum measured with the 10 m grazing-incidence monochromator and (b) higher-energy part of the spectrum measured with the InSb double-crystal monochromator.

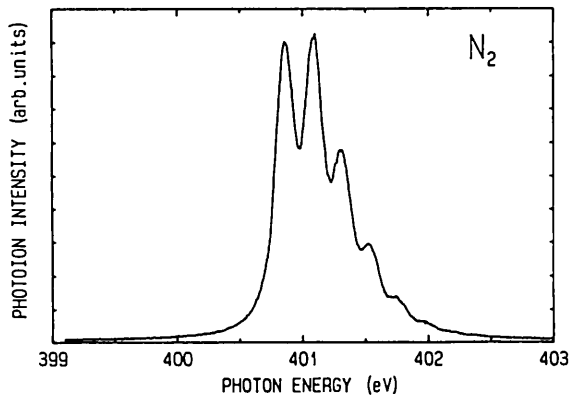

Fig. 12 High-resolution photoionization spectrum of N_2 $1s \rightarrow \pi^*$ excitation.

have tried to operate the 10 m grazing-incidence monochromator in high-resolution mode. The ion yield from nitrogen displays five clearly-resolved vibrational structures at about 401 eV $1s \rightarrow 2p^*$ resonance (Fig. 12). This demonstrates that the achieved instrumental resolution is about 4700. This is the third best resolution ever achieved with a monochromator covering K edges of the elements C, N, O, and F.

A. Yagishita

Present Status of BL-13

BL-13 was designed and built in FY 1986-1987 as a 27-pole wiggler (MPW)/undulator (U) beamline to cover the hard X-ray (4-25 keV) and the soft X-ray (50-1000 eV) regions. BL-13 consists of two hard X-ray branch beamlines, BL-13A and BL-13B, which were constructed and partly in operation and a soft X-ray branch beamline BL13C which is currently under construction.

Since the BL-13-MPW was operated with full power, i.e., 300 mA, 1.5 T on Oct. 16, 1989, the effect of heat load on the first crystal has been studied. The calculated maximum total power is 6.73 kW. Absorbers consisting of five 0.13 mm thick graphite foils were inserted in front of the water-cooled Be windows (200 μm × 2). A direct water cooling scheme proposed by Oversluizen et al. was used to cool the first Si(111) crystal as shown in Fig. 13. A typical cooling fin width and the channel width are 0.8-1 mm. The profile of the rocking curve has been measured as a function of magnetic field and stored current while the surface temperature distribution was measured by an infrared TV camera. With a regulated water flow of 12 l/sec at 20°C, the maximum surface temperature at full power was 35°C. In Fig. 14, profiles of rocking curve for the 111 reflection with θ=12.7° (9 keV) are shown. Peak height and integrated intensity of the 111 reflection are shown in Fig. 15 as a function of magnetic field and stored current. Above 1.0 T, the peak height does not increase linearly with stored current although the integrated intensity still increases almost linearly with stored current, which saturates above 1.25 T due to the deformation of crystal. The results indicate that the present crystal cooling is inadequate from the viewpoint of not only beam intensity but also energy resolution. The total energy resolution of the spectrometer which is a convolution of the width of the rocking curve and the divergence of the source is now

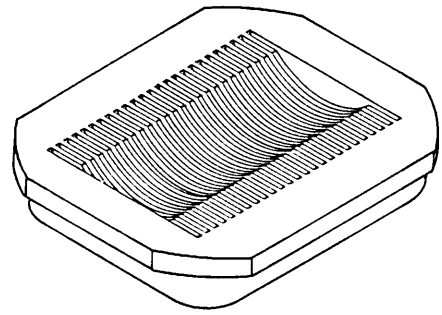

Fig. 13 Schematic back view of the first Si(111) crystal. The width of each fin and water channel is 0.8 mm and 1 mm, respectively.

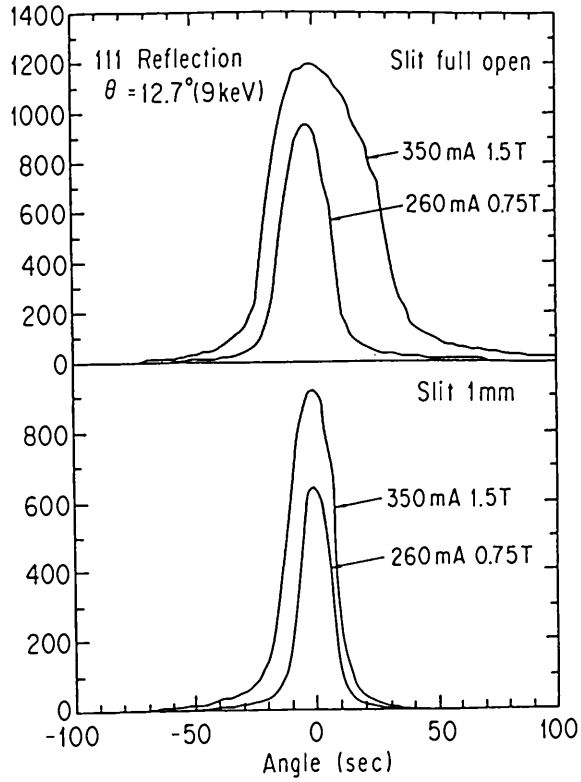

Fig. 14 Profile of the rocking curve for the 111 reflection with θ=12.7° plotted for various magnetic field strengths and stored currents.

a function of the stored current. More effective crystal cooling with a fin/channel width of 0.5 mm is planned. Two other problems related with crystal cooling at high-power beamlines are an additional degradation of the energy resolution caused by vibrations of the crystal and instability due to thermal expansion of mechanical components. The turbulence of the water flow was minimized by lowering the water pressure by additional pumping of outlet flow and by a double tube cooling system in vacuum. Ceramic materials with low coefficients of thermal expansion were successfully used as mechanical components. As a result, a highly stable monochromatized beam is presently obtained with intensity roughly an order of magnitude higher than from normal bending-magnet radiation. A typical focus size is 1 mm × 4 mm with sagittal focusing. In conclusion, the final energy resolution can be readily used for EXAFS experiments, although further improvements in crystal cooling are necessary for absorption spectroscopy such as XANES.

H. Oyanagi

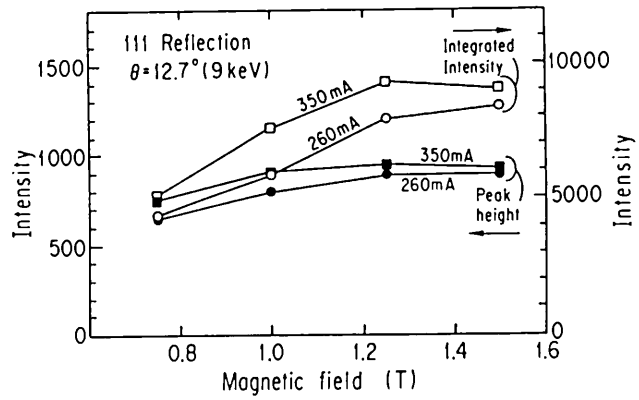

Fig. 15 Peak intensity and integrated intensity of the 111 reflection with θ=12.7° as a function of magnetic field.

Performance of BL-18A

BL-18A has been constructed to be dedicated to photoemission experiments of surfaces and interfaces with high energy and angle resolutions, as a joint project between the Synchrotron Radiation Laboratory of the Institute for Solid State Physics (ISSP), University of Tokyo and KEK-PF. The beamline is laid out for photon energies from 10 to 150 eV and equipped with a constant-deviation-angle grazing-incidence monochromator and an angle-resolved photoelectron spectrometer (VG ADES 500).

To obtain photoelectron spectra with energy resolution higher than 0.1 eV at 20 eV and angle resolution of ± 0.5°, the entrance and exit slits of the ADES 500 hemispherical electron energy analyzer were replaced by new ones with smaller aperture. The schematic diagram of the monochromator is shown in Fig. 16.

The performance of the monochromator and the ADES 500 photoelectron spectrometer were examined by measuring the photoelectron spectra of clean and metal-adsorbed Si(100) surfaces and some rare earth compounds.

The beamline will be open to users from April 1991.

A. Kakizaki

Performance of BL-19A - Revolver Undulator -

The revolver undulator beamline, BL-19A, has been constructed to be dedicated to photoelectron spectroscopy with high photon flux, and laid out for photon energies from 20 to 250 eV. To cover such a wide spectral range with fundamental peaks of

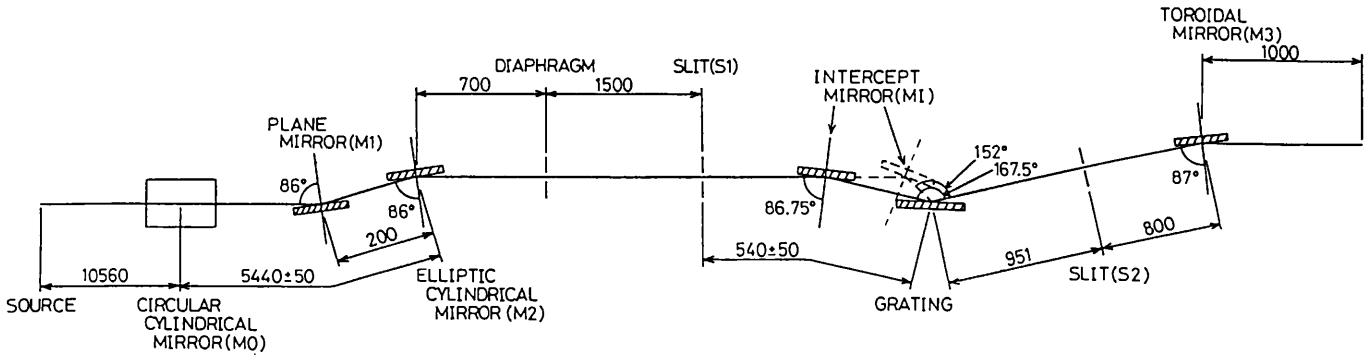

Fig. 16 Schematic diagram of BL-18A.

the undulator radiation, the revolver consists of four pairs of permanent magnets which have different period lengths and tunable magnet gaps. The deviation of the positron beam trajectory due to the magnet gap change is corrected using horizontal and vertical steering magnets at both ends of the undulator. Correction currents of the steering magnets were determined by measuring and minimizing the difference of the closed orbit distortion around the ring. In FY 1990, the scanning of the undulator magnet gap has been accomplished during the normal user-beam-time.

Figure 17 shows the photoelectron yield spectra of Au by using higher harmonics of the undulator with K=5.67 (upper figure) and the spectra by scanning the magnet gap from 81 mm to 98 mm (lower one), i.e. from K=3.49 to 2.47, respectively. Intensities of fundamental peaks are much larger than those obtained by using higher harmonics in this photon energy range. The envelope of the fundamental peaks reflects the transmission of the constant-deviation-angle grazing-incidence monochromator (CDM) with 1200/mm grating of 2 m radius. The maximum photon flux was estimated to be ~ 7×10^{13} photons/sec/mm^2 at 90 eV with a 600/mm grating of 4 m radius using 100 μm entrance and exit slits in the CDM. This value is an almost two orders of magnitude greater photon flux than the one derived from dipole radiation with the same divergence of radiation.

A. Kakizaki

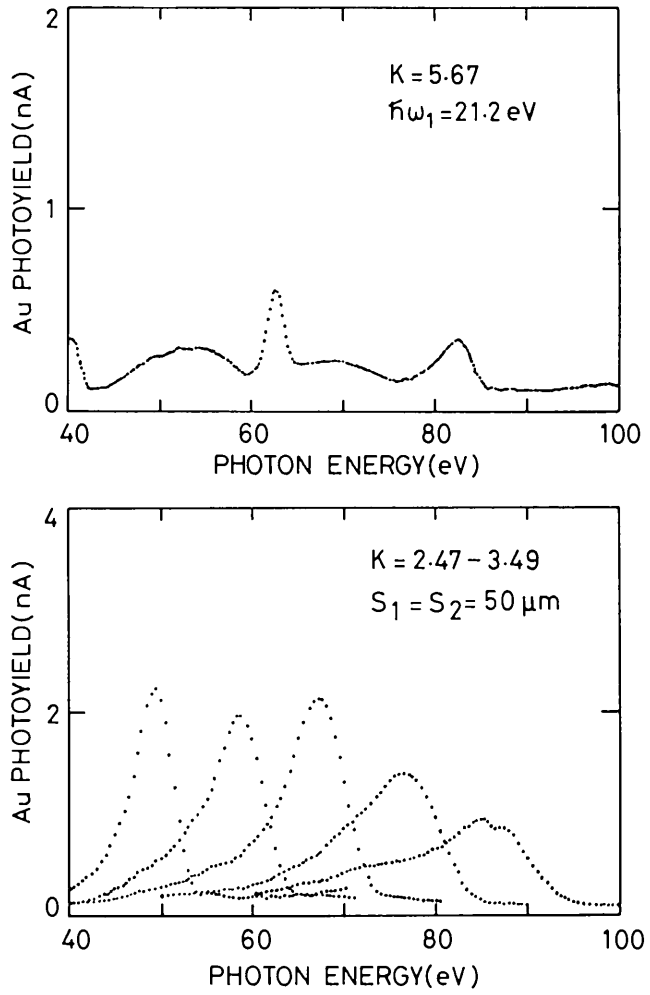

Fig. 17 Photon flux spectra of first harmonics for K = 2.47 - 3.49 (magnet gap = 81 - 98 mm), comparing with higher harmonics radiation of K = 5.67.

Feedback System for Vertical Beam Position at BL-3A

Stabilizing the vertical beam position is very important for all experiments using synchrotron radiation. A new feedback system having piezoelectric translation and beam position monitors with fast analog circuits has been installed for a double-crystal monochromator at BL-3A (Fig. 18). In this system the first crystal of the monochromator is moved vertically to keep the height of the outgoing beam constant. When the incident beam drifts up and down with a displacement of Δx, the distance between two crystals,

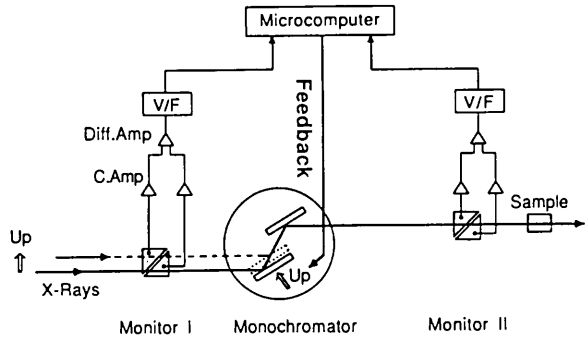

Fig. 18 Feedback system of BL-3A.

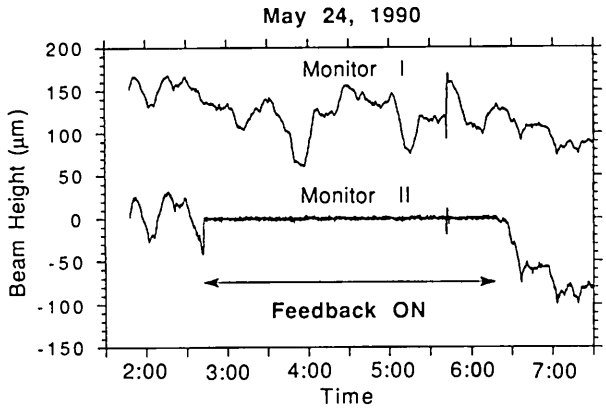

Fig. 19 Suppression by the feedback during normal user-time operation. The measurement started at 1:48 a.m. on May 24, 1990.

ΔD, becomes smaller and larger, respectively, according to $\Delta D = -\Delta x/(2\cos\theta_m)$, where θ_m is the Bragg angle of the monochromator.

Figure 19 is an example of performance tests of the feedback system. Monitor I recorded the drift of the height of the incoming beam. The drift of the height of the outgoing beam was observed by using monitor II placed in the experimental hutch when the feedback was ON/OFF. With the feedback ON, it was kept within about 10 μm which corresponded to the signal/noise limitation of the monitor II. EXAFS measurements were made to show that the X-ray energy of the monochromatized beam did not change during the feedback; the fluctuation of the X-ray intensity at the K absorption edge of Cu atoms was much reduced when the feedback was ON. Absorption spectra were measured for a Cu foil of 6 μm thickness and the Fourier transformation of $k^3\chi(k)$ was carried out successfully.

A. Koyama, S. Sasaki, and T. Mori

Improvement of the Sagittal Focusing Double-Crystal Monochromator

The sagittal focusing double-crystal monochromator developed by Prof. Matsushita[1] has been used at several beamlines because of its focusing ability and its ease of operation. However, we experienced several problems; the focusing is not so satisfactory sometimes and the output photon flux changes significantly during scanning of the Bragg angle. Dr. Kawata found that the in-plane rotation of a sagittally bent crystal restricts the focusing property; the glancing angle changes from place to place when the axis of bending is not parallel to that of the incoming X-rays.[2] Thus a rotation stage has been added to the second crystal holder of the monochromator installed at BL-6B and 7C in order to realize the in-plane rotation. The required correction-angle (γ) can be easily calculated from the difference of the positions of the rocking curves at the right and left halves of the crystal, which is usually within 1°. The effect of the crystal rotation is shown in Fig. 20. Here Si(111) was used as the monochromator and the Bragg angle was set at 25°. When $\gamma = 0.35°$ the positions of the rocking curves at both halves of the crystal were differed by 27 arcsec. But they coincided with each other at the optimum setting ($\gamma = 0.0°$). This improved the energy resolution. At the same time the photon flux increased by 60 %. The rather wide rocking curve may be due to the distortion of the crystal during manufacturing and the wide aperture of the entrance slit; 10.2 arcsec was observed at 9 keV by using another crystal.

Though the focusing property was improved, the variation of intensity became more significant by introducing the rotation mechanism. This problem was solved by increasing the rigidity of both the first and the second crystal holder. The variation of the parallelism between two crystals was improved to *ca.* 10 arcsec during a scan from 5° to 40°, which makes the operation of the monochromator easier and makes it possible to use crystals of higher indices, such as Si(311).

A. Koyama, and M. Nomura

1) Photon Factory Activity Report #4(1986) p. 93.
2) Photon Factory Activity Report #7(1989) p. I-10.

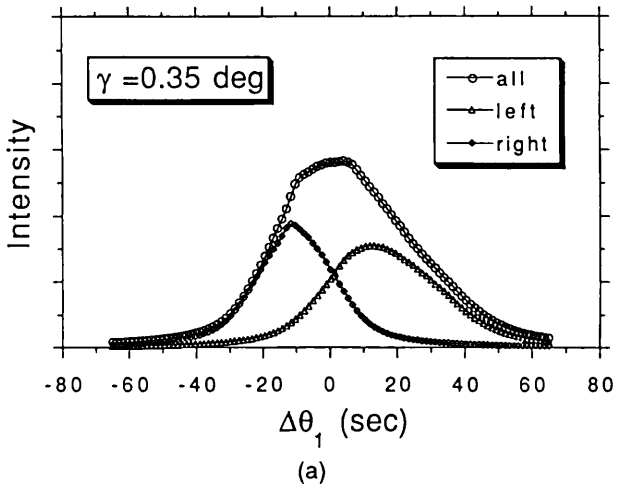

(a)

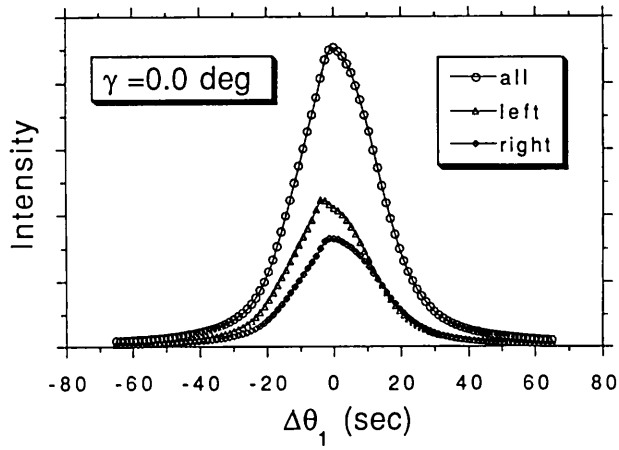

(b)

Fig. 20(a) The positions of two rocking curves at the right and left halves of the Si(111) crystal monochromator are separated by 27 arcsec when γ = 0.35°. (b) The positions of the two rocking curves coincide with each other when γ = 0.0°. The photon flux increases by 60%.

C. NEW INSTRUMENTATION

Fuji Imaging Plate Scanner (BAS2000)

The imaging plate (IP) has been actively used in many of the X-ray experiments at PF. In order to meet the increasing demand to use the imaging plate, a Fuji laser scanner, called BAS2000, was purchased and connected through Ethernet to the drum-type laser scanner which was developed at PF (Fig. 21). In the BAS2000, scanning of a 10 mW He-Ne laser is performed with an oscillating mirror, while the IP is traversed so as to form an orthogonal scan. The BAS2000 can read IPs sized 20 cm × 25 cm and 40 cm × 25 cm. The pixel size is 100 μm × 100 μm or 200 μm × 200 μm and the data are of 8 or 10 bits. The BAS2000 is very easy to operate owing to (1) automatic loading of the IP with a special imaging plate magazine designed for operation outside a dark room and (2) friendly mouse-controlled commands under an UNIX window with a SUN 3/80 computer. It takes 3 minutes to scan an imaging plate of 20 cm × 40 cm with a pixel size of 100 μm × 100 μm. In order to permit as many users (scans) as possible with the BAS2000 successively, those users who wish to work on the image data under the BAS2000 graphic software are requested to move to another computer (SUN 3/470) which is connected to the BAS2000 via Ethernet. Data can be dumped on 1/2 inch magnetic tape via the SUN 3/470 computer. A high-resolution hard copy printer, called FUJIX PICTROGRAPHY, is available.

The BAS2000 is intended for use in experiments which require many exposures of IPs with the standard sizes, whereas the home-made drum-type laser scanner is intended for experiments which require a higher spatial resolution (50 μm or 25 μm pixel size), a higher precision in intensity (12-bit A/D conversion), a wider dynamic range than 4 orders of magnitude, or the flexibility for use with arbitrary sizes of IPs.

Besides the above two laser scanners, two prototype Fuji IP scanners (BA100) and a drum scanner designed for time-resolved experiments are also actively used at PF. BA100s are used dedicatedly with a Weissenberg camera at BL-6A2 for protein crystallography.

Y. Amemiya

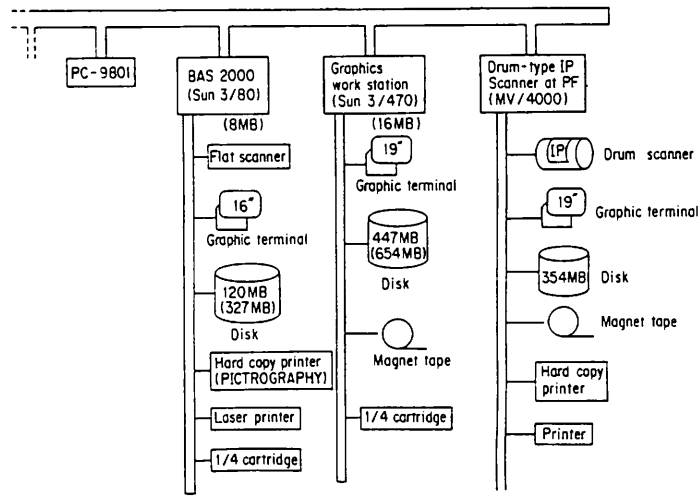

Fig. 21 Network of Imaging Plate scanners at PF.

He-3 Dilution Refrigerator for X-ray Topography of Solid Helium

The first He-3 dilution refrigerator (hereafter referred to as He-3 DR) installed in BL-6C1[1] was used successfully for the study of magnetic properties of some materials at ultralow temperatures. The second He-3 DR for X-ray topography of solid helium has been installed in BL-3C2 with a special goniometer system and a special camera system using nuclear plates.

The He-3 DR was purchased from Oxford Instruments Inc. It has a beryllium sample chamber which can rotate around the two orthogonal axes by a rotating system. We cannot control the orientation of a helium single crystal grown in the sample chamber, hence we must tilt the sample chamber to adjust the orientation of the helium crystal so that appropriate diffraction could be observed at $2\theta = 90°$ perpendicularly for a horizontal incident X-ray beam (Fig. 22). The sample chamber and its rotating system were manufactured by Takayosi Suzuki in the machine shop of the Institute of Industrial Science, University of Tokyo according to the idea of H. Suzuki.

The first test drive of He-3 DR was done with Oxford Inc. in June 1990 without the sample chamber and its rotating system, and the base temperature easily reached 7.8 mK. At the end of October the sample chamber and its rotating system were installed into the cryostat of the He-3 DR. In December, the second test drive of the He-3 DR with the sample chamber and its rotating system was performed. The heat load of the sample chamber and its rotating system caused serious difficulty in cooling down to fixed temperatures. The difficulty seems to be due to the poor thermal contact of the sample chamber and its rotating system with the liquid helium bath and the 1 K pot. Improvement of the thermal contact of the sample chamber and its rotating system will be performed at the beginning of 1991.

This equipment will be used for the direct observation of lattice defects in hcp and bcc ^{4}He, hcp and bcc ^{3}He, and ^{3}He-^{4}He mixtures in order to investigate the quantum mechanical behavior of lattice defects.

H. Suzuki & T. Nakajima

1) Photon Factory Activity Report #6(1988) p. I-16.

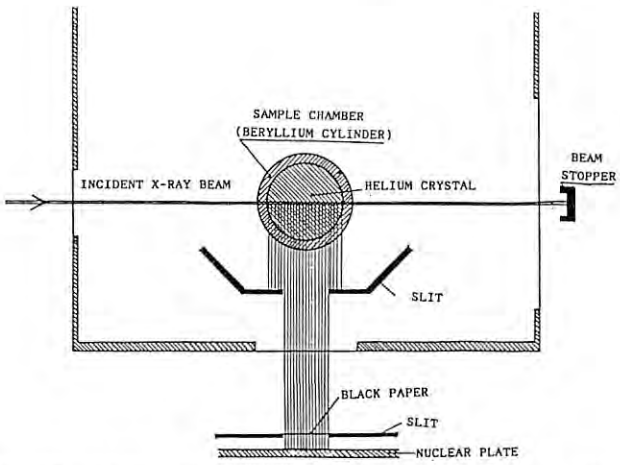

Fig. 22 Sample chamber and position of the nuclear plate. The rotating system of the sample chamber and radiation shields around it are omitted.

Cooling System with Single-Crystal Diffractometer at BL-10A

BL-10A is currently used for crystal-structure analyses and scattering experiments with a vertical-type four-circle diffractometer. During this period a cooling and heating system has been installed for accurate single-crystal diffraction studies. The device uses liquid nitrogen to generate a cold or hot gas stream in the temperature range between 100 and 900 K. The system includes the evaporator, storage and supply dewars, the automatic refilling system, flexible vacuum insulated line, and stainless-steel dewar tube. A photograph of the gas outlet (nozzle) is shown in Fig. 23.

Nitrogen gas is taken from a storage dewar by a gas-pressure environment from a nitrogen cylinder. The gas passes through the flow control and is blown directly onto the crystal mounted on the diffractometer. The device has the following characteristics: (1) flexible data collection without geometrical shadow, (2) warm/dry gas outer stream to avoid frost formation, (3) no absorbing materials in the beam path, (4) good stability over weeks without interruption.

S. Sasaki

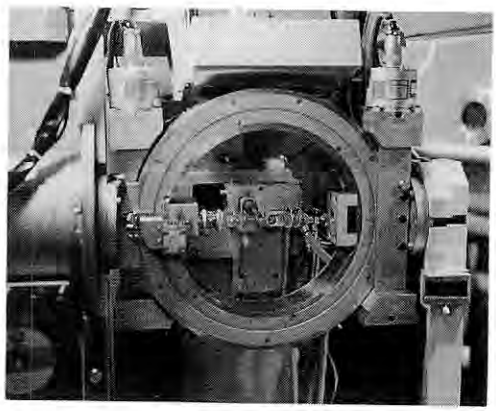

Fig. 23 Nozzle for the cold/hot gas stream of the cooling and heating system and four-circle diffractometer.

X-ray Emission Spectrometer (XES)

A Johansson type high-resolution X-ray spectrometer was constructed for spectroscopic use with soft X-ray fluorescent emission originating from the M-shell vacancy of rare-earth metals and their compounds. The spectrometer was designed to be attached dedicatedly to the undulator beamline BL-2A. The beamline provides 1 to 3 keV soft X-rays with a high flux in a narrow cone of a few tens of microradians when higher harmonics are used

The Rowland circle radius is 250 mm. The ADP (101, 2d = 10.640 A) and RAP (001, 2d = 26.121 A) are used as spectrometer crystals. When these crystals are scanned with incidence angles from 75° to 15°, the photon energy range from 0.5 keV to 4.5 keV can be covered.

The Rowland circle mounting is realized by a pulley-driven mechanical linkage with a moving pivot at the center of the circle and a fixed pivot at the sample point which coincides with the position of the entrance slit. The incident light beam is focused finely on the sample with a mirror of ellipse in such a way that the fluorescent portion of the sample becomes as the virtual entrance slit.

The spectrometer has two manipulators for the sample and the prefocusing mirror, respectively. It also has an e^--gun system for spectrometer alignment. The spectrometer chamber can be attached to the beamline rotated by a right angle around the incident light beam to study polarization effects on the fluorescence spectra.

H. Maezawa

Production and Direct Measurement of VUV Circular Polarization with Reflection Optics

Much interest has recently been devoted to the generation and application of circularly polarized synchrotron radiation (CPSR) in the vacuum ultraviolet (VUV) and soft X-ray (SX) regions. However, a lack of a suitable $\lambda/4$ retarder has hindered complete polarization analyses in these regions.

Figure 24 shows a schematic view of the experimental arrangement to produce CP in the VUV by two different methods at a normal bending-magnet beamline and to completely analyze its polarization state with reflection optics. In the first experiment,[1] off-plane CPSR was extracted with the entrance slit of the monochromator by deflecting the incoming beam vertically with the beamline's first premirror. The Stokes parameters of the emerging beam were measured with a polarimeter comprising two triple-reflection polarizers P_1 and P_2 in conjunction with detector D. In the second experiment,[2] the conversion of linearly polarized SR (LPSR) to CPSR was attempted by using a triple-reflection $\lambda/4$ retarder, CP_0, as proposed by Johnson and Smith.[3] The resulting beam was polarization-analyzed with the polarimeter.

The monochromatized SR beam was collimated with a fixed pinhole diaphragm, FH, and incident onto P_1 (first experiment) or CP_0 (second experiment). All of CP_0, P_1 and P_2 can be rotated independently around their axes by 360° under vacuum; their rotation angles are denoted by θ, α and β, respectively. When the Stokes vector of the light to be analyzed is $S=(S_0, S_1, S_2, S_3)$, the state of polarization is completely specified by S_1/S_0, S_2/S_0 and S_3/S_0. They all can be determined with three polarizing quantities of the polarimeter by measuring the transmitted light intensities for seven independent pairs of rotation angles (α, β).[1,2] A GaAsP photodiode was used as detector. The measurements were made on BL-11D at an average ring current of 300 mA with a maximum slit width of 200 μm. The polarimeter chamber was kept at a pressure of $\sim 1 \times 10^{-8}$ Torr.

Off-plane CPSR (first experiment)[1]

The Stokes parameters were measured over the 25-80 eV range for three different beam-deflection angles. Increasing the deflection angle resulted in a change in the polarization state from predominantly linear polarization (LP) to elliptical polarization (EP).

Figure 25 shows the degree of CP($= S_3/S_0$) and of horizontal LP($= S_1/S_0$) measured at 60 eV as a function of the deflection angle. The present results together with those at other energies show that the maximum degree of CP of up to $|S_3/S_0| \gtrsim 80$ % could be obtained over the 60-80 eV range. The MCD studies using off-plane CP are presented in a following article of this issue.

Triple-reflection circular polarizer (second experiment)[2]

Figure 26 shows the Stokes parameters, S_1/S_0 and S_3/S_0, measured at 30 eV for the output beam of CP_0 as a function of its rotation angle.

The measured degree of CP (S_3/S_0) is seen to be nearly odd in θ, showing right- and left-handed EP, respectively. This result indicates the feasibility of an easy switching of the photon helicity. The maximum values of the degree of CP, $S_3/S_0 \approx \pm 82$ %, were achieved at angles $\theta \approx \pm 25°$, respectively, in fairly good agreement with the calculation. The deviation from complete CP arises mainly from the incomplete

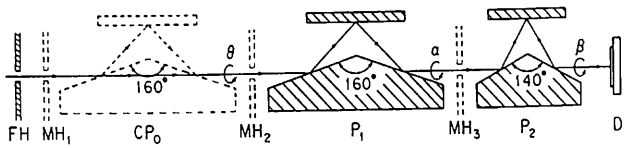

Fig. 24 Experimental arrangement for the production and analysis of circularly polarized VUV light with reflection optics. CP_0: circular polarizer; P_1: quasi $\lambda/4$ retarder; P_2:LP analyzer; D:GaAsP photodiode; FH:fixed pinhole diaphragm; MH_1~MH_3: removable pinhole diaphragm.

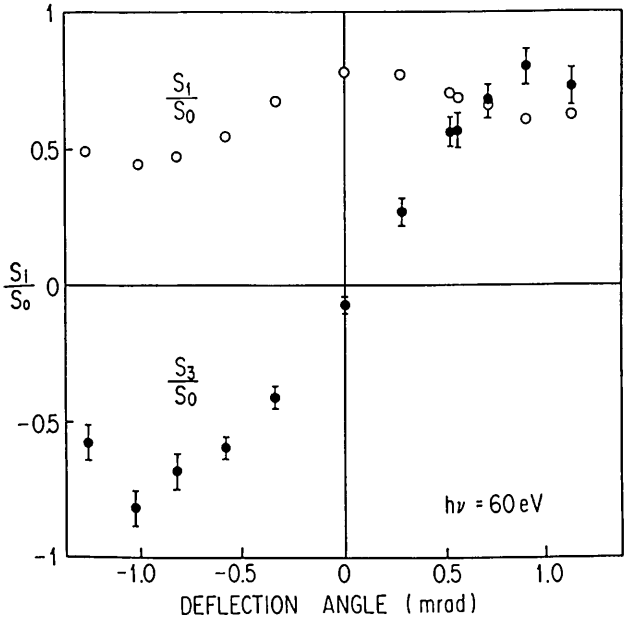

Fig. 25 Stokes parameters S_1/S_0 and S_3/S_0 (degree of CP) measured at 60 eV for the emerging beam of BL-11D as a function of vertical beam-deflection angle.

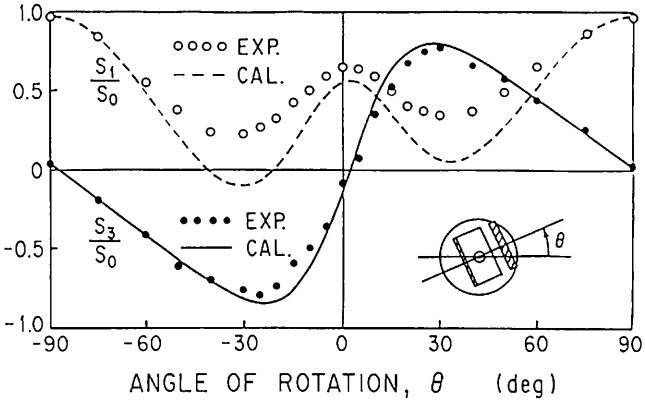

Fig. 26 Measured and calculated Stokes parameters S_1/S_0 and S_3/S_0 (degree of CP) at 30 eV for the emerging beam from the circular polarizer CP_0 as a function of its rotation angle.

LP of the incident beam ($S_1^{in}/S_0^{in} < 1$), and partly from a small deviation of the circular polarizer CP_0 from a perfect $\lambda/4$ retarder.

T. Koide

1) T. Koide et al.: Nucl. Instrum. Methods (submitted).
2) T. Koide et al.: Appl. Phys. Lett. (submitted).
3) P. D. Johnson and N. V. Smith: Nucl. Instrum. Methods 214 (1983) 505.

UHV Superconducting Magnet for MCD and Photoemission Spectromicroscopy Experiments

Magneto-optics is a powerful technique for studying the spin-dependent electronic states of materials. A high-field magnet is desired for such experiments, because the magnetic-field-induced perturbation energy (i.e., Zeeman splitting) is very small (an order of 1 meV for a 10 T field) in paramagnetic substances.

We have designed and constructed a bakable superconducting-magnet system for uses in magnetic-circular-dichroism (MCD) and magnetic-imaging photoemission-spectromicroscopy (MIPESM) experiments in the VUV and SX regions. Figure 27 shows its cross-sectional views and the optical path in MCD measurements. The magnet is a split-coil solenoid producing fields of up to 5.8 T. Field homogeneity at the center is better than 0.36 % within a sphere of 10 mm diameter. The magnet coil is made of NbTi wire, thus allowing easy switching of the field direction unlike that made of Nb_3Sn wire. The key aspect of this magnet system is a double-wall structure for a liquid-He cryosystem. This enables us to bake out the outer wall without any appreciable rise in the magnet temperature. The standing time of the magnet is 15 ~ 16 h without liquid-He refilling at 5 T operation. The central part of the double-wall structure is composed of vacuum ducts extending toward three directions perpendicular to each other. The vertical duct permits access of the sample holder introduced from outside the vacuum chamber through a lower port. The sample holder (made of Cu) is attached to a modified OXFORD He-gas-flow cryostat and its temperature can be varied from 300 to 4.2 K.

The whole system is evacuated with a 110 l/s noble pump in conjunction with a 400 l/s magnetically-levitated turbomolecular pump with a magnetic shielding. Slight bakeouts have led to a pressure of ~1 $\times 10^{-9}$ Torr, sufficiently low for MCD measurements. A full bakeout will be soon done for MIPESM experiments. Light is incident on the sample through

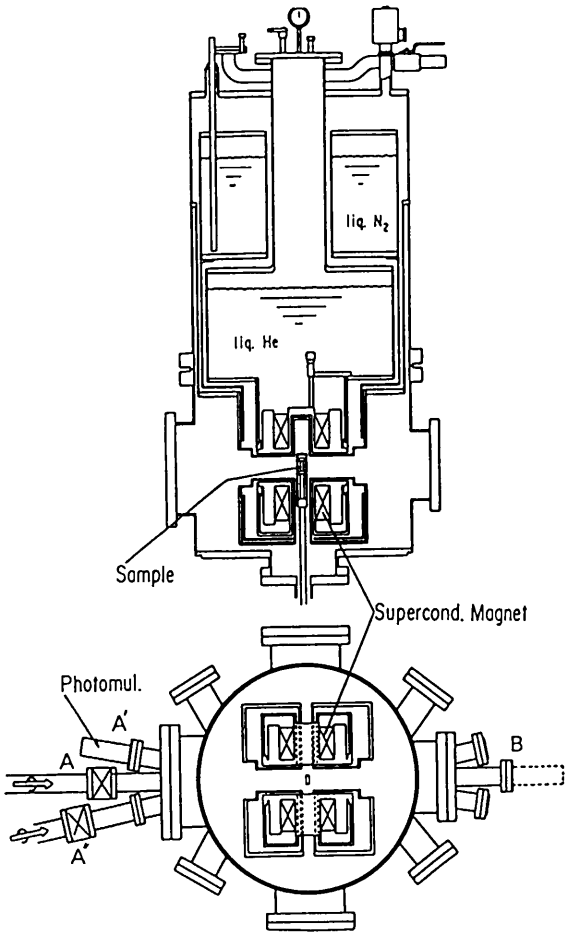

Fig. 27 Cross sections of the bakable 5.8 T superconducting magnet system.

port A and transmitted or reflected light is detected at ports B or A' in MCD measurements (Fig. 27). In MIPESM experiments, the light beam will enter through port A" and photoelectrons emitted from the sample should be transferred through port A to be detected at a position ~ 2 m away from the magnet center. Results of MCD studies were described in a previous issue of this report [1] and are also presented in a following article of this issue.

T. Koide

1) T. Koide et al.: Photon Factory Activity Report #7 (1989) p. 265.

Apparatus for MCD Absorption Measurements

The apparatus was designed and constructed for photoabsorption measurements to study magnetic circular dichroism (MCD) of various magnetic materials. It is equipped with an electron gun for vacuum evaporation, a permanent magnet flipper, and an air-lock system to introduce sample substrates. The permanent magnet flipper is similar to a single period of undulator magnets, but has two holes to allow the incident light to go through. The maximum magnetic field at the sample position is 12 k gauss and its direction is switched by a linear motion of the magnet flipper. The thickness of deposited film is monitored by a quartz thickness monitor. Both the sample holder and the thickness monitor can be cooled to liquid nitrogen temperature. The apparatus is basically an ultrahigh vacuum system. Special care has been taken to keep the temperature of the magnet flipper lower than 100 °C during bakeout of the vacuum chamber. The detector is a photomultiplier covered with a magnetic shield, by which spurious MCD signal was reduced to less than 0.01 %.

One of the results of the test operation of the apparatus connected to BL-28 is shown in Figs. 28(a) and (b). In this experiment the direction of circular polarization was fixed while the magnetic field was

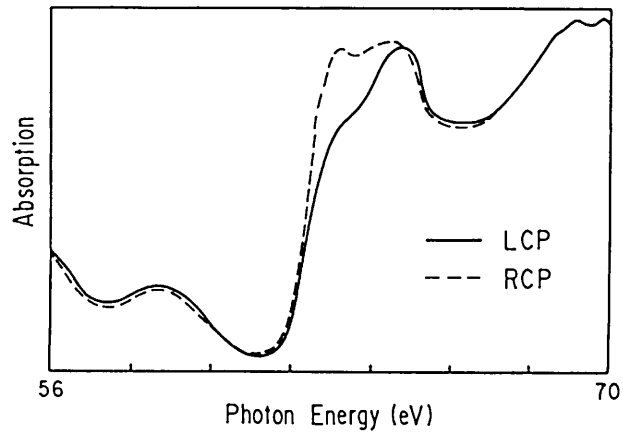

(a)

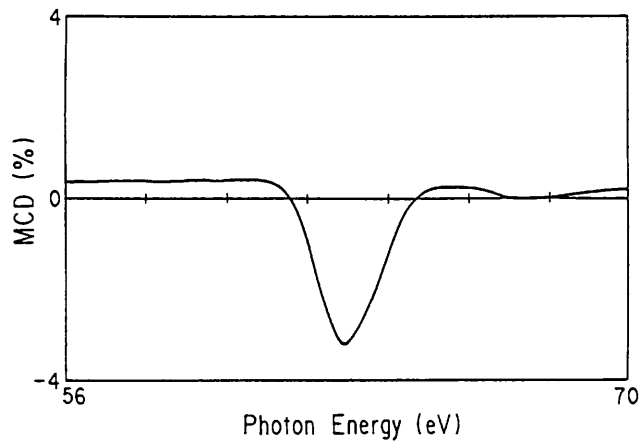

(b)

Fig. 28 (a) Photoabsorption spectra of Ni for right and left circularly polarized light in the region of the 3p → 3d excitation. (b) Magnetic circular dichroism of Ni defined by the ratio between the difference and the sum of the LCP and RCP absorption coefficients.

switched at each photon energy. Figure 28(a) shows the comparison between the $M_{2,3}$ absorption spectra of Ni in the two alternative magnetic fields. Figure 28(b) shows the MCD signal defined by $(I_L - I_R)/(I_R + I_L)$, where I_L and I_R are the absorption coefficients for the two alternative magnetic fields corrected by subtraction of the background contribution to the absorption coefficient. It is seen from these results that the energy-integrated MCD signal does not vanish though it would vanish if the orbital angular momentum of valence electrons is totally quenched. Thus the present results indicate that the orbital angular momentum makes an appreciable contribution to the magnetic moment of ferromagnetic Ni.

Through these results together with the result of a theoretical calculation, it is suggested that the circular polarization of the light actually obtained through the monochromator at BL-28 is larger than 70 % in the present photon energy range.

T. Miyahara

D. HIGHLIGHTS OF EXPERIMENTS

Soft X-ray Polarization Measurements with Use of a Multilayer Phase Shifter and Polarizer

We describe here our method and the result of the first attempt of the complete polarization measurement including the handedness with use of a multilayer phase shifter and polarizer.

Figure 29 shows the calculated s-reflectance R_S and p-reflectance R_P of an ideally flat Ru/Si multilayer (21 layer, 3.95 nm/5.4 nm) as a function of the angle of incidence ϕ at a photon energy of 97 eV. The reflectance increase in R_S is much larger than that in R_P at $\phi \simeq 45°$ since the pseudo-Brewster angles of all materials in this photon energy are around 45°. Thus, all multilayers can be used as polarizers at $\phi \simeq 45°$. Furthermore, this angle is close to the principal angle of incidence ϕ_P of the multilayer mirrors. This means that the mirror can be used as a phase shifter if we select the angle of incidence within a peak of R_P, which is indicated by the hatched area in Fig. 29.

Figure 30 illustrates a vertical view of the setup of our polarization measurement. In the chamber of the apparatus for optical element characterization[1], we mounted the phase shifter(P) and the analyzer assembly(A). Two multilayer mirrors for P and A were cut out from a single Ru/Si multilayer mirror. The micro-channel-plate detector(D) is attached rigidly to the assembly A. In this configuration, the assembly A can be rotated in the chamber to change its azimuth η and the chamber can be rotated so as to change the azimuth χ of P. The azimuths χ and η are measured counterclockwise from the orientation shown in the figure. It should be noted here that the retardation of A gives no effect to the intensity of the beam entering the detector D, whereas that of P effectively transforms the state of polarization.

At a certain azimuth χ, the polarized incident beam with ellipticity angle ε and azimuth δ is transformed in a particular way, defined by χ, to the ellipse with azimuth angle η^*. Therefore, if we measure at various azimuths χ the azimuthal angle η^* of the reflected polarization ellipse by a rotation of the assembly A giving a cosine squared curve (Malus' law), we can find the quantities associated with the incident light, i.e. δ and ε and those with P, i.e. $\alpha = |R_S/R_P|$ and the retardation Δ by using the function

$$\tan\eta^* = \frac{2\alpha[\cos 2\varepsilon \sin 2(\delta-\chi)\cos\Delta + \sin 2\varepsilon \sin\Delta]}{\alpha^2 - 1 + (\alpha^2+1)\cos 2\varepsilon \cos 2(\delta-\chi)}.$$

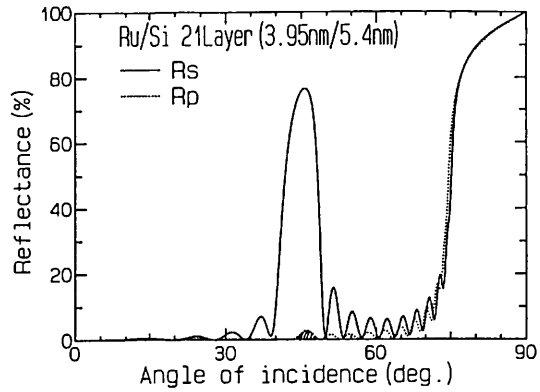

Fig. 29 Reflectance of an ideally flat Ru/Si multilayer.

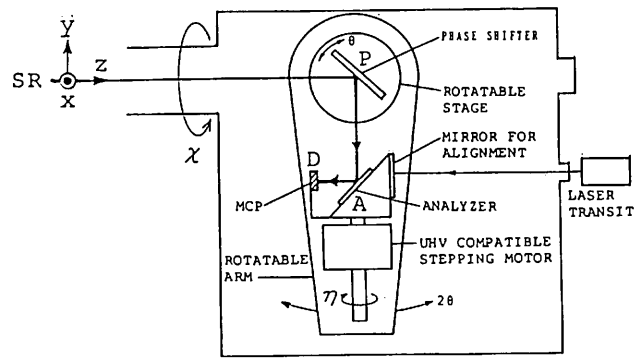

Fig. 30 Schematic of polarization measurement apparatus.

ϕ (M_0 vertical inclination)	angle of incidence at P	α $\lvert R_s/R_p \rvert$	Δ(deg.) (retardation)	ε(deg.) (ellipticity angle)	δ(deg.) (azimuth of the ellipse)	degree of linear polarization*
0.25°	45°	7.74±0.72	-35.9±7.8	-15.8±1.6	-4.86±2.50	0.85±0.03
0°	43°	31.7±2.8	-21.4±12.3	-4.5±1.7	-0.53±1.47	0.99±0.01
-0.25°	45°	7.73±1.42	-35.0±6.7	13.1±2.3	3.21±2.96	0.90±0.03
-0.45°	45°	7.74±1.80	-37.5±8.8	18.9±2.6	5.56±4.74	0.79±0.05

*Calculated by the ellipticity angle ε.

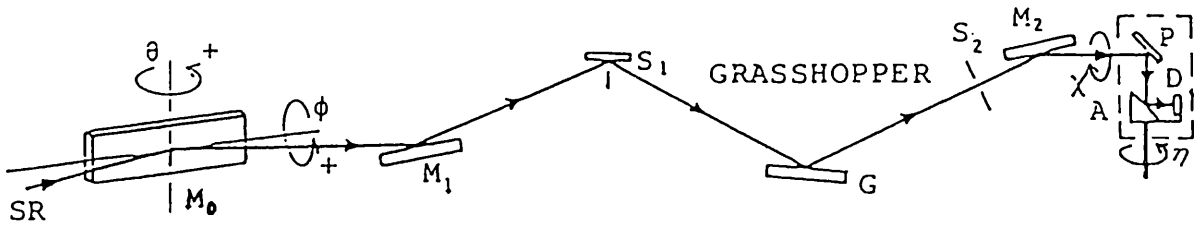

Fig. 31 Schematic diagram of polarization measurements at BL-11A.

The polarization of the 97 eV light from the grasshopper monochromator was measured in the way described above at four typical attitudes selected by the vertical inclination ϕ of the mirror M_0 at BL-11A (see Fig. 31). The origin of ϕ was chosen arbitrarily. Figure 31 shows the quantities determined. The mirror for the analyzer assembly was fixed at the angle of incidence of 45° at which the s-reflectance, α, and the polarization measured independently were 60 %, 8.4, and 0.97, respectively. The αs in the table with 45 ° incidence angle at P agree well in spite of the difference in the polarization state of the incident beam and they are also close to 8.4 above. This demonstrates the good reliability of the present polarization measurements. The non-zero azimuths cannot be explained readily but the ellipticity angles agree well with the theoretical prediction including the handedness[2].

H. Kimura & M. Yamamoto

1. Shichiro Mitani et al.: Rev. Sci. Instrum. 160 (1989) 2218.
2. H. Kitamura: Insertion Device Handbook (Photon Factory, 1990) p. 80

Magnetic Circular Dichroism at the $M_{2,3}$ Absorption Edges in 3d Transition Metals and Compounds

We have obtained successfully MCD spectra around the $M_{2,3}$ edges in ferromagnetic Ni and Fe, ferrimagnetic Fe_3O_4, and Fe/Pt multilayered structure. MCD signals were also observed at the $N_{6,7}$ edges in Pt for the Fe/Pt multilayer.

The production and direct measurement of CPSR as well as the development of a UHV superconducting magnet are described in preceding articles of this issue. The experiments were made in normal-incidence reflection with the Faraday configuration. Since $n \approx 1$ and $k << 1$ in this region, the reflection MCD gives essentially the same spectrum as the transmission MCD. The reflected light was detected with a sodium-salicylate-coated photomultiplier specially designed for uses under high magnetic fields. The use of a superconducting magnet allowed the confirmation of sample-magnetization saturation. The field direction was changed with the photon helicity fixed.

Figures 32(a) and (b) show the reflectance spectra for two opposite magnetization directions and the MCD spectrum of a single crystal of Ni(111), respectively. A comparison of our spectra with reported absorption spectra of Ni and NiO showed that the influence of surface oxide (NiO) was negligibly small; the present spectra show a clear bump B at ~ 80 eV existing only in Ni and no deep dip at the absorption maximum observed only in NiO. The MCD spectrum exhibits a

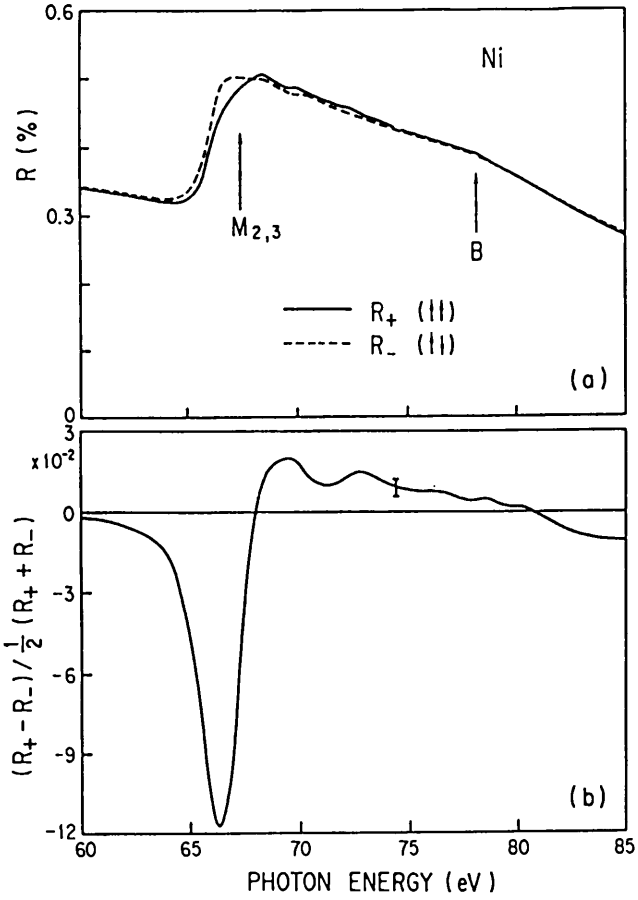

Fig. 32 (a) Reflectance spectra of Ni around the $M_{2,3}$ absorption edges for two different orientations between the spin direction of the incident photon and that of the majority 3d electrons. (b) MCD spectrum of Ni deduced from the spectra in (a).

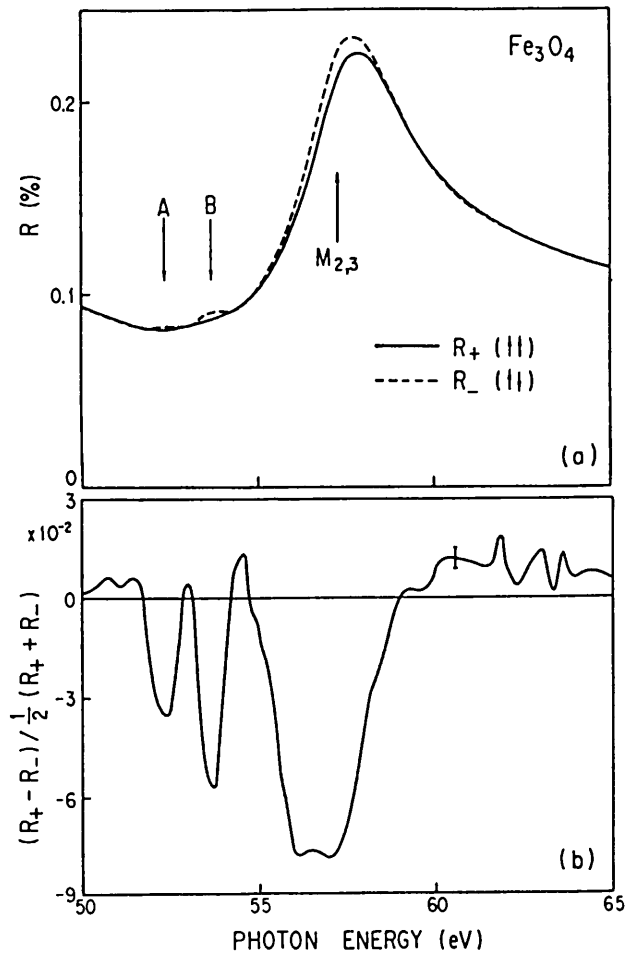

Fig. 33 (a) Reflectance spectra of Fe_3O_4 around the $M_{2,3}$ absorption edges in Fe for two different orientations between the spin direction of the incident photon and that of the majority 3d electrons. (b) MCD spectrum of Fe_3O_4 deduced from the spectra in (a). Note the strong MCD signals for weak features A and B.

large negative peak at the M_3 edge followed by a small positive peak at the M_2 edge with increasing energy. This marked asymmetry conflicts with the antisymmetric spectrum predicted by Erskine and Stern[1] who took into account only the spin angular momentum of the 3d electrons on the basis of a band calculation. The present result indicates a remaining orbital angular momentum in the ground state and is in agreement with a calculation by Yoshida and Jo which takes into account an orbital magnetic moment of 0.07 μ_B.

Figure 33 shows the results for a single crystal of $Fe_3O_4(111)$. The main peak at the $M_{2,3}$ edges exhibits a large negative MCD signal, which is similar to the behavior in Ni. However, the overall structure in the MCD spectrum is much more complicated than that for Ni. Most interesting is an abnormally strong MCD signal observed for the very weak multiplet structures A and B in the prethreshold region. A comparison of the present spectra with the reported total-yield spectra for Fe_xO and Fe_2O_3 indicates that features A and B might be identified from their energy positions as arising from transitions in Fe^{2+} and Fe^{3+} ions, respectively. The MCD signals for feature A as well as the main peak could reasonably be attributed to the magnetic moments in Fe^{2+} ions at the octahedral (16d) site. However, the large MCD signal for feature B seems to contradict a simple picture based on the above-mentioned assignment, since the magnetic moments of Fe^{3+} ions at the tetrahedral (8a) and octahedral (16d) sites are canceled out in the ground state. The strong MCD observed for the prethreshold multiplets could provide new insight into the magnetic structure, though detailed theoretical studies are required for a reasonable interpretation of the overall MCD spectrum of Fe_3O_4.

T. Koide

1) J. L. Erskine and E. A. Stern: Phys. B 12 (1975) 5016.

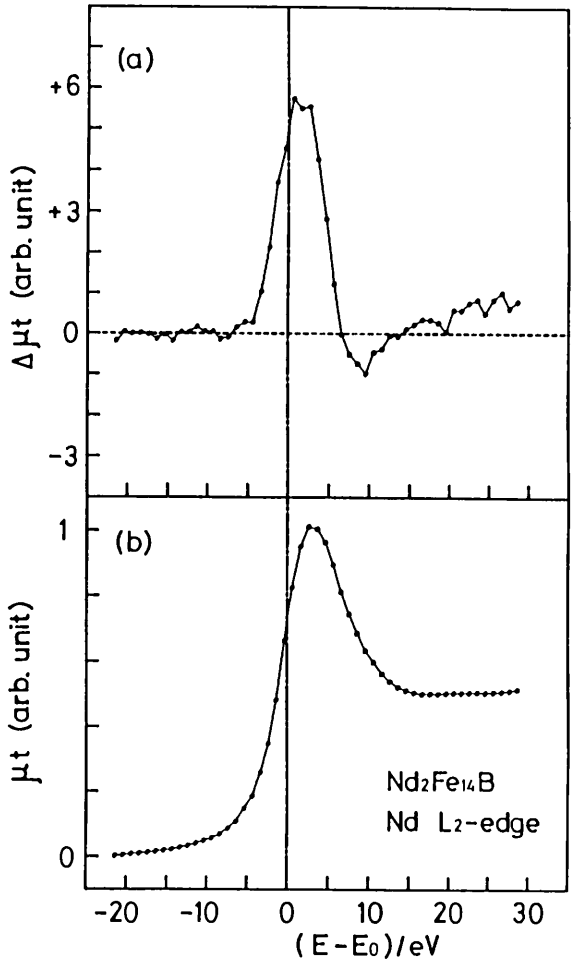

Fig. 34 (a) Magnetic and (b) usual XANES spectra at the L_2 edge of Nd in $Nd_2Fe_{14}B$ taken by the fluorescence method.

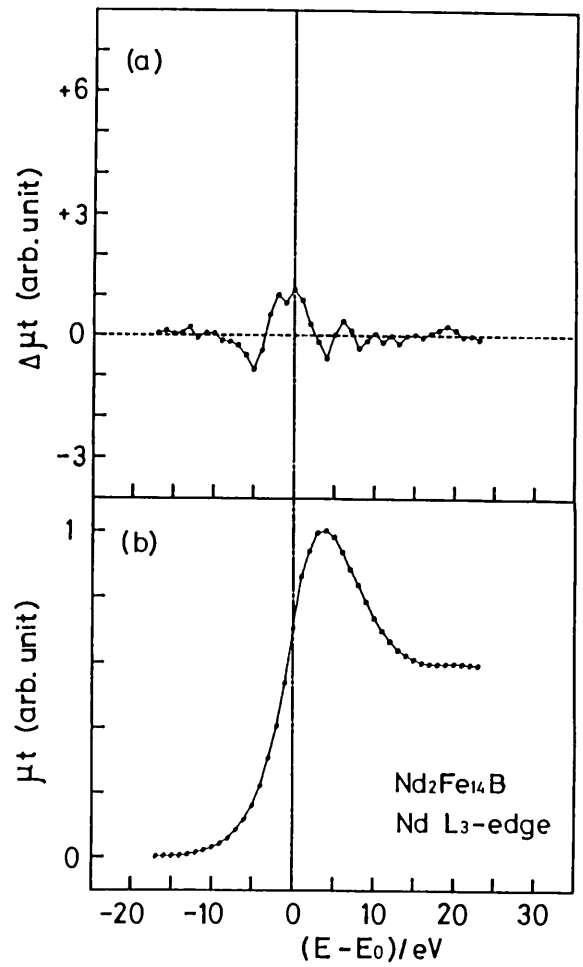

Fig. 35 (a) Magnetic and (b) usual XANES spectra at the L_3 edge of Nd in $Nd_2Fe_{14}B$ taken by the fluorescence method.

Magnetic Circular Dichroism with E-MPW at AR-NE1

Magnetic effects in X-ray absorption processes have been measured by using circularly polarized X-rays emitted from the elliptical multipole wiggler which was installed at the 6.5 GeV Accumulation Ring (AR)[1].

At this beamline, AR-NE1A2, we can obtain the intense circularly polarized X-rays; the brilliance is expected to be 10^{14} photons/sec/mm^2/mrad^2/0.1 %b.w. and the degree of circular polarization, P_C, after monochromatization is estimated to be more than 0.7 in the electron orbital plane for 10 keV X-rays. Monochromatized X-rays from 6 to 30 keV are provided by a fixed-exit-beam double-crystal monochromator using Si(111) and higher harmonics are rejected by detuning the first crystal with respect to the second.

Firstly, the magnetic X-ray-Absorption-Near-Edge-Structure (XANES) spectra of the K edges of Fe and Ni were measured using the transmission and fluorescence methods. These results are in good agreement with earlier data in the literature[2,3], which show that the empty 4p-bands of Fe and Ni have positive and negative spin polarization near the Fermi level, respectively.

Figures 34 and 35 show the magnetic and usual XANES spectra at the $L_{2,3}$ edges of Nd in $Nd_2Fe_{14}B$ taken by the fluorescence method. The origins of the energy scale are chosen at the inflection points of the usual absorption spectra. As shown in Fig. 34, a large positive magnetic effect is observed near the L_2 edge of Nd, which reveals that the unoccupied 5d-bands are polarized due to the strong interaction between the 4f and 5d electrons of Nd. On the other hand, the magnetic XANES at the L_3 edge of Nd (Fig. 35) is quite different from that at the L_2 edge. The intensity of the magnetic XANES at the L_3 edge is about one sixth of that at the L_2 edge, though the intensity ratio of the magnetic XANES at the L_2 and L_3 edges is expected to be about -2 according to a phenomenological calculation on the basis of free atoms[4]. The magnetic effect below the Fermi level,

observed near the L_3 edge, may be ascribed to the contribution of the majority band of 4f states to the magnetic XANES due to the quadrupole transition[5].

Using the fluorescence method, we already took the magnetic XANES spectra at the $L_{2,3}$ edges of Pt in several kinds of Fe-Pt compounds and at the K edge of Fe in Ho-IG foil. Analysis of these results is now in progress.

T. Iwazumi

1) S. Yamamoto, H. Kawata, H. Kitamura, M. Ando, N. Sakai and N. Shiotani: Phys. Rev. Lett. 62 (1989) 2672.
2) G. Schütz, W. Wagner, W. Wilhelm, P. Kienle, R. Zeller, R. Frahm and G. Materlik: Phys. Rev. Lett. 58 (1987) 737.
3) S. P. Collins, M. J. Cooper, A. Brahmia, D. Laundy and T. Pitkanen: J. Phys. Condens. Matter, 1 (1989) 323.
4) G. Schütz, M. Knülle, R. Wienke, W. Wilhelm, W. Wagner, P. Kienle and R. Frahm: Z. Phys. B-Condensed Matter 73 (1988) 67.
5) P. Carra and M. Altarelli: Phys. Rev. Lett. 64 (1990) 1286.

Magnetic Compton Scattering Experiments at AR-NE1

Circularly polarized X-rays interact with the electron spin moments in the process of Compton scattering, so that the intensity becomes spin-dependent. Furthermore the energy spread of Compton scattering gives information about the momentum-space density of electrons. Thus the magnetic Compton scattering experiment provides information about magnetic-electron momentum-space density in ferromagnetic materials. Quantitatively, the Compton profile $J(p_z)$, the magnetic Compton profile $J_{mag}(p_z)$, and the cross section $(d^2\sigma/d\Omega dE)$ can be expressed by following equations;

$$J(p_z) = \iint(n\uparrow(p) + n\downarrow(p))\cdot dp_x\cdot dp_y$$
$$J_{mag}(p_z) = \iint(n\uparrow(p) - n\downarrow(p))\cdot dp_x\cdot dp_y$$
$$d^2\sigma/d\Omega dE = C_0(E_0, E, k_0, k, \theta, P_l)\cdot J(p_z) + C_1(E_0, E, k_0, k, \theta)\cdot P_c\cdot J_{mag}(p_z)$$

where $n\uparrow(p)$ and $n\downarrow(p)$ are the electron momentum densities with spin-up and spin-down, respectively. Then the Compton profile and the magnetic Compton profile are expressed by the projection of the total electron density $(n\uparrow(p) + n\downarrow(p))$ and the magnetic electron density $(n\uparrow(p) - n\downarrow(p))$ along the scattering vector. The cross section is expressed by the linear combination of $J(p_z)$ and $J_{mag}(p_z)$. The coefficients of C_0 and $C_1\cdot P_c$ are given by the experimental conditions; E_0, E and k_0, k are the X-ray energies and wave vectors of the incident and scattered X-rays, respectively. θ is the scattering angle; P_l and P_c are the Stokes' parameters for the linear and circular polarization of the incident X-rays.

Figure 36 shows an experimental arrangement for magnetic Compton scattering. Circularly polarized X-rays from the ellipsoid-multipole wiggler (E-MPW) are monochromatized by the Quasi-Doubly-Bent Si(111) monochromator and focused at the sample position. The magnetization of the sample is switched by an electric magnet. Finally, Compton scattered X-rays are detected with a segmented Ge-SSD detector which has a high counting-rate capability. This detector consists of 13 elements, each of which has an 80 mm^2 active area with an independent amplifier ADC and MCA. The count rate of each element is adjusted to be less than 3×10^4 cps by using a slit in front of the detector in order to keep a good energy resolution. Consequently, the count rate of 4×10^5 cps can be achieved with 13 elements by summing up each data.

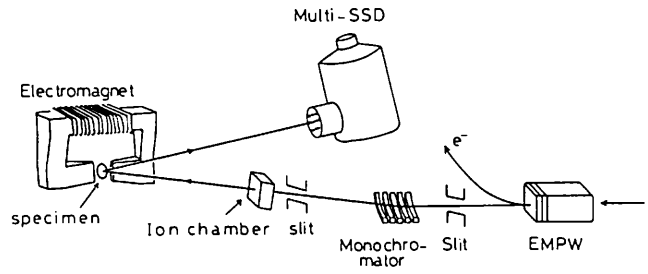

Fig. 36 Experimental setup for magnetic Compton scattering. EMPW : ellipsoid multipole wiggler.

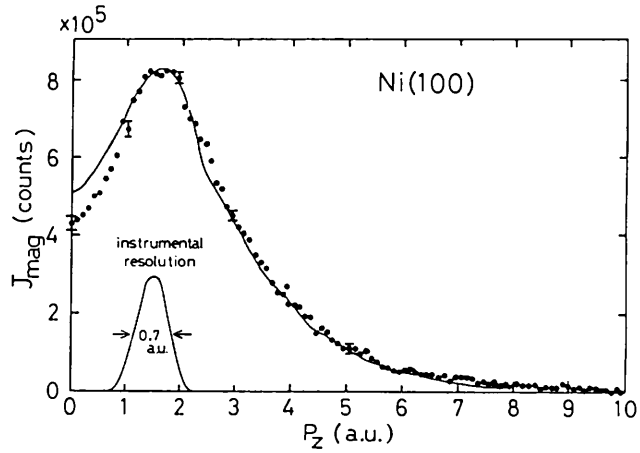

Fig. 37 Magnetic Compton profile of Ni(100).

A detailed description of this improvement is reported in the users' short reports in this volume.

Figure 37 shows the magnetic Compton profile (MCP) of Ni<100> which was obtained by the above experimental arrangement. Good statistical accuracy of this profile demonstrates a clear discrepancy between experiment and theory. Using this experimental arrangement, MCP of Fe (+ 3 % Si, single crystal), Fe-Ni alloy ($Fe_{50}Ni_{50}$, single crystal), and Gd (polycrystal) were also measured. In the case of Gd metal, a high statistical accuracy of the MCP gives information about magnetic electrons from not only 4f electrons but also additional contributions from 5d and 6s electrons. The detailed description is also reported in this volume.

H. Kawata

Observation of Quantum Beats in Nuclear Bragg Scattering of α-$^{57}Fe_2O_3$

Nuclear Bragg scattering (NBS) from a $^{57}Fe_2O_3$ single crystal was observed at the 5 T superconducting vertical wiggler beamline (BL-14B) in July, 1990 with a 40 cps event rate. During the summer shutdown, final adjustments of a newly constructed diffractometer for NBS experiments were made. All rotation axes of this diffractometer are made horizontal because it was designed originally for use of undulator X-rays at the AR-NE3 beamline. Test operation was performed in December, 1990 at BL-16A, a 53-pole wiggler beamline, for two weeks with multi-bunch operation followed by four-day single-bunch operation. An event rate of more than 500 cps was observed in multi-bunch operation. This event rate was larger enough to measure the energy-angle distribution of NBS, to take topographs as well as to measure Mössbauer absorption spectra not by oscillating an absorber but the hematite crystal, keeping its angular position at fixed deviations from the Bragg condition. The Mössbauer absorption spectrum revealed a characteristic dependence on the deviation angle from the Bragg conditions, which was expected from the enhancement effect of the resonant NBS.

In single-bunch operation, with roughly 1/10 event rate of that in multi-bunch operation, quantum beats in the time domain which are the Fourier transforms of the energy spectrum were measured. An avalanche photodiode detector developed for timing experiments in the X-ray region was used for this measurement. This detector has some excellent characteristics; time resolution as high as 300 ps, low noise level, as well as short tails of the output pulses. Although the efficiency for 14.4 keV photons is approximately 3 %

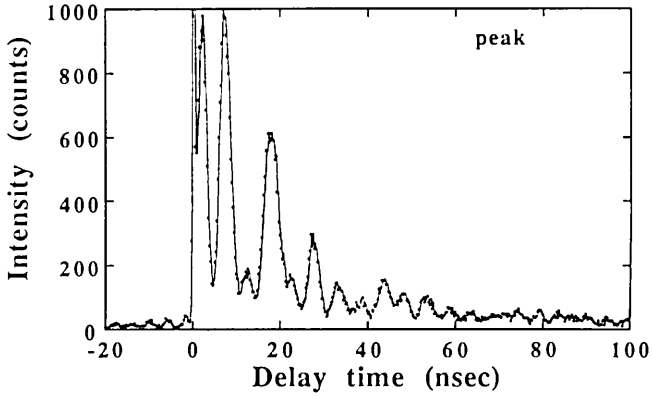

Fig. 38 Quantum beats observed in nuclear Bragg scattering from α-$^{57}Fe_2O_3$ (hematite). The sample crystal was set on the peak of 777 nuclear allowed but electric forbidden Bragg reflection. Accumulation time was approximately 10 hours.

at present, we can get the profiles of the quantum beat as shown in Fig. 38 with the help of the high event rate of the NBS.

Owing to the high time resolution of the detector, the first peak of the quantum beat can be separated from the prompt peak. The low noise level of the detector enabled us to observe the quantum beats just before the prompt peak though the signal level is less than 30. These correspond to transitions which occur more than 0.6 μm after the incident photon pulses. Applications to NBS from other Mössbauer species which have shorter life times are highly envisaged.

T. Ishikawa

XAFS Measurement in a Small Area with an X-ray Microprobe

X-ray fluorescence (XRF) analysis with a high spatial resolution and high sensitivity is an attractive application of synchrotron radiation to the chemical characterization of matter. The X-ray microprobe system at BL-4A consists of a fixed-exit double-crystal monochromator and a Pt-coated ellipsoidal mirror of 1/9.5 demagnification. A pinhole is placed at the focal point of the ellipsoidal mirror and the sample behind the pinhole is scanned 2-dimensionally for the elemental mapping. A Si(Li) detector is used for XRF measurement. The spatial resolution depends on the dimension of the pinhole and was around 10 μm. The incident photon flux at the sample was 3×10^7 photons/s for 8 keV X-rays at a storage beam current of 300 mA. Applications to geological and biological samples are now under way. Figure 39 shows the

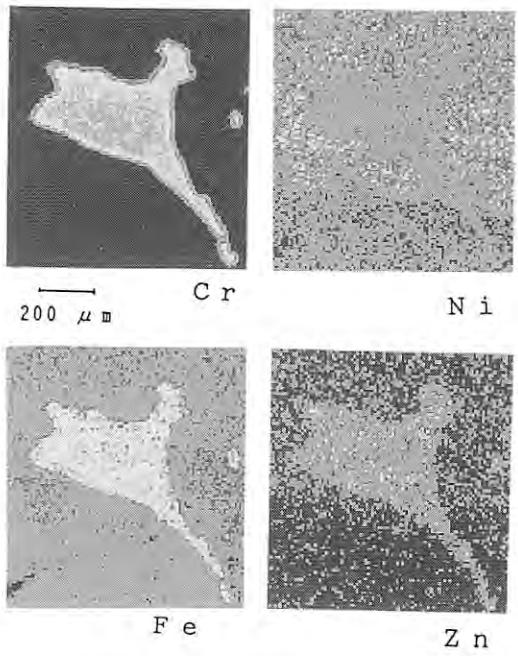

Fig. 39 Elemental imaging of a rock sample (peridotite) using X-ray fluorescence detection.

elemental mapping of peridotite with a spatial resolution of about 20 μm. The elemental distributions reflect the constituent minerals, i.e. chromite, olivine, and pyroxene. In a point-measurement mode, in which a small area or a small sample is analyzed while the sample is at rest during measurement, the minimum detection limit is of the order of fg.

In the present system, incident X-rays are well monochromatized and the focal point is fixed even when the incident energy is changed. The spectroscopic application for chemical-state analysis such as XAFS (X-ray absorption fine structure) in a small region was performed for the first time. Figure 40 shows the fluorescence XANES (X-ray absorption near edge structure) spectra of Fe obtained from minerals shown in Fig. 39. Though the XRF detection of the XAFS has high sensitivity, the spectrum is distorted due to the self-absorption effect for a thick or concentrated sample. The spectra shown in Fig. 40 were obtained with a small exit angle geometry which was quite effective to minimize the spectrum distortion. The difference in the absorption spectrum (Fig. 40) corresponds to the difference in the chemical state of Fe in each mineral. This example demonstrates the new approach to local structure analysis.

A. Iida

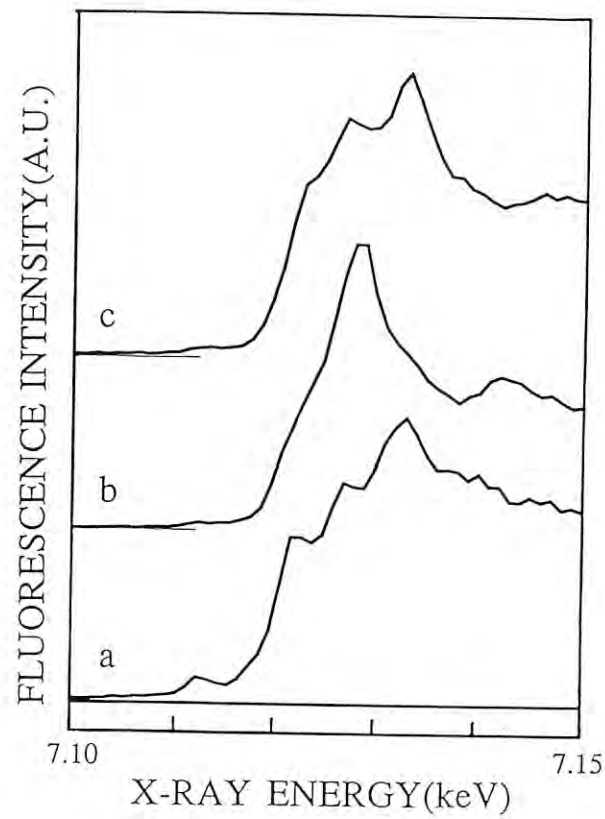

Fig. 40 Fe K edge X-ray absorption spectra from minerals, a: Cr-spinel, b: olivine and c: pyroxene. Spectra were obtained by X-ray fluorescence detection using an X-ray microprobe.

Protein Crystallography at BL-6A

The protein data collection system which consists of the Weissenberg camera for macromolecular crystallography at BL-6A2, Fuji Imaging Plate, its image reader (BA100) and data processing program "WEIS" is successfully used. A full data set around one axis can be recorded on 10-20 IP sheets from one crystal and total exposure time is about 5-15 min. The resolution limit is always extended when compared with other methods as shown in Table 2. Most users can collect 3 ~ 8 data sets in 24 hours. 53 groups currently use this system and more than 90 protein data are collected.

One of the most important investigations with respect to immune recognition and human health is the three dimensional structural study of the influenza virus neuramidase and complexes with antibody Fab fragments as shown on the cover page of users' short reports.

N. Sakabe

Table 2. Neuraminidase X-ray Data

P. Colman & J. N. Varghese, CSIRO, Australia

Source	No. crystal	No. film	Total reflex.	Unique reflex.	R-factor	Resol. limit	Method
Rotating anode	4	27	52,947	13,947	11.17 %	2.9 A	Oscil.
DESY Hamburg	4	70	129,690	29,807	10.14	2.2	Oscil.
Photon Factory	1	16	178,771	50,917	5.76	1.8	Weis.

E. SUMMARY OF EXPERIMENTAL STATIONS AND BEAMLINE OPTICS

Figures 41 and 42 are the latest overview of the SR laboratory area of the TRISTAN-AR and the PF experimental hall schematically showing the arrangement of the experimental stations now in operation or under construction. This section summarizes the experimental stations in operation with the names of the contact persons. Outlines of the beamline optics for each beamline are also summarized in tabular form.

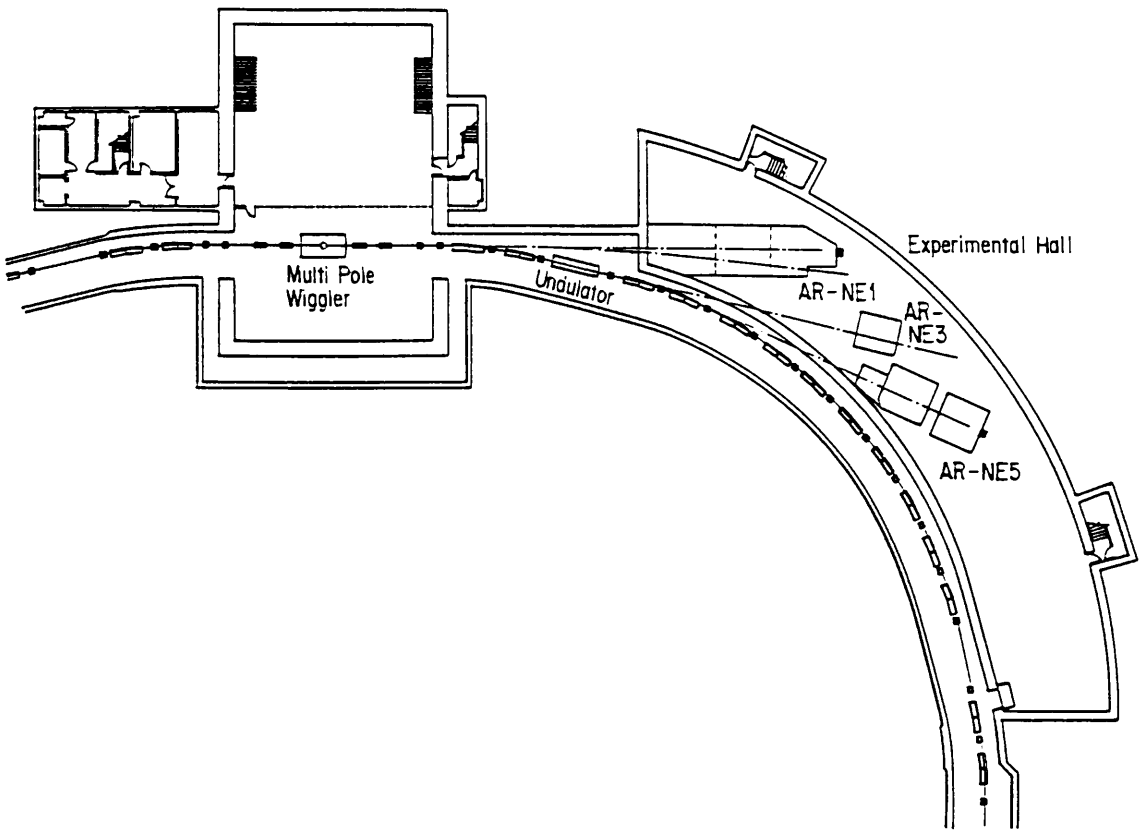

Fig. 41 Plan view of the synchrotron radiation laboratory area of the TRISTAN Accumulation Ring (AR).

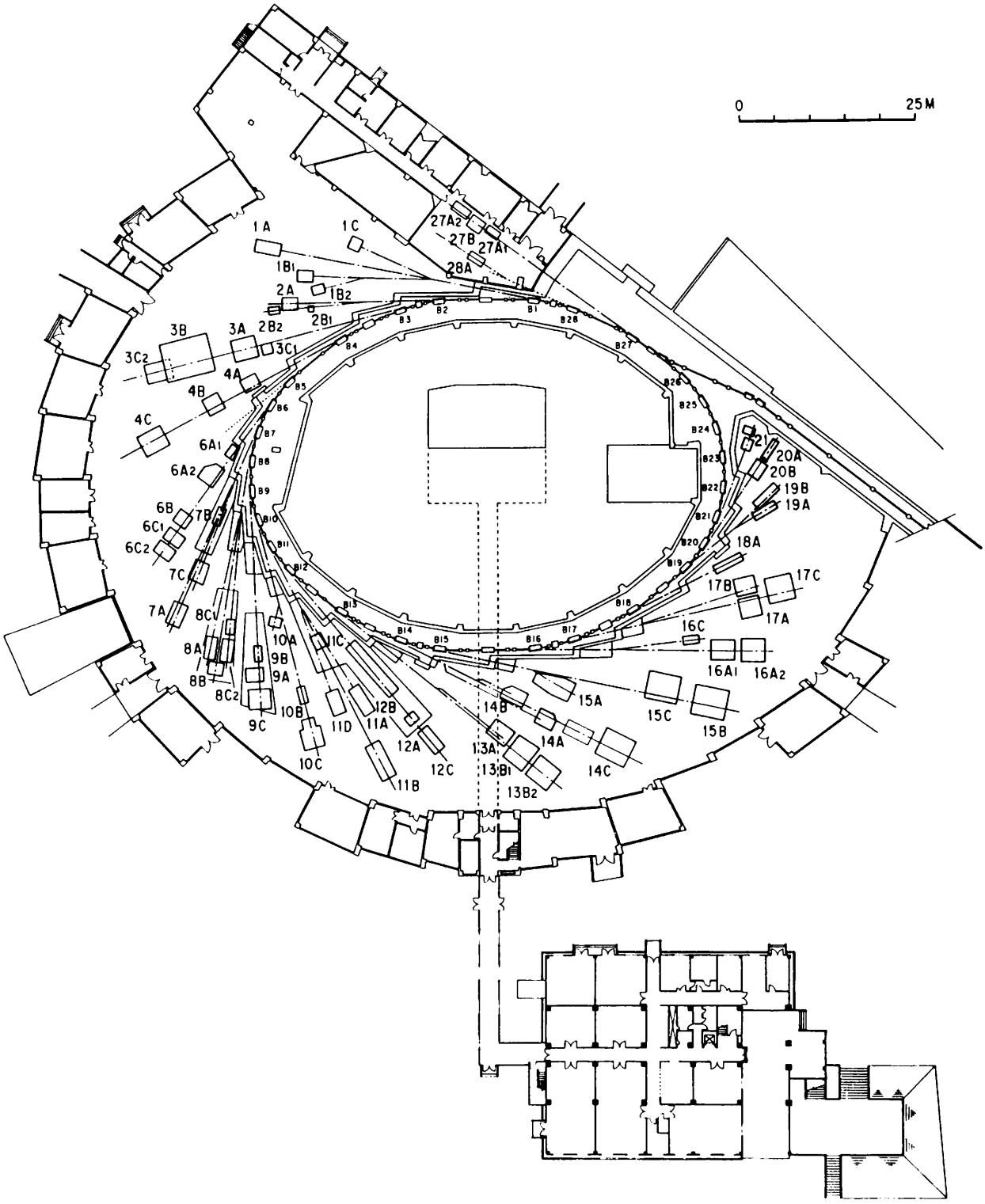

Fig. 42 Plan view of the experimental hall at the PF 2.5 GeV storage ring.

Table 3. List of Experimental Stations

Experimental Station	Contact person
PF (Photon Factory Ring)	
BL-1 [NTT]	
A Solid surface analysis	M. Oshima
B X-ray lithography	H. Kinoshita
C Photochemical reaction	T. Urisu
BL-2 (Undulator)	
A Soft X-ray spectroscopy	Y. Kitajima
B1 Soft X-ray microscopy	A. Yagishita
B2 Soft X-ray spectroscopy	"
BL-3	
A X-ray diffraction and scattering	S. Sasaki
B VUV and soft X-ray spectroscopy	A. Yagishita
C1 X-ray diffraction	S. Sasaki
C2 X-ray topography in milli-Kelvin region (for solid helium)	T. Nakajima
BL-4	
A Trace element analysis,	A. Iida
B Liquid/melt structure analysis, Powder diffraction, Micro-crystal structure analysis	K. Ohsumi
C X-ray diffuse scattering, Fluorescent EXAFS	S. Kishimoto
BL-6	
A1 Ultra small-angle X-ray scattering	M. Ando
A2 Macromolecular crystallography by Weissenberg camera	N. Sakabe
B X-ray spectroscopy and diffraction	M. Nomura
C1 X-ray diffraction at low temperatures	T. Nakajima
C2 Accurate lattice spacing measurement	M. Ando
BL-7 [The Research Center for Spectrochemistry, The Univ. of Tokyo]	
A Soft X-ray photoemission spectroscopy	H. Namba
B Surface photochemical reaction	"
[PF]	
C X-ray spectroscopy and diffraction	M. Nomura
BL-8 [Hitachi]	
A Soft X-ray spectroscopy	Y. Hirai
B EXAFS	A. Nakano
C1 X-ray lithography	K. Mochiji
C2 X-ray tomography and digital radiography	K. Usami
BL-9 [NEC]	
A X-ray lithography	K. Suzuki
B Photochemical reaction	I. Nishiyama
C EXAFS and X-ray topography/diffraction	J. Mizuki
BL-10	
A X-ray diffraction/scattering, Crystal structure analysis	S. Sasaki
B XAFS	M. Nomura
C Small-angle X-ray scattering of enzymes, Surface diffraction	K. Kobayashi
BL-11	
A Soft X-ray spectroscopy	A. Yagishita
B Surface EXAFS, Soft X-ray spectroscopy	Y. Kitajima
C VUV spectroscopy (solid state)	H. Kato
D Angle-resolved photoelectron spectroscopy	"

Experimental Station	Contact person
BL-12	
A VUV spectroscopy (gas phase)	K. Tanaka
B VUV high resolution spectroscopy	K. Ito
C Photochemical reaction	K. Tanaka
BL-13 (Multipole wiggler/Undulator)[Reserch team for advanced materials*]	
A Accurate lattice parameter measurement	K. Nakayama
B1 Surface-sensitive XAFS, X-ray diffraction	H. Oyanagi
B2 High pressure & high temperature X-ray diffraction	O. Shimomura
BL-14 (Vertical wiggler)	
A Crystal structure analysis of proteins, EXAFS	S. Kishimoto
B High precision X-ray optics	X. Zhang
C General purpose (X-rays)	N. Watanabe
BL-15	
A Small-angle X-ray scattering of muscle and alloys	Y. Amemiya
B X-ray topography and interferometry	H. Kawata
C High-resolution X-ray diffraction	X. Zhang
BL-16 (Multipole wiggler/Undulator)	
A General purpose (X-rays)	T. Matsushita
U Soft X-ray spectroscopy	H. Kato
BL-17 [Fujitsu]	
A Characterization of crystals	S. Komiya
B Photochemical vapor deposition	Y. Nara
C X-ray lithography	S. Okamura
BL-18 [The Institute for Solid State Physics, The Univ. of Tokyo]	
A Angle-resolved photoelectron spectroscopy of surfaces and interfaces	A. Kakizaki
BL-19 (Revolver undulator) [The Institute for Solid State Physics, The Univ. of Tokyo]	
A Spin polarized photoelectron spectroscopy	A. Kakizaki
B Photoelectron spectroscopy at various temperatures	"
BL-21 [Light Source Division]	
Beam position monitoring	T. Katsura
BL-28 (Undulator)	
VUV and soft X-ray spectroscopy with circularly polarized undulator radiation	T. Miyahara
AR (Tristan Accumulation Ring)	
AR-NE1 (Multipole wiggler/Undulator)	
A1 Precision Compton and magnetic Compton scattering	H. Kawata
A2 Spectroscopy and scattering with circularly polarized X-rays	T. Iwazumi
B Spectroscopy with circularly polarized soft X-rays	Y. Kitajima
AR-NE3 (Undulator)	
Surface diffraction, Nuclear Bragg scattering	X. Zhang
AR-NE5	
A Angiography, X-ray tomography	K. Hyodo
C High pressure & high temperature X-ray diffraction	T. Kikegawa

* National Laboratory of Metrology, National Institute of Researches in Inorganic Materials, Electrotechnical Laboratory, National Chemical Laboratory, The Institute of Physics and Chemical Research

Table 4. X-Ray Beamline Optics

Branch Beam Line	H. Angular Acceptance (mrad)	Typical Beam Size (Hmm × Vmm)	Photon Flux at Sample Position	Monochromator Crystal	Energy Resolution $(\Delta E/E)\times10^{-4}$	Energy Range (keV)	Mirror
BL-3A	4	100 × 5 4 × 0.1		Double Crystal Si(111) Sagittal Focusing	~ 2	4 ~ 25	Collimating and Focusing Mirrors (Fused Quartz)
BL-3C1/C2	2	20 × 4		None		4 ~ 30	None
BL-4A	6	50 × 4 4 × 1		Double Crystal Sagittal Focusing	~ 2	4 ~ 20	None
BL-4B	4.5	50 × 5		Double Crystal Si(111)	~ 2	4 ~ 35	None
BL-4C	4	4 × 1		Double Crystal Si(111) Sagittal Focusing	~ 2	4 ~ 20	None
BL-6A1	0.1	10 × 3		Plane(111)	7.5	8 ~ 17	
BL-6A2	4	2.5 × 1		Bent Si(111) (a = 0, 6.0°, 7.8°, 9.5°, 11.4°, 13.7°, 16.5°)		5 ~ 25	Bent Plane Fused Quartz
BL-6B	4	8 × 1		Double Crystal Si(220), Si(111), Si(311) Sagittal Focusing with Si(111)	~ 2	4 ~ 25 (4 ~ 13)	None
BL-6C1	0.5	10 × 5		None		8 ~ 30	
BL-6C2	0.5	5 × 5		Channel-Cut Si (111)	7.5	8 ~ 12	None
BL-7C	4	8 × 1	1×10^{10}/6mm^2 (8 keV, 300 mA) (1×10^{11} when focused)	Double Crystal Si (111) Sagittal Focusing	~ 2	4 ~ 20 (4 ~ 13)	Double Mirror Fused Quartz Focusing
BL-8C1/C2	5	50 × 5	2×10^6/mA·mm^2 at 10 keV with Si (111)	Channel-Cut Si(220), Si(111), Si(400)	~ 2	5 ~ 40	None
BL-9A	5	25 × 25				1.2 ~ 3.1	SiC
BL-9C	5	150 × 5		Double Crystal Si(111) Sagittal Focusing	~ 2	5 ~ 25	None
BL-10A	1	10 × 3		Si(111), Si(220) Ge(111), InSb(111) Quartz(100), PG(002) Curved Si(111) (α ~ 4°, 8°)	50 ~ 5	5 ~ 25	None
BL-10B	2	8 × 1	1×10^9/7mm^2 (10 keV, 300 mA)	Channel-Cut Si(311)	1	6 ~ 30	None

Branch Beam Line	H. Angular Acceptance (mrad)	Typical Beam Size (Hmm × Vmm)	Photon Flux at Sample Position	Monochromator Crystal	Energy Resolution $(\Delta E/E)\times10^{-4}$	Energy Range (keV)	Mirror
BL-10C	4	6 × 1.5	~ 10^{10}/9mm^2 (8 keV, 100 mA)	Double Crystal Si(111)	2	4 ~ 10	Bent Cylinder
BL-13A	1			Double Crystal Si(220)	~ 0.1	4 ~ 30	None
BL-13B1/B2	4			Double Crystal Si(111), Si(220)	~ 2	4 ~ 25	Bent plane Fused Quartz
BL-14A	1.28 (Vertical)	5 × 38		Double Crystal Si (111) Si (422) Si (553)	2	5.1 ~ 19.1 14.4 ~ 51.7 22.7 ~ 84.5	Bent Cylinder for Vertical Forcusing, Pt-coated Fused Quartz
BL-14B	2.2	5 × 30		Double Crystal Si(111),Si(220),Si(311)	2	5.2 ~ 57	None
BL-14C	1.3	10 × 40		Double Crystal Si(111), Si(220)	2	5.5 ~ 69	None
BL-15A	2	2.6 × 1.3	9 × 10^{10}/6mm^2 (8.0 keV, 150 mA)	Curved Crystal Ge(111) (α = 8.0°)	~ 10	5.6 ~ 12.4	Cylinder, Fused Quartz
BL-15B	0.14	5 × 5		None		3.5 ~ 34	None
BL-15C	2	60 × 6		Double Crystal Si(111)		4 ~ 30	None
BL-16A	4	4 × 1		Double Crystal Si(111) Sagittal Focusing	~ 2	4 ~ 35	Commissioning
BL-17A	4	100 × 10		Double Crystal Si(111)	~ 2	4 ~ 5	None
BL-17C	1	20 × 5		None		1	Quartz (plane)
AR-NE1-A1	2	8 × 3	1 × 10^{10}/mA/mm^2 (60 keV)	Single Crystal Si(111) (Double bent crystal Si(111)	~ 15	40 ~ 70	None
AR-NE1-A2	2	80 × 4 4 × 4		Double Crystal Si(111) Sagittal Focusing	~ 2	6 ~ 28	Bent plane
AR-NE3	—	10 × 2	~1 × 10^{11} (14.4 keV, 6.5 GeV, 25 mA)	Double Crystal Si(111)	~ 2	5 ~ 25	None
AR-NE5-A	10	120 × 70		Single Crystal Si(311) (α = 4° ~ 5.9°)	~ 50	20 ~ 40	None
AR-NE5-C	10	70 × 5		Double Crystal Si(111) Sagittal Focusing	~ 10	30 ~ 100	None

Table 5. VUV and Soft X-ray Monochromators

Branch Beamline	Acceptance Horiz./Vert. (mrad)	Type of Monochromator	Grating Grove density (l/mm)	Photon Energy (eV)	Beam Size (mm)	Typical Resolution ($\lambda/\Delta\lambda$)	Reference
BL-7B (RCS)	6 4	1m Seya-Namioka	1200 2400	5 ~ 45	1 × 1	1000	1
BL-11C	4.8 3	1m Seya-Namioka	1200 2400	4 ~ 30	~1 ϕ	1000	2
BL-12A	2.4 1.5	1m Seya-Namioka	1200 2400	4 ~ 35	~1 ϕ	1000	3
BL-12B	5 3.6	6.65 m Off-Plane Eagle	1200 4800	5 ~ 30	----	2.5×10^5	4, 5
BL-1A (NTT)	4 0.5	Grating/Crystal	1200 2400	50 ~ 900	4 × 1	500	6
BL-1B' (NTT)	1.2 4	Plane Grating	600 1200 2400	10 ~ 1000	5 × 1	200	----
BL-2B2 Undulator	K = 0.55 ~ 2.2 λ_u = 6 cm	10 m Grazing Incidence α = 89°	1200 2400	250 ~ 1600	< 0.2 ϕ	500 ~ 5000	7, 8
BL-3B	10 2	Grazing Incidence R = 24 m $\alpha+\beta$ = 165°	200 600 1800	10 ~ 280	< 2 ϕ	200 ~ 3000	9
BL-7A (RCS)	6 1	Plane Grating	1200 2400	10 ~ 1000	2 × 1	500	10
BL-8A (Hitachi)	0.5 1	Varied-space Plane Grating	800 2400	40 ~ 1800	5 × 1	1000	11
BL-11A	1 0.5	2 m Grazing Incidence α = 88° Grasshopper Mark VII	600 1200 2400	40 ~ 1000	< 1 ϕ	200 ~ 2000	12
BL-11D	1.5 2	Grazing Incidence R = 2 m $\alpha+\beta$ = 154°	600 1200 2400	20 ~ 150	1.5 ϕ	100 ~ 1500	13
BL-12C'	3.8 1	Plane Grating	1200	50 ~ 690	7 × 15	100	----
BL-16U Undulator	K = 0.5 ~ 5.75 λ_u = 12 cm	2 m Grazing Incidence α = 87°	1200 2400	40 ~ 600	2 × 1	1400 ~ 2500	14
BL-18A (ISSP)	2 2	Grazing Incidence R = 3 m $\alpha+\beta$ = 160° R = 6.65 m $\alpha+\beta$ = 167.5°	300 600 1200 500	12 ~ 250	< 1 ϕ	1000 ~ 2000	15

Branch Beamline	Acceptance Horiz./Vert. (mrad)	Type of Monochromator	Grating Grove density (l/mm)	Photon Energy (eV)	Beam Size (mm)	Typical Resolution ($\lambda/\Delta\lambda$)	Reference
BL-19A Revolver Undulator (ISSP)	K = 1.0 ~ 9.0 λ_u = 16.4 cm	Grazing Incidence R = 2 m $\alpha+\beta = 160°$ R= 4 m $\alpha+\beta = 170°$	600 1200 600 1200	12 ~ 250	< 0.3 ϕ	1000	16
BL-19B Revolver Undulator (ISSP)	K = 0.5 ~ 1.25 λ_u = 5 cm K = 0.5 ~ 2.5 λ_u = 7.2 cm K = 1.0 ~ 5.0 λ_u = 10 cm	Varied-space Plane Grating	800 2400	10 ~ 1200	< 0.5 ϕ	1500	16
BL-28U Undulator	$K_x \simeq$ 0.5 ~ 3 $K_y \simeq$ 0.5 ~ 0.75 λ_u = 16 cm	Grazig Incedence R = 2 m $\alpha+\beta = 160°$ R = 4 m $\alpha+\beta = 170°$	600 1200 600 1200	15 ~ 280	< 0.5 ϕ	1000	----
AR-NE1B Undulator	$K_x \simeq$ 0.5 ~ 3 $K_y \simeq$ 0.5 ~ 7.5 λ_u = 16 cm	10 m Grazing Incidence $\beta = 89°$	1200 2400	250 ~ 1800	----	2000	----
BL-1A (NTT)	4 0.5	Grating/Crystal InSb (111) Si (111)	----	2500 ~ 4000	4 × 1	2000	6
BL-2A Undulator	K = 0.5 ~ 2.2 λ_u = 6 cm	Double Crystal InSb (111) Si (111)	----	1760 ~ 6000	< 0.5 ϕ	5000	8
BL-8B (Hitachi)	6 0.5	Double Crystal InSb (111) Si (111)	----	1700 ~ 14000	1.9 × 0.5	5000	----
BL-11B	4 0.6	Double Crystal InSb (111)	----	1760 ~ 3650	8 × 1	2000	17, 18
BL-1B (NTT)	1.2 4	Plane Mirror	----	----	5 × 1	----	----
BL-1C (NTT)	2 4	Toroidal Mirror	----	----	3 × 5	----	19
BL-2B1	K = 0.5 ~ 2.2 λ_u = 6 cm	Zone Plate	----	400 ~ 830	~ 0.01ϕ	50	20, 21
BL-9A (NEC)	5 0.3	Oscillating Mirror	----	----	----	----	22
BL-9B (NEC)	10	Plane + Toroidal Mirrors	----	----	15 × 20	----	22
BL-12C	3.8 1	Toroidal + Multilayer Mirrors	Rh - Si 21 Layers Rh - C 21 Layers	80 ~ 103 89 ~ 124	2 × 1	12 15	23
BL-17B (Fujitsu)	8 1	Toroidal Mirror	----	----	< 1 ϕ	----	----

References

1. H. Namba et al., Rev. Sci. Instrum. **60**, 1917 (1989).
2. Photon Factory Activity Report 1982/1983, V-15 (1984).
3. Photon Factory Activity Report 1982/1983, V-17 (1984).
4. K. Ito et. al., Appl. Opt. **25**, 837 (1986).
5. K. Ito et al., Appl. Opt. **28**, 1813 (1989).
6. T. Kawamura et al., Rev. Sci. Instrum. **60**, 1928 (1989).
7. H. Maezawa et al., Nucl. Instrum. and Meth. A**246**, 310 (1986).
8. H. Maezawa et al., Rev. Sci. Instrum. **60**, 1889 (1989).
9. A. Yagishita et al., KEK Preprint 90-132 (1990).
10. H. Namba et al., Rev. Sci. Instrum. **60**, 1909 (1989).
11. M. Itou et al., Appl. Opt. **28**, 146 (1989).
12. M. Yanagihara et al., KEK Report 84-17 (1984).
13. T. Miyahara et al,. Jpn. J. Appl. Phys. **24**, 293 (1985).
14. Y. Muramatsu and H. Maezawa, Rev. Sci. Instrum. **60**, 2078 (1989).
15. S. Suzuki et al., Activity Report of SRL-ISSP 60 (1989).
16. A. Kakizaki et al., Rev. Sci. Instrum. **60**, 1893 (1989).
17. T. Ohta et al., Nucl. Instrum. and Meth. A**246**, 373 (1986).
18. M. Funabashi et al., Rev. Sci. Instrum. **60**, 1983 (1989).
19. T. Urisu et al., Rev. Sci. Instrum. **60**, 2157 (1989).
20. Y. Kagoshima et al., Jpn. J. Appl. Phys. **29**, L 172 (1989).
21. Y. Kagoshima et al., Rev. Sci. Instrum. **60**, 2448 (1989).
22. Photon Factory Activity Report 1988 # 6, I-13 (1989).
23. Photon Factory Activity Report 1988 # 6, I-11 (1989).

ISSN 0912-1803

PHOTON FACTORY
ACTIVITY REPORT
1990
#8

PHOTON FACTORY ACTIVITY REPORT 1990

#8